Fractal Dimension Study of Southern California Temporospatial Seismicity Patterns from 1982 to 2020

Hong Ji Cai

A thesis

submitted to the Faculty of

the department of Earth and Environmental Sciences

in partial fulfillment

of the requirements for the degree of

Master of Science

Boston College
Morrissey College of Arts and Sciences
Graduate School

August 2022

Fractal Dimension Study of Southern California Temporospatial Seismicity Patterns from 1982 to 2020

Hong Ji Cai

Advisor: John E. Ebel, Ph.D.

Power-law scaling relationships concerning the earthquake frequency-magnitude distribution and the fractal geometry of spatial seismicity patterns may provide applications to earthquake forecasting and earthquake hazard studies. Past studies on the fractal characteristics of seismic phenomena have observed spatial and temporal differences in earthquake clustering and b value in relation to fractal dimension value. In this thesis, an investigation of the spatiotemporal seismicity patterns in southern California for the years 1982 to 2020 was conducted. The range and temporospatial distribution of b and D_2 values for earthquake hypocenters contained in the Southern California Earthquake Data Center catalogue were calculated and shown in time series and spatial distribution maps. b values were calculated using both the Least Squares Method and the Maximum Likelihood Method while D_2 values were calculated for length scales between 1 km to 10 km. A set of b and D_2 values were calculated after declustering for foreshocks and aftershocks using Gardner and Knopoff's declustering algorithm. b values decreased while D_2 values increased on the dates of $M > 6.0$ earthquakes, whereas b values increased and D_2 values decreased on the dates after $M > 6.0$ earthquakes. Declustering results suggest an influence of earthquake aftershocks to increase D_2 values while decreasing b values. The role for b values and D_2 values to delineate both the temporal and spatial extent of aftershock sequences for large earthquakes may prove to have an application in earthquake hazard studies.

Table of Contents

List of Tables

List of Tables

List of Figures

Acknowledgements

Introduction

The understanding and application of fractals, subsets describing self-similar shapes, have been explored and expanded upon to address observations of fractal patterns in a wide variety of physical systems, including seismogenic zones. In seismology, numerous fractal-related seismic studies have been conducted for various geologic settings using D_2 (correlation dimension) values calculated with respect to a set of earthquake source parameters obtained from regional earthquake catalogues (Öncel et al., 1996; Godano and Caruso, 1995; Tosi, 1998; Telesca et al., 2001; Oncel and Wilson, 2002; Öncel and Wilson, 2004; Wyss et al., 2004; Mandal and Rastogi, 2005; Chen et al., 2006; Roy and Nath, 2007; Tosi et al., 2008; Molchan and Kronrod, 2009; Roy et al., 2010; Öztürk et al., 2012; Han et al., 2015; Mondal et al., 2019; Radziminovich et al., 2019; Mandal et al., 2021; Tiwari et al., 2021). Earthquake source parameters include time of rupture, hypocenter, seismic moment, magnitude, and focal mechanism (fault type and orientation) (Roch et al., 2016; Nordström et al., 2017). Past studies have applied different notions of fractal dimension to different aspects of the seismic process, such as fault traces (Okubo and Aki, 1987; Aviles et al., 1987; Bonnet et al., 2001), rock fracturing (Hirata et al., 1987; Feng and Seto, 1999), and earthquake locations (Öncel et al., 1996; Tosi, 1998; Telesca et al., 2001; Oncel and Wilson, 2002; Wyss et al., 2004; Mandal and Rastogi, 2005; Chen et al., 2006; Roy and Nath, 2007; Tosi et al., 2008; Molchan and Kronrod, 2009; Roy et al., 2011; Öztürk, 2012; Han et al., 2015; Mondal et al., 2019; Radziminovich et al., 2019; Mandal et al., 2021; Tiwari et al., 2021).

Multiple trends in D_2 values have been reported and related to changes in seismicity. Wyss et al. (2004) showed a difference in D_2 values for locations along the 30 km to 50 km Parkfield section of the San Andreas Fault Zone, in which D_2 values varied between 0.96 to 1.14 for the locked section and 1.45 to 1.72 for the creeping section. Earlier studies assumed their data sets to be monofractal, that is, having a uniform distribution of D_2 values for their study regions. However, the results from

Wyss et al. (2004) suggested that earthquake locations were multifractal as opposed to monofractal. A multifractal set is a set that is the mathematical union of two or more fractal sets. Indeed, Radziminovich et al. (2019) and Chen et al. (2006) spatially mapped D_2 values for the Baikal Rift System from 2003 to 2014 and for the six month time window following the M_w (moment magnitude) 7.6 Chi-Chi earthquake of 1999, respectively. Their results demonstrated a spatially non-uniform distribution of D_2 values for each of their study regions, supporting a multifractal model for earthquake locations.

Hirata et al. (1987) conducted a microfracture experiment on a sample of Oshima granite and computed the D_2 values corresponding to the spatial distribution of the hypocenters of acoustic emissions, seismic waves generated by microfracturing, for three non-overlapping intervals in time prior to rock failure. The sequence of D_2 values 2.75, 2.66, and 2.25 in the study of Hirata et al. (1987) demonstrated a decrease in D_2 values prior to rock failure. In addition, several studies have reported a decrease in D_2 values prior to large earthquakes; these examples include the 1999 M_w 7.6 Izmit earthquake (Roy and Nath, 2007), the 2002 M_w 7.9 Denali Fault earthquake (Roy and Nath, 2007), the 2002 M_w 7.4 Sumatra earthquake (Roy and Nath, 2007), the 2003 M_w 7.2 Fiordland earthquake (Mondal et al., 2019), the 2004 M_w 9.1 Sumatra earthquake (Roy and Nath, 2007), and the 2009 M_w 7.8 Fiordland earthquake (Mondal et al., 2019). Hence, a temporal decrease in D_2 value may serve as an earthquake precursor.

An earthquake precursor refers to any physical phenomena that were reported prior to an earthquake (Cicerone et al., 2009). Examples of earthquake precursors include induced electric and magnetic field changes, groundwater level changes, anomalous gas emissions, temperature changes, unusual surface deformations, and anomalous seismicity patterns (Cicerone et al., 2009). In addition, the b value of

the Gutenberg-Richter law, that is, the absolute value of the slope of the cumulative frequency-magnitude distribution of earthquake magnitudes is an earthquake precursor of utmost interest due to previous attempts in relating the b value to various notions of fractal dimension (Aki, 1981; Hirata, 1989; Öncel et al., 1996; Turcotte, 1997; Legrand, 2002; Oncel and Wilson, 2002; Öncel and Wilson, 2004; Wyss et al., 2004; Mandal and Rastogi, 2005; Chen et al., 2006, Roy et al., 2011; Öztürk, 2012; Han et al., 2015; Mandal et al., 2021).

The purpose of this thesis was to identify, if any, patterns in the temporospatial evolution of b and D_2 values in southern California from 1982 to 2020 and attempt to correlate any such changes to changes in seismicity. In particular, precursory patterns in b and D_2 values prior to large earthquakes were desired. In this thesis, I observed no precursory patterns in b and D_2 values prior to large earthquakes. Instead, I observed

(1) a decrease in D_2 values following declustering of aftershocks,

(2) a decrease in b values and an increase in D_2 values on the months and years of $M > 6.0$ earthquakes,

(3) an increase in b values and a decrease in D_2 values on the months and years after $M > 6.0$ earthquakes

(4) relatively low b values and high D_2 values about the epicenters of $M > 6.0$ earthquakes,

which suggest a relationship between b values, D_2 values, and aftershocks of $M > 6.0$ earthquakes.

Background

Mathematics

From Falconer (2014), a fractal is a set F that fulfills at least one of the following properties:

(1) F has detail on arbitrarily fine length scales.

(2) F is too irregular to be described in traditional geometrical language.

(3) F exhibits self-similarity.

(4) One can calculate two values for F: a "topological dimension" and a "fractal dimension," where the fractal dimension is greater than the topological dimension.

Qualitative observations, such as the rough appearances of fault traces over many length scales (Aviles et al., 1987; Okubo and Aki, 1987) and the self-similar geometry of fault traces (King, 1983; Robertson et al., 1995; Saleur et al., 1996; Bonnet et al., 2001), suggest that faults and other fracture systems are fractal. Since earthquakes occur on faults, the spatial distribution of earthquakes should be fractal, too. Indeed, it has been shown by empirical evidence that both the epicenters and hypocenters of earthquakes fit fractal models under a range of length scales (Öncel et al., 1996; Tosi, 1998; Telesca et al., 2001; Wyss et al., 2004; Mandal and Rastogi, 2005; Roy and Nath, 2007; Tosi et al., 2008; Molchan and Kronrod, 2009; Han et al., 2015; Mondal et al., 2019; Radziminovich et al., 2019; Tiwari et al., 2021).

There exists a spectrum of different notions of fractal dimension, and, for each definition, one can calculate an approximation of the fractal dimension value for that definition (Grassberger, 1983). Typically, seismic studies use D_0 (capacity dimension) (Aviles et al., 1987; Okubo and Aki, 1987; Bonnet et al., 2001; Oncel and Wilson, 2002) or D_2 (correlation dimension) (Öncel et al., 1996; Tosi, 1998; Bonnet et al., 2001; Telesca et al., 2001; Oncel and Wilson, 2002; Öncel and Wilson, 2004; Wyss et

al., 2004; Mandal and Rastogi, 2005; Chen et al., 2006; Kagan, 2007; Roy and Nath, 2007; Öztürk, 2012; Han et al., 2015; Mondal et al., 2019; Radziminovich et al., 2019; Tiwari et al., 2021), which are of the spectrum of D_q (Renyi dimension of order q). Here, for $q \in \{0\} \cup \mathbb{N}$, D_q is defined as

$$(1) \qquad D_q = \frac{1}{1-q} \lim_{s \to 0} \frac{\log \sum_{i=1}^{N(s)} P_i^q}{\log(1/s)},$$

where $N(s)$ is the number of non-empty squares in $\mathbb{R}^2$ or cubes in $\mathbb{R}^3$ of a partitioning with length scale s of a set X, and P_i is the probability for a point in X to belong in the ith square of that partitioning (Grassberger, 1983). When $q = 0$, Eq. (1) becomes:

$$(2) \qquad D_0 = - \lim_{s \to 0} \frac{\log N(s)}{\log s},$$

where $N(s)$ may be interpreted as the minimum number of balls in $\mathbb{R}^2$ or spheres in $\mathbb{R}^3$ of radius s needed to cover X (Grassberger, 1983). As a remark, there is nothing special about using squares or balls as opposed to cubes or spheres. If a set is truly fractal, then by definition it should exhibit self-similarity at both large and small length scales, and calculations using scaled copies of squares or balls and cubes or spheres will yield the same D_q values. Although, in practice there will be some inherent uncertainty in the D_q values so D_q values may not necessarily be identical when different length scales, areas, or volumes are used.

Let the Heaviside step function $H(x)$ be defined as

$$(3) \qquad H(x) = \begin{cases} 0 & x < 0 \\ 1/2 & x = 0 \\ 1 & x > 0. \end{cases}$$

For a finite set X of points, we define the correlation integral $C(s)$ as

$$(4) \qquad C(s) = \lim_{n \to \infty} \frac{2}{n(n-1)} \sum_{i=1}^{n} \sum_{j=1}^{n} H(s - |x_i - x_j|)$$

where x_i and x_j are points in X and n is the number of points in X (Grassberger and Procaccia, 1983). For such a finite set, note that

$$(5) \qquad P_i = \lim_{n \to \infty} \frac{1}{n} n_i,$$

where n_i is the number of points belonging to the ith square or cube of a partitioning of X (Grassberger and Procaccia, 1983). It can be shown that

$$(6) \qquad C(s) \approx \lim_{n \to \infty} \frac{1}{n^2} \sum_{i=1}^{N(s)} n_i^2 = \sum_{i=1}^{N(s)} P_i^2$$

(Grassberger and Procaccia, 1983). Then,

$$(7) \qquad D_2 = \lim_{s \to 0} \frac{\log C(s)}{\log s}$$

(Grassberger and Procaccia, 1983). Physically, the double summation in Eq. (4) counts the number of unique pairs of points contained in an open ball or sphere of radius s, and D_2 indicates how $C(s)$ changes with respect to an increase in the accuracy of the chosen length scale s.

Additionally, there is a proposed relationship between D_0 and the b value of the Gutenberg-Richter law (Aki, 1981), and studies have shown correlations between the fractal dimension and b value (Hirata, 1989; Öncel et al., 1996; Oncel and Wilson, 2002; Öncel and Wilson, 2004; Wyss et al., 2004; Mandal and Rastogi; 2005; Chen et al., 2006, Roy et al., 2011; Öztürk, 2012; Han et al., 2015; Mandal et al., 2021). The empirical Gutenberg-Richter law states that

$$(8) \qquad \log_{10} N(M) = a - bM,$$

where $N(M)$ is the number of earthquakes with magnitudes $\geq M$, and a and b are constants (Gutenberg and Richter, 1944). The scalar seismic moment M_0 of an earthquake is defined as

$$(9) \qquad\qquad M_0 = \mu A \bar{D},$$

where μ is the shear modulus of the rock in which the rupture is embedded, A is the area of the slip patch, and $\bar{D}$ is the average slip (Aki, 1966). Similar to magnitude, the scalar seismic moment is one of the many measures used to quantify the "size" of an earthquake. Whereas the magnitude of an earthquake is based on the amplitude of specific waves, the scalar seismic moment is based on the physical deformation associated with the earthquake. However, it was empirically shown that

$$(10) \qquad\qquad \log_{10} M_0 \approx cM + d,$$

where c and d are constants (Kanamori and Anderson, 1975). According to Aki (1981),

$$(11) \qquad\qquad D_0 \approx \frac{3}{c} b$$

for faults, where c was empirically shown to be typically 1.5 (Hanks and Kanamori, 1979), although other values have been used or proposed (Legrand, 2002; Wyss et al., 2004; Sianturi et al., 2019). Eq. (11) assumes the three following hypotheses (Turcotte, 1997; Legrand, 2002):

(1) Eq. (8) holds,

(2) Eq. (10) holds, and

(3) $M_0 \approx L^3$ or $M_0 \approx A^{3/2}$, where L is the length of the rupture, and A is the area of the rupture.

Although Eq. (11) describes a theoretical relationship that yields the D_0 value for faults, several studies have observed

$$(12) \qquad\qquad D_2 \approx \frac{3}{c}b,$$

an empirical relationship that yields the D_2 value for epicenters or hypocenters of earthquakes and other seismic waves (Wyss et al., 2004; Chen et al., 2006; Öztürk, 2012).

Geology

The seismicity of southern California is a product of the continuous interaction between the Pacific Plate and the North American Plate, where the Pacific Plate moves to the northwest relative to the North American Plate at a rate of $\sim$50 mm/yr, forming a right-lateral transform boundary called the San Andreas Fault (Freed et al., 2007). In truth, the San Andreas Fault Zone is a more accurate descriptor because the San Andreas Fault branches off into smaller faults that, in turn, branch off into even smaller faults due to a long history of seismic ruptures along the plate boundary (Perrin et al., 2016; Ye and Liu, 2017). One can view this branching off into smaller, subsidiary faults to be similar in image to a fractal tree. The seismicity of southern California is widely distributed among the San Andreas Fault Zone, the east-west trending left-lateral Garlock Fault, and the southeast-northwest trending right-lateral faults of the Eastern California Shear Zone of the Mojave Desert, as well as the San Jacinto and Elsinore Fault Zones (Fig. 1). Additionally, other fault zones, such as the transtensional Imperial Fault Zone, and the proximal Laguna Salada Fault, which produced the 2010 $M_{\mathbf{w}}$ 7.2 El Mayor-Cucapah (Baja California) earthquake, play active roles in the seismicity of southern California; for example, Hauksson et al. (2010) suggested that the 2010 $M_{\mathbf{w}}$ 7.2 El Mayor-Cucapah earthquake had triggered seismicity along the San Jacinto and Elsinore Fault Zones.

More than 29 Ma, there was a mid-ocean ridge between the Pacific Plate to the west and the Farallon Plate to the east (Ye and Liu, 2017). On the east side of the Farallon Plate there was a plate boundary that consisted of a subduction zone where the Farallon Plate subducted beneath the North American Plate (Ye and Liu, 2017). Eventually, the mid-ocean ridge was subducted beneath the North American Plate, resulting in compressive, reverse faulting in western California (Nicholson et al., 1986), and Basin and Range extension in eastern California, Nevada, and Utah, followed due to the decrease in horizontal stress from the absence of the Farallon Plate's subduction. As the mid-ocean ridge subducted beneath the North American Plate, this interaction formed a new strike-slip plate boundary due to a change in relative plate motions; this new strike-slip plate boundary, the San Andreas fault, grew in length to both the north and south (Irwin, 1990).

Objectives

The purpose of this study was to

(1) calculate the range and temporospatial distribution of b and D_2 values for earhquake hypocenters in southern California from 1982 to 2020, and

(2) explore the physical significance of these b and D_2 values with respect to temporospatial seismicity patterns.

The purpose of objective (1) was to identify any interesting changes in b or D_2 values in either time or space, in particular, any consistent changes in b or D_2 values that occur immediately, before, or after large earthquakes. The purpose of objective (2) was to correlate interesting changes in b or D_2 values in either time or space to changes in seismicity. In turn, an understanding of what particular changes in b or D_2 values represent physically will assist in future applications of b or D_2 values in seismic studies.

Methods

DATA

All computations used data from the Southern California Earthquake Data Center (SCEDC) catalogue, the archive of the Southern California Seismic Network (SCSN), which is available at scedc.caltech.edu. The SCEDC catalogue contains earthquakes with depths ≤ 35.54 km and $M \leq 7.3$ for an area bounded between $30.86°$ to $38.54°$N and $114.00°$ to $122.22°$W (Fig. 1). In addition to earthquakes, the SCEDC catalogue also contains information about non-earthquakes: quarry blasts, sonic booms, nuclear blasts, teleseismic events, and unknown events (Hutton et al., 2010).

From 1982 to 2020, the SCEDC catalogue reported earthquake magnitudes as energy magnitude ($M_\mathbf{e}$), moment magnitude ($M_\mathbf{w}$), body-wave magnitude ($M_\mathbf{b}$), surface-wave magnitude ($M_\mathbf{s}$), local magnitude ($M_\mathbf{l}$), coda amplitude magnitude ($M_\mathbf{ca}$), helicorder magnitude ($M_\mathbf{h}$), and coda duration magnitude ($M_\mathbf{d}$) (Hutton et al., 2010). In this thesis, I assumed that each of these different ways of computing magnitudes would give values that were approximately similar for magnitudes below approximately 6.3, the value above which the $M_\mathbf{l}$ scale saturates (Hutton et al., 2010).

According to Hutton et al. (2010), the following operational changes probably affected the quality of the SCEDC catalogue for different time intervals:

(1) In 1986, the network sensitivity decreased, which resulted in a lesser number of small earthquakes being recorded.

(2) $M_\mathbf{ca}$ values for the range 2.0 to 3.5 in the 1980s and 1990s may be overestimates, although no values were discussed.

(3) In the 1990s, more $M_\mathbf{l}$ values and fewer $M_\mathbf{ca}$ and $M_\mathbf{h}$ values were recorded.

(4) Beginning in 2000, $M_\mathbf{w}$ became the preferred magnitude for $M \geq 5.0$.

(5) In 2001, the change from the Caltech/USGS Seismic Processing system to the ANSS Quake Monitoring System changed the number of earthquakes with different types of magnitudes.

Finally, a large number of waveforms from 1977 to 1981 were not recoverable (Hutton et al., 2010), resulting in missing earthquake data from 1977 to 1981, including locations and magnitudes. Therefore, the earliest year to be used in the time range of this thesis was 1982.

Magnitude of Completeness

The magnitude of completeness, $M_{\mathbf{c}}$, the minimum M at which all earthquakes are reliably recorded in an earthquake catalogue, was estimated using the Maximum Curvature Method (Wiemer and Wyss, 2000), which equates $M_{\mathbf{c}} - 0.2$ to the M corresponding to the maximum non-cumulative frequency (Fig. 2). Here, the maximum non-cumulative frequency for a set of earthquake magnitudes is defined as the mode of those magnitude values.

Hutton et al. (2010) estimated $M_{\mathbf{c}}$ values for the SCSN catalogue from 1932 to 2008 and reported that, on average, the catalogue was complete for $M_{\mathbf{c}} \geq 1.8$ since 1981, with exceptions. The $M_{\mathbf{c}}$ may vary in both time and space due to improvements in technology, station density, and station coverage (Hutton et al., 2010). For example, offshore areas and areas in Mexico were characterized by high $M_{\mathbf{c}}$ values due to low station coverage (Hutton et al., 2010). Changes in $M_{\mathbf{c}}$ do not reflect changes in seismicity, but rather changes in the ability of the network to consistently detect earthquakes (Hutton et al., 2010).

In this thesis, I computed b values for monthly and yearly partitions of the SCEDC catalogue. In order to obtain an accurate b value for each partition, all earthquakes with M below the $M_{\mathbf{c}}$ of the partition must be removed from the partition prior to

b value calculation. Although other studies have published $M_{\mathbf{c}}$ values for earthquake catalogues pertaining to southern California (Wiemer and Wyss, 2000; Hutton et al., 2010), I chose to recompute $M_{\mathbf{c}}$ values for each partition as my $M_{\mathbf{c}}$ values may not be identical to the $M_{\mathbf{c}}$ values in literature due to differences in catalogues used as well as partitioning of the catalogues.

The SCEDC catalogue was partitioned into subsets corresponding to each year of the study period and a M_c value was found for each subset; these M_c values will be defined as yearly M_c values. In order to maintain closeness to an independent and identical distribution for M values, all yearly partitions should be filtered for the same $M_{\mathbf{c}}$ value. This $M_{\mathbf{c}}$ value corresponded to the maximum yearly $M_{\mathbf{c}}$ value of 2.5 (Fig. 3). Similarly, the SCEDC catalogue was partitioned into subsets corresponding to each month of each year of the study period and a M_c value was found for each subset; these M_c values will be defined as monthly M_c values. In order to maintain closeness to an independent and identical distribution for M values, all monthly partitions were filtered for $M \geq 2.3$, the maximum monthly $M_{\mathbf{c}}$ value (Fig. 3).

b VALUES

Recall that the b value is the absolute value of the slope of the cumulative frequency-magnitude distribution of earthquake magnitudes. Given any population of earthquake M values, the b value is expected to increase as the percentage of high M values decreases. In addition, empirical evidence has shown that the b value decreases with increasing depth, differential stress, and lithostatic stress (Mori and Abercrombie, 1997; Wiemer and Wyss, 1997; Gerstenberger et al., 2001; Scholz, 2015). Past studies have suggested the b value to be a potential earthquake precursor (Smith, 1981; Smith, 1986; Nanjo et al., 2012); however, Hutton et al. (2010) had suggested that temporal changes in the b value were more likely due to problems in the earthquake catalogue itself, such as completeness or network sensitivity, as opposed to any actual

changes in the seismicity rate.

Multiple methods exist to determine the b value (Gutenberg and Richter, 1944; Aki, 1965; Utsu, 1965; Page, 1968; Bender, 1983; Ogata and Yamashina, 1986; Wang et al., 2014; Han et al., 2015). In no particular order, the three most common methods to determine the b value are

   (1) visual inspection for a line of best fit,

   (2) Maximum Likelihood Method, and

   (3) Least Squares Method.

In this thesis, b values were not determined by visual inspection for a line of best fit because I deemed the method to be too impractical in determining a large number of b values and to be too subjective. Instead, in this thesis, b values were determined using both the Maximum Likelihood Method and the Least Squares Method because both methods solve for the b value and its standard deviation using equations. Because different methods may produce different b values for the same set of M values (Bender, 1983; Wiemer and Wyss, 1997; Enescu et al., 2011; Wang et al., 2014; Han et al., 2015), there is much discussion concerning the accuracy of these different methods, including both the Maximum Likelihood Method and the Least Squares Method (Bender, 1983; Guttorp, 1987; Sandri and Marzocchi, 2007; Amorèse et al., 2010). In this thesis, I am interested in reporting spatial or temporal trends in b values. If the Maximum Likelihood Method and the Least Squares Method produce different trends in b value for the same population of M values, then I would dismiss the trend associated with higher standard deviation values.

Let $b_{\mathbf{ML}}$ denote a b value estimated for a set of earthquake magnitudes $\{M_i\}$ using the Maximum Likelihood Method. Then

$$(13) \qquad b_{\mathbf{ML}} = \frac{(N-1)\log_{10} e}{\sum_{i=1}^{N}(M_i - M_0)},$$

where N is the cardinality of $\{M_i\}$, and M_0 is the minimum magnitude in $\{M_i\}$ (Ogata and Yamashina, 1986). Eq. (13) is the equation for the b value that maximizes the likelihood function given by Aki (1965). The standard deviation in $b_{\mathbf{ML}}$, $\sigma_{b_{\mathbf{ML}}}$, is approximated as

$$(14) \qquad \sigma_{b_{\mathbf{ML}}} \approx 2.30 b_{\mathbf{ML}}^2 \sum_{i=1}^{N} \frac{(M_i - \bar{M})^2}{N(N-1)},$$

where $\bar{M}$ is the arithmetic mean of $\{M_i\}$ (Shi and Bolt, 1982).

Let $b_{\mathbf{LS}}$ denote a b value estimated for a set of earthquake magnitudes $\{M_i\}$ using the Least Squares Method, in which $b_{\mathbf{LS}}$ is equal to the absolute value of the slope of the linear regression of $\{M_i\}$ to Eq. (8). The linear regression was calculated using MATLAB's polyfit function, which performs an unweighted least squares linear regression.

Let the set $\{X_i\}$ with arithmetic mean $\bar{X}$ and the set $\{Y_i\}$ with arithmetic mean $\bar{Y}$ have the same cardinality S, and let

$$(15) \qquad \mathrm{ss}_{XX} = \sum_{i=1}^{n}(X_i - \bar{X})^2,$$

$$(16) \qquad \mathrm{ss}_{YY} = \sum_{i=1}^{n}(Y_i - \bar{Y})^2,$$

$$(17) \qquad \mathrm{ss}_{XY} = \sum_{i=1}^{n}(X_i - \bar{X})(Y_i - \bar{Y}).$$

The standard deviation in slope, σ, of a linear regression in the form $\{Y_i\} = a_1\{X_i\} + a_0$ is

$$(18) \qquad \sigma = \sqrt{\frac{\mathrm{ss}_{YY} - a_1\mathrm{ss}_{XY}}{(S-2)\mathrm{ss}_{XX}}}.$$

Eq. (18) was used to estimate the standard deviation in $b_{\mathbf{LS}}$, $\sigma_{b_{\mathbf{LS}}}$.

Coordinate Conversion

In order to calculate D_2 values, hypocenter locations were transformed from geodetic (ϕ, λ, h) to Cartesian coordinates (x, y, z), where ϕ is the latitude, λ is the longitude, and h is the elevation. Let

$$v = \frac{a}{\sqrt{1 - \xi \sin^2 \phi}}, \tag{19}$$

$$\xi = f(2 - f), \tag{20}$$

where $a = 6378.137$ km and $f = 1/298.257223563$ (Featherstone, 1994; Gerdan and Deakin, 1999), then the transformation is achieved by the following three equations:

$$x = (v + h) \cos \phi \cos \lambda \tag{21}$$

$$y = (v + h) \cos \phi \sin \lambda \tag{22}$$

$$z = [v(1 - \xi) + h] \sin \phi, \tag{23}$$

The transformation maps all hypocenter locations from the World Geodetic System of 1984 (WGS84) reference ellipsoid to an Earth-Centered, Earth-Fixed (ECEF) model. Here, v is the WGS84's transverse radius of curvature, a is the WGS84's semi-major axis length, ξ is the WGS84's first eccentricity squared, and f is the WGS84's flattening (Featherstone, 1994; Gerdan and Deakin, 1999). In the ECEF model, the point $(x, y, z) = (0, 0, 0)$ is the center of the ellipsoid, the z-axis and the axis of rotation of the ellipsoid are collinear, the xz-plane is the origin of longitudes, and the xy-plane is the origin of latitudes (Gerdan and Deakin, 1999).

D_2 values

In order to calculate a D_2 value for a subset of an earthquake catalogue, a set of $C(s)$ values corresponding to the set $\{s \in \mathbb{R} \mid 0.1 \text{ km} \le s \le 1000 \text{ km}\}$ was constructed for sampling intervals of size $\log_{10} r = 0.2$, where $r \in \mathbb{R}^+$, using Eq. (4), and where x_i and x_j are hypocenter locations in Cartesian coordinates. The plot of

$\log_{10} C(s)$ against $\log_{10} s$ is expected to have a constant, positive slope equal to D_2 for all s due to the self-similarity of fractals (Grassberger, 1983). However, a finite set of hypocenter locations only approximates a true mathematical fractal. Given a plot of $\log_{10} C(s)$ against $\log_{10} s$ for a set of hypocenter locations, the slope will approach 0 at sufficiently small and large s values due to the finite number of earthquakes contained in any catalogue (finite size effect) and the absence of events outside of the study volume (boundary effect), respectively (Bonnet et al., 2001; Kagan, 2007). Both effects are demonstrated in Fig. 4, which shows the computation of the D_2 value for a finite sampling of a mathematical fractal. The range $1.0 \text{ km} \leq s \leq 10.0 \text{ km}$ is in general agreement with Wyss et al.'s (2004) range in s used to determine D_2 values for patches of the San Andreas Fault near the Parkfield section of California, where 0.23 $\text{km} \leq s \leq 17 \text{ km}$. Therefore, D_2 was estimated as the slope of the linear regression of $\log_{10} C(s)$ against $\log_{10} s$ for $1.0 \text{ km} \leq s \leq 10.0 \text{ km}$. The linear regression was calculated using MATLAB's polyfit function. Eq. (18) was used to estimate the error in D_2, σ_{D_2}.

Calculations - Temporal Variables

In this thesis, I performed three sets of calculations to produce three sets of variables: temporal variables, declustered variables, and spatial variables. This section and the following two sections detail the sequential order of operations used to produce each set of variables.

For the first set of calculations, I began with the unprocessed SCEDC catalogue. Non-earthquakes, which include quarry blasts, sonic booms, nuclear blasts, teleseismic events, and unknown events, were removed from the SCEDC catalogue. To ensure completeness, earthquakes with magnitudes below the maximum monthly M_c value of 2.5 (Fig. 3) were removed from the SCEDC catalogue. The Gutenberg-Richter distribution tends to have a break in linearity at high magnitudes due to the low occurrence

of large earthquakes. By visual inspection of the Gutenberg-Richter distribution for each year, this break in linearity typically occurred at or above a magnitude value of approximately 4.5. Consequently, earthquakes with magnitudes above 4.5 were removed from the SCEDC catalogue. Hypocenter locations in the SCEDC catalogue were transformed from geodetic to Cartesian coordinates. Henceforth, I defined all variables calculated in this section to be temporal variables. Finally, values for $b_{\mathbf{ML}}$, $\sigma_{b_{\mathbf{ML}}}$, $b_{\mathbf{LS}}$, $\sigma_{b_{\mathbf{LS}}}$, D_2, and σ_{D_2} were calculated for each month of each year in which at least 30 earthquakes occurred.

Calculations - Declustered Variables

For the second set of calculations, I began with the unprocessed SCEDC catalogue. Non-earthquakes were removed from the SCEDC catalogue. Earthquakes with magnitudes below 2.5 or above 4.5 were removed from the SCEDC catalogue. Hypocenter locations in the SCEDC catalogue were transformed from geodetic to Cartesian coordinates.

Foreshocks and aftershocks are earthquakes that occurred within some small distance and prior to and after a designated earthquake, respectively; the designated earthquake is called a mainshock (van Stiphout et al., 2012). In a declustering algorithm, earthquakes listed in a catalogue are categorized as foreshocks, mainshocks, and aftershocks, and earthquakes belonging to one or more of the chosen categories are removed, depending on the objective of the analysis (van Stiphout et al., 2012). As foreshocks and aftershocks tend to cluster in both space and time near their mainshocks, the removal of these seismicity clusters is aptly named declustering (van Stiphout et al., 2012). Past studies have reported anomalous changes in the fractal dimension value both before and after large earthquakes (Dimitriu et al., 2000; Roy and Nath, 2007; Mondal et al., 2019), and such changes were interpreted to be the result of changes in the clustering of foreshocks and aftershocks. Hence, I wished to know if

my analysis results change if I used a catalogue containing foreshocks and aftershocks as opposed to one with those events removed. In this thesis, I chose to remove only the foreshocks and aftershocks of $M \geq 7.0$ earthquakes because the anomalous changes in the fractal dimension values were typically reported for $M \geq 7.0$ earthquakes (Roy and Nath, 2007; Mondal et al., 2019).

The following approximation of Gardner and Knopoff's (1974) declustering algorithm, found in van Stiphout et al. (2012), was used:

(24) $$d = 10^{0.1238M+0.983} \text{ km}$$

(25) $$t = \begin{cases} 10^{0.032M+2.7389} \text{ days}, & M \geq 6.5 \\ 10^{0.5409M-0.547} \text{ days}, & M < 6.5 \end{cases},$$

where, for a magnitude M mainshock, d is the space window, and t is the time window. In Gardner and Knopoff's declustering algorithm, a foreshock was defined as an earthquake with an epicenter at most d km away from the mainshock's epicenter and with an origin time at most t days prior to the mainshock's origin time, whereas an aftershock was defined as an earthquake with an epicenter at most d km away from the mainshock's epicenter and with an origin time at most t days after the mainshock's origin time. Although other declustering algorithms exist (Reasenberg, 1985; Zhuang et al., 2002), Gardner and Knopoff's declustering algorithm was chosen due to the simple nature of its application. Henceforth, I define all variables calculated in this section to be declustered variables. After declustering, a value for $b_{\mathbf{ML}}$, $\sigma_{b_{\mathbf{ML}}}$, $b_{\mathbf{LS}}$, $\sigma_{b_{\mathbf{LS}}}$, D_2, and σ_{D_2} was calculated for each month of each year in which at least 30 earthquakes occurred.

Calculations - Spatial Variables

For the third set of calculations, I began with the unprocessed SCEDC catalogue. Non-earthquakes were removed from the SCEDC catalogue. Earthquakes with magnitudes above 4.5 were removed. Earthquakes with magnitudes below 2.3 were removed because the maximum yearly M_c value was 2.3 (Fig. 3). Hypocenter locations were transformed from geodetic to Cartesian coordinates. Henceforth, I defined all variables calculated in this section to be spatial variables. For each year, the study volume was partitioned into a square pattern mesh grid of 0.1° latitude by 0.1° longitude cells. For each cell containing 100 or more earthquakes within a 100 km radius, a $b_{\mathbf{LS}}$, $\sigma_{b_{\mathbf{LS}}}$, $b_{\mathbf{ML}}$, $\sigma_{b_{\mathbf{ML}}}$, D_2, and σ_{D_2} were calculated using the nearest 100 earthquakes. Declustered variations of these spatial distribution maps of b and D_2 values were not produced due to an insufficient number of events in the foreshock-aftershock zones after declustering.

Results

<div align="center">TEMPORAL RESULTS</div>

Temporal $b_{\mathbf{ML}}$ values ranged from 0.49 to 2.40 with an average of 1.28 ± 0.27 (Table 1; Fig. 5). Temporal $b_{\mathbf{LS}}$ values ranged from 0.67 to 2.01 with an average of 1.11 ± 0.23 (Table 1; Fig. 5). Temporal $\sigma_{b_{\mathbf{LS}}}$ values ranged from 0.03 to 0.27 with an average of 0.09 ± 0.04, whereas temporal $\sigma_{b_{\mathbf{ML}}}$ values had a wider range between 0.02 and 0.42 with a higher average of 0.17 ± 0.06 (Table 1; Fig. 5). 62% of temporal $\sigma_{b_{\mathbf{LS}}}$ values were below 0.1, whereas only 10% of temporal $\sigma_{b_{\mathbf{ML}}}$ values were below 0.1 (Fig. 5). The higher proportion of low values for temporal $\sigma_{b_{\mathbf{ML}}}$ would suggest that temporal $b_{\mathbf{LS}}$ values should be used for assessing changes in the temporal b value. The temporal trend in $b_{\mathbf{LS}}$ values was characterized by a high frequency of increases and decreases, with higher $b_{\mathbf{LS}}$ values occurring prior to 2003 (Fig. 6), reflecting a decrease in the predominance of small earthquakes after 2003.

Temporal D_2 values ranged from 0.03 to 2.12 with an average of 0.52 ± 0.40 (Table 1; Fig. 7). Temporal σ_{D_2} values ranged from 0.00 to 0.14 with an average of 0.04 ± 0.02 (Table 1; Fig. 7), suggesting a good fit of the fractal model to the set of earthquake hypocenters.

There was a predominant pattern in temporal D_2 values on the dates of and after $M > 6.0$ earthquakes:

(1) For the 1983 M 6.1 Coalinga earthquake, the temporal D_2 value was 0.14 a month prior to the earthquake (Fig. 8). The temporal D_2 value increased to 1.44 on the month of the earthquake, before decaying for one month to 0.37 (Fig. 8).

(2) For the 1987 M 6.6 Superstition Hills earthquake, the temporal D_2 value was 0.84 a month prior to the earthquake (Fig. 8). The temporal D_2 value

increased to 1.84 on the month of the earthquake, before decaying for four months to 0.39 (Fig. 8).

(3) For the 1992 M 6.1 Joshua Tree earthquake, the temporal D_2 value was 0.31 a month prior to the earthquake (Fig. 8). The temporal D_2 value increased to 1.89 on the month of the earthquake, before decaying for one month to 1.54 (Fig. 8).

(4) For the 1992 M 7.3 Landers earthquake, the temporal D_2 value was 1.54 a month prior to the earthquake (Fig. 8). The temporal D_2 value increased to 1.76 on the month of the earthquake, before decaying for four months to 0.99 (Fig. 8).

(5) For the 1994 M 6.7 Northridge earthquake, the temporal D_2 value was 0.34 a month prior to the earthquake (Fig. 8). The temporal D_2 value increased to 2.06 on the month of the earthquake, before decaying for seven months to 0.17 (Fig. 8).

(6) For the 1999 M 7.1 Hector Mine earthquake, the temporal D_2 value was 0.46 a month prior to the earthquake (Fig. 8). The temporal D_2 value increased to 1.72 on the month of the earthquake, before decaying for four months to 0.37 (Fig. 8).

(7) For the 2003 M 6.5 San Simeon earthquake, the temporal D_2 value was 0.27 a month prior to the earthquake (Fig. 8). The temporal D_2 value increased to 1.30 on the month of the earthquake, before decaying for at least four months to 0.21 (Fig. 8).

(8) For the 2010 M 7.2 El Mayor-Cucapah earthquake, the temporal D_2 value was 0.35 a month prior to the earthquake (Fig. 8). The temporal D_2 value increased to 2.12 on the month of the earthquake, before decaying for thirteen months to 0.23 (Fig. 8).

(9) For the 2019 M 7.1 Ridgecrest earthquake, the D_2 value was 0.42 a month prior to the earthquake (Fig. 8). The D_2 value increased to 2.00 on the month of the earthquake, before decaying for seven months to 0.41 (Fig. 8).

In summary, temporal D_2 values increased by a value in the range 0.22 to 1.77 from the month prior to and of the occurrence of a $M > 6.0$ earthquake (Fig. 8). After the occurrence of a $M > 6.0$ earthquake, temporal D_2 values decayed for one to thirteen months to a value in the range 0.17 to 0.99 (Fig. 8).

Declustered Results

The spatial and temporal windows used in Gardner and Knopoff's declustering algorithm ranged from 53 km to 77 km and 499 days to 939 days. There was a predominant pattern in declustered D_2 values on the dates of and after most $M > 7.0$ earthquakes:

(1) For the 1992 M 7.3 Landers earthquake, declustered D_2 values were lower than their corresponding temporal D_2 values on the month of the earthquake and for eight months after the earthquake (Fig. 9).

(2) For the 1999 M 7.1 Hector Mine earthquake, declustered D_2 values were lower than their corresponding temporal D_2 values on the month of the earthquake and for six months after the earthquake (Fig. 9).

(3) For the 2010 M 7.2 El Mayor-Cucapah earthquake, declustered D_2 values were lower than their corresponding temporal D_2 values on the month of the earthquake and for fifteen months after the earthquake (Fig. 9).

(4) For the 2019 M 7.1 Ridgecrest earthquake, less than 30 $M \geq 2.5$ earthquakes occurred on the month of the earthquake and for nine months after the earthquake. Consequently, no declustered D_2 values were calculated on the month of the earthquake and for nine months after the earthquake (Fig. 9).

In summary, declustered D_2 values were lower than temporal D_2 values on the months in which a $M > 7.0$ earthquake occurred and for six to fifteen months after the

occurrence of a $M > 7.0$ earthquake, with the exception of the 2019 M 7.1 Ridgecrest earthquake due to an insufficient number of earthquakes after declustering (Fig. 9). That is, aftershocks appear to increase the D_2 value.

Spatial Results

Spatial $b_{\mathbf{ML}}$ values ranged from 0.47 to 4.10 with an average of 1.27 ± 0.30 (Table 2; Fig. 10). Spatial $b_{\mathbf{LS}}$ values ranged from 0.60 to 3.50 with an average of 1.11 ± 0.24 (Table 2; Fig. 10). Spatial $\sigma_{b_{\mathbf{LS}}}$ values ranged from 0.01 to 0.41 with an average of 0.10 ± 0.04, whereas spatial $\sigma_{b_{\mathbf{ML}}}$ values had a wider range between 0.03 to 0.58 with a higher average of 0.14 ± 0.05 (Table 2; Fig. 10). 19% of spatial $\sigma_{b_{\mathbf{LS}}}$ values were below 0.1, whereas only 5% of spatial $\sigma_{b_{\mathbf{ML}}}$ values were below 0.1 (Fig. 10). The higher proportion of low values for spatial $\sigma_{b_{\mathbf{ML}}}$ would suggest that spatial $b_{\mathbf{LS}}$ values should be used for reporting changes in the spatial b value.

Assuming that foreshocks and aftershocks are producing anomalous changes in the b and D_2 value, for each $M > 6.0$ earthquake a spatial window of 77 km about that earthquake's epicenter was used to record changes in spatial $b_{\mathbf{LS}}$ and spatial D_2 values relative to the timing of that earthquake. The value 77 km was chosen because it was the maximum distance expected for foreshocks and aftershocks as defined in Gardner and Knopoff's declustering algorithm.

For spatial $b_{\mathbf{LS}}$ values:

(1) For the 1983 M 6.1 Coalinga earthquake, the mean spatial $b_{\mathbf{LS}}$ value increased from 0.93 in 1983 to 1.00 in 1984 (Fig. 11). No earthquakes occurred within a 77 km window of the earthquake's epicenter in 1982 (Fig. 11).

(2) For the 1987 M 6.6 Superstition Hills earthquake, the mean spatial $b_{\mathbf{LS}}$ value increased from 1.32 in 1986 to 1.36 in 1987, before decreasing to 1.28 in 1988 (Fig. 11). An analysis of spatial $b_{\mathbf{LS}}$ and D_2 values was not performed for the

1987 M 6.2 Elmore Ranch earthquake, because it was considered a foreshock of the 1987 M 6.6 Superstition Hills earthquake.

(3) For the 1992 M 7.3 Landers earthquake, the mean spatial $b_{\mathbf{ML}}$ value for a 77 km window about the epicenter was 1.28 in 1987 and increased to 1.56 in 1988 (Fig. 12). From 1988 to 1992, the mean spatial $b_{\mathbf{ML}}$ value for a 77 km window about the epicenter monotonically decreased to 1.04, before increasing to 1.26 in 1993 (Fig. 12). An analysis of spatial $b_{\mathbf{LS}}$ and D_2 values was not performed for the 1992 M 6.1 Joshua Tree earthquake or the 1992 M 6.3 Big Bear earthquake, which were considered as foreshocks and aftershocks of the 1992 M 7.3 Landers earthquake.

(4) For the 1994 M 6.7 Northridge earthquake, the mean spatial $b_{\mathbf{LS}}$ value for a 77 km window about the epicenter decreased from 1.22 in 1993 to 0.94 in 1994, before increasing to 0.99 in 1995 (Fig. 11).

(5) For the 1999 M 7.1 Hector Mine earthquake, the mean spatial $b_{\mathbf{LS}}$ value for a 77 km window about the epicenter was 1.22 in 1994 (Fig. 12). From 1994 to 1996, the mean spatial $b_{\mathbf{LS}}$ value for a 77 km window about the epicenter monotonically decreased to 0.92, before monotonically increasing to 1.22 in 1998 (Fig. 12). From 1998 to 1999, the mean spatial $b_{\mathbf{LS}}$ value for a 77 km window about the epicenter decreased to 1.05, before monotonically increasing to 1.28 in 2001 (Fig. 12).

(6) For the 2003 M 6.5 San Simeon earthquake, the mean spatial $b_{\mathbf{LS}}$ value for a 77 km window about the epicenter increased from 0.84 in 2003 to 0.88 in 2004 (Fig. 11).

(7) For the 2010 M 7.2 El Mayor-Cucapah earthquake, the mean spatial $b_{\mathbf{LS}}$ value for a 77 km window about the epicenter was 1.23 in 2005 (Fig. 12). The mean spatial $b_{\mathbf{LS}}$ value for a 77 km window about the epicenter decreased to 0.96 in 2006, before increasing to 1.08 in 2011 (Fig. 12). From 2006 to 2010, the

mean spatial b_{LS} value for a 77 km window about the epicenter monotonically decreased to 0.92, before monotonically increasing to 1.18 in 2014 (Fig. 12).

(8) For the 2019 M 7.1 Ridgecrest earthquake, the mean spatial b_{LS} value for a 77 km window about the epicenter increased from 0.95 to 0.99, before increasing to 1.01 in 2020 (Fig. 12).

In summary, the mean spatial b_{LS} values within the foreshock-aftershock zone of a $M > 6.0$ earthquake tended to decrease from the year prior to and of the occurrence of a $M > 6.0$ earthquake, before increasing for the following year (Fig. 11; Fig. 12).

Spatial D_2 values ranged from 0.11 to 1.84 with an average of 0.82 ± 0.27 (Table 2; Fig. 13). Spatial σ_{D_2} values ranged from 0.00 to 0.20 with an average of 0.06 ± 0.03 (Table 2; Fig. 13), suggesting a good fit of the fractal model to the set of earthquake hypocenters.

For spatial D_2 values:

(1) For the 1983 M 6.1 Coalinga earthquake, the mean spatial D_2 value for a 77 km window about the epicenter monotonically decreased from 1.49 in 1983 to 0.78 in 1988 (Fig. 14).

(2) For the 1987 M 6.6 Superstition Hills earthquake, the mean spatial D_2 value for a 77 km window about the epicenter monoyonically increased from 0.69 in 1985 to 1.07 in 1987, before monotonically decreasing to 0.73 in 1990 (Fig. 14).

(3) For the 1992 M 7.3 Landers earthquake, the mean spatial D_2 value for a 77 km window about the epicenter monotonically increased from 0.45 in 1991 to 1.23 in 1993, before decreasing to 0.84 in 1995 (Fig. 15).

(4) For the 1994 M 6.7 Northridge earthquake, the mean spatial D_2 value for a 77 km window about the epicenter monotonically increased from 0.47 in 1992 to 1.25 in 1994, before monotonically decreasing to 0.50 in 1998 (Fig. 14).

(5) For the 1999 M 7.1 Hector Mine earthquake, the mean spatial D_2 value for a 77 km window about the epicenter monotonically increased from 0.73 in 1998 to 1.10 in 2000, before monotonically decreasing to 0.62 in 2004 (Fig. 15).

(6) For the 2003 M 6.5 San Simeon earthquake, the mean spatial D_2 value for a 77 km window about the epicenter increased from 0.44 in 2001 to 1.38 in 2003, before decreasing to 0.86 in 2007 (Fig. 14).

(7) For the 2010 M 7.2 El Mayor-Cucapah earthquake, the mean spatial D_2 value for a 77 km window about the epicenter monotonically increased from 0.95 in 2007 to 1.45 in 2010, before monotonically decreasing to 1.33 in 2012 (Fig. 15).

(8) For the 2019 M 7.1 Ridgecrest earthquake, the mean spatial D_2 value for a 77 km window about the epicenter increased from 0.67 in 2018 to 1.18 in 2019, before further increasing to 1.23 in 2020 (Fig. 15).

In summary, the mean spatial D_2 values within the foreshock-aftershock zone of a $M > 6.0$ earthquake tended to increase from the year prior to and of the occurrence of a $M > 6.0$ earthquake, before generally decreasing in one or more years afterwards (Fig. 14; Fig. 15).

FRACTAL RESULTS

The data depicted in some of the scatter plots of $\log_{10} C(s)$ against $\log_{10} s$ did not demonstrate a constant, positive linear trend for the entire range 1 km $\leq s \leq$ 10 km (Fig. 16). For example, the data in the scatter plots of $\log_{10} C(s)$ against $\log_{10} s$ may have begun a gradient increase at $s > 0.1$ km or a gradient decrease at $s < 0.1$ km (Fig. 16), which may produce a less accurate measurement of D_2. As shown by the example of a finite sample of the Sierpinski triangle (Fig. 4), for any finite sampling of a fractal set, the data depicted in the scatter plot of $\log_{10} C(s)$ against $\log_{10} s$ should follow an S-shaped curve. However, a number of D_2 calculations involved scatter plots of $\log_{10} C(s)$ against $\log_{10} s$ with data that followed double S-shaped curves,

which was peculiar as no previous studies have reported such an observation. The presence of multiple slopes or fractal dimensions is interpreted to suggest that the set of earthquake hypocenters is multifractal. Alternatively, the presence of multiple slopes may be due to an insufficient number of earthquakes.

Discussion

The purpose of this study was to identify, if any, temporal or spatial patterns in b and D_2 values for southern California seismicity from 1982 to 2020, as recorded in the SCEDC catalogue. In particular, precursory changes in b and D_2 values prior to large earthquakes were desired. However, no consistent and easily identifiable precursory changes in b and D_2 values were identified in the results of this study. Instead, consistent and easily identifiable changes in b and D_2 values were found on the dates of and after large earthquakes.

Some studies have interpreted the D_2 value of earthquake locations to be an indication of the degree of spatial clustering of those earthquake locations, with low D_2 values being associated with high clustering and high D_2 values being associated with low clustering (Dimitriu et al., 2000; Oncel and Wilson, 2002; Han et al., 2015; Mondal et al., 2019; Radziminovich et al., 2019). That is, there exists a negative correlation between the D_2 value and degree of clustering of earthquake locations. However, my declustering results suggest the opposite. After declustering, a process that decreases the degree of clustering of earthquake locations, the declustered D_2 values for months in which declustering had occurred were lower than their corresponding temporal D_2 values (Fig. 9). Instead of a negative correlation, this decrease in D_2 values after declustering suggests that there exists a positive correlation between the D_2 value and degree of clustering of earthquake locations. Indeed, Öztürk (2012) had reported high D_2 values to be associated with the largest earthquakes contained in a set of 99,737 earthquakes that occurred in Turkey from 1970 to 2011, and interpreted high D_2 values to be an indication of a stronger clustering of epicenters. Possible causes for an increase in clustering of epicenters include swarms, foreshocks, and aftershocks. Large earthquakes may be preceded by a cluster of earthquakes termed foreshocks. Hence, if foreshocks preceded a large earthquake, and if there exists a positive correlation between the D_2 value and degree of clustering of earthquake locations, then

an increase in the D_2 value could be a precursor to a large earthquake. There have been increases in the temporal D_2 values prior to large earthquakes (Fig. 8), but no increases in the spatial D_2 values prior to large earthquakes (Fig. 14; Fig. 15); that is, any increase in the D_2 values prior to large earthquakes was caused by seismicity outside of their foreshock-aftershock window as defined in Gardner and Knopoff's algorithm. Additionally, the results of this thesis show both an increase and decrease in D_2 values prior to large earthquakes (Fig. 8), and hence the role for either the increase or decrease in the D_2 value as a precursor for large earthquakes remains unclear.

Other studies have interpreted the D_2 value of earthquake locations to be an indication of the geometry of the spatial distribution of those earthquake locations: D_2 values close to 0 imply a set of earthquake locations describing a point, D_2 values close to 1 imply a set of earthquake locations describing a line, D_2 values close to 2 imply a set of earthquake locations describing a surface, and D_2 values close to 3 imply a set of earthquake locations describing a volume (Tosi et al., 2008; Radziminovich et al., 2019). Fig. 17 illustrates this difference in D_2 values due to a difference in geometry as well as the effect of scattering, which decreases the D_2 value. In this thesis, prior to declustering the D_2 values for dates within the temporal window of the aftershock sequences of $M > 7.0$ earthquakes approached or exceeded 2.0 (Fig. 9), implying sets of hypocenters describing surfaces. After declustering, the corresponding D_2 values decreased to values within the range [0.06, 1.38] (Fig. 9), implying sets of hypocenters describing points and lines. That is, aftershocks of large earthquakes tend to occupy surfaces in space, in contrast to the collection of earthquakes outside of aftershocks which tend to occupy points or lines in space and reflect locations that are more spatially random. Indeed, one of the effects of Gardner and Knopoff's declustering algorithm is to reduce a non-Poissonian distribution containing dependent events into a Poissonian distribution containing independent events, in which the dependent events were aftershocks (Gardner and Knopoff, 1974). There is an empirical law, the

Omori-Utsu law, which describes observed temporal trends in the aftershock rates of mainshocks as

$$(26) \qquad n(t) = \frac{K}{(c+t)^p},$$

where $n(t)$ is the number of aftershocks per unit time, t is the time after the main-shock, and K, c, p are constants (Utsu, 1961). That is, the aftershock rate is typically highest immediately after a mainshock and subsequently decays with time. Hence, the increase in D_2 values on the months of the $M > 7.0$ earthquakes and the subsequent decay in D_2 values within the temporal window of the aftershock sequences of the $M > 7.0$ earthquakes are interpreted to be a result of the temporal decay in the aftershock rate as described by the Omori-Utsu law. Both the Omori-Utsu law and the results from declustering suggest that the increased D_2 values on the months of the $M > 7.0$ earthquakes and the subsequent decay in D_2 values within the temporal window of the aftershock sequences of the $M > 7.0$ earthquakes were correlated with the aftershock activity. Physically, on the months of large earthquakes, a high dimension set of strongly clustered and surface distributed aftershocks superimpose onto a lower dimension set of weakly clustered, spatially random earthquakes. Although no precursory pattern in D_2 values occurred prior to large earthquakes, the large increase and subsequent decay in D_2 values after a large earthquake may provide a use in defining aftershocks using a quantitative measure. The identification of aftershocks is necessary to obtain reliable seismic hazard assessments (Fereidoni and Atskinson, 2014).

Some studies have suggested a potential role for either the increase or decrease in the b value as a precursor for large earthquakes (Smith, 1981; Smith, 1986; de Arcangelis et al., 2016). Smith (1981) observed a monotonic increase in $b_{\mathbf{ML}}$ value from 1.0 in 1970 to 1.9 in 1974 for a set of $M \geq 4.0$ earthquakes that occurred in a 2° latitude by 2° longitude region in New Zealand, prior to a monotonic decrease in $b_{\mathbf{ML}}$

value until 1979; a M 6.0 earthquake occurred in 1977 when $b_{\mathbf{ML}}$ was close to 1.4, suggesting an increase in b value to be a precursor for large earthquakes. In contrast, Nanjo et al. (2012) observed a monotonic decrease in $b_{\mathbf{ML}}$ value from about 0.9 in 2005 to about 0.4 in 2011 for a set of $M \geq 2.5$ earthquakes that occurred close to the epicenter of the 2011 $M_{\mathbf{w}}$ 9.0 Tohoku earthquake in Japan, suggesting a decrease in b value to be a precursor for large earthquakes. The results in this thesis showed both an increase and decrease in $b_{\mathbf{LS}}$ values prior to and within a 77 km window of the epicenters of several $M > 6.0$ earthquakes (Fig. 11; Fig. 12). Hence, the role for either the increase or decrease in the b value as a precursor for large earthquakes remains dubious.

The increase in $b_{\mathbf{LS}}$ values immediately after a majority of the $M > 6.0$ earthquakes and all of the $M > 7.0$ earthquakes (Fig. 11; Fig. 12) is consistent with observations in literature (Gulia et al., 2018). It has been shown that there exists an inverse relationship between b values and stress (Scholz, 2015). Therefore, the decrease in spatial $b_{\mathbf{LS}}$ values that occurred in the years of the $M > 6.0$ earthquakes may be suggestive of an increase in stress within the aftershock zone of the eventual $M > 6.0$ earthquakes, and the increase in spatial $b_{\mathbf{LS}}$ values that occurred on the year after the $M > 6.0$ earthquakes may be suggestive of stress released from the aftershock zones as a result.

There has been much debate regarding the existence of a relationship between the fractal dimension and b value, with both positive (Oncel and Wilson, 2002; Oncel and Wilson, 2004; Wyss et al., 2004; Mandal and Rastogi, 2005; Chen et al., 2006; Roy et al., 2011; Han et al., 2015; Mandal et al., 2021) and negative relationships (Hirata, 1989; Öncel et al., 1996; Oncel and Wilson, 2002; Mandal and Rastogi, 2005; Öztürk, 2012; Mandal et al., 2021) being reported in past studies in various geologic settings in the world. In this thesis, a linear regression between the temporal $b_{\mathbf{LS}}$

values and temporal D_2 values yields the equation $D_2 = 0.22b_{\mathbf{LS}} + 0.28$ with a correlation coefficient of 0.12 (Fig. 18), suggesting a weak positive correlation between D_2 values and b values. However, if one were to restrict the previous linear regression to D_2 values and b values that occurred on months in which $M > 6.0$ earthquakes occurred in, then the linear regression would yield the equation $D_2 = 1.90b_{\mathbf{LS}} - 0.24$ with a correlation coefficient of 0.82 (Fig. 18), suggesting a strong positive correlation between D_2 values and b values. Hence, there may indeed exist a relationship between the fractal dimension and b value; however, the strength of this relationship may vary temporally and depend on the occurrence of large earthquakes. Indeed, Legrand (2002) had proposed that the value of c in the equation $D = 3b/c$ (Aki, 1981) is not necessarily 1.5 and instead depends upon the sizes of the earthquakes, where $c = 1$, 1.5, and 2 for small, intermediate, and large earthquakes, respectively. Sianturi et al. (2019) had proposed $c = 3$ for crystalline rocks and 2.4 for subduction zones, which suggests that the relationship between the fractal dimension and b value may vary spatially due to a dependence on material heterogeneity. Assuming $D = 3b/c$ (Aki, 1981), then the results in this thesis would suggest that the spatial c values do vary spatially, ranging between 1.73 to 13.81 with 98% of the spatial c values being greater than 2 (Fig. 19). If a relationship between the fractal dimension and b value does exist, then it is not as simple as the one proposed by Aki (1981).

Both results in literature (Öncel et al., 1996; Tosi, 1998; Wyss et al., 2004; Mandal and Rastogi, 2005; Roy and Nath, 2007; Tosi et al., 2008; Radziminovich et al., 2019; Tiwari et al., 2021) and the results in this thesis (Fig. 16) have demonstrated that the set of earthquake locations are fractal within specific ranges of length scales. Öncel et al. (1996) demonstrated that sets of earthquake epicenters in the Anatolian fault zones of Turkey obeyed fractal scaling for the range 5 km $< s <$ 160 km. Similarly, Roy and Nath (2007) demonstrated that a set of earthquake epicenters in the Sumatra-Andaman region obeyed fractal scaling for the range 5 km $< s <$ 50 km.

However, Wyss et al. (2004) obtained different results for ranges of length scales for fractal scaling when they demonstrated that sets of earthquake hypocenters in the Parkfield section of the San Andreas fault obeyed fractal scaling for the ranges 0.23 km $< s < 2.7$ km, 0.3 km $< s < 5.2$ km, 1 km $< s < 6.2$ km, 1 km $< s < 6$ km, 0.3 km $< s < 6$ km, and 1 km $< s < 17$ km. That is, the finite size effect and the boundary effect occurred at different length scales for different areas in the Parkfield section as defined in Wyss et al. (2004). Furthermore, Tosi (1998) proposed a break in fractal scaling for a set of earthquake epicenters in Central Italy, suggesting that the set was fractal separately for the ranges 0.5 km $< s < 7$ km and 8 km $< s < 56$ km. Similarly, the results of this thesis have demonstrated a difference in range of length scales in which earthquake locations obey fractal scaling. For example, for the determination of spatial D_2 values for the year 2019, fractal scaling occurred for the range $0 < \log_{10} s < 1$ or 1 km $< s < 10$ km in one cell while a different cell had fractal scaling at the range $-0.20 < \log_{10} s < 0.60$ or 0.63 km $< s < 3.98$ km (Fig. 16), suggesting that the range in which fractal scaling occurs for a real fractal varies spatially.

Conclusion

Temporal b values and D_2 values were calculated for subsets of earthquakes contained in the SCEDC catalogue with magnitudes between 2.3 and 4.5 (inclusive).

(1) Temporal $b_{\mathbf{ML}}$ values ranged from 0.49 to 2.40 with an average of 1.28 ± 0.27.

(2) Temporal $b_{\mathbf{LS}}$ values ranged from 0.67 to 2.01 with an average of 1.11 ± 0.23.

(3) Temporal D_2 values ranged from 0.03 to 2.12 with an average of 0.52 ± 0.40.

Spatial b values and D_2 values were calculated for the set of all earthquakes listed in the SCEDC catalogue with magnitudes between 2.5 and 4.5 (inclusive).

(1) Spatial $b_{\mathbf{ML}}$ values ranged from 0.47 to 4.10 with an average of 1.27 ± 0.30.

(2) Spatial $b_{\mathbf{LS}}$ values ranged from 0.60 to 3.50 with an average of 1.11 ± 0.24.

(3) Spatial D_2 values ranged from 0.11 to 1.84 with an average of 0.82 ± 0.27.

No consistent and easily identifiable changes in b or D_2 values were found prior to the occurrence of large earthquakes, that is, no precursory changes in b and D_2 values were found in the result of this study. Instead, consistent and easily identifiable changes in b and D_2 values were found on the dates of and after large earthquakes. b values decreased whereas D_2 values increased between the years prior to and of $M > 6.0$ earthquakes, suggesting an increase in stress and the presence of strongly clustered aftershocks distributed along a surface (Fig. 20; Fig. 21). b values increased whereas D_2 values decreased after the occurrence of $M > 6.0$ earthquakes, suggesting stress release and a decay in the rate of aftershocks as seismicity returns to a more spatially random and weakly clustered set of earthquakes (Fig. 20; Fig. 21). These consistent and easily identifiable changes in b and D_2 values for the dates of and after large earthquakes reveal patterns tied to aftershock behavior, and, consequently, may possess applications in understanding aftershocks and seismic hazard.

Tables

Table 1: Values for temporal variables were determined for monthly sets of earthquake hypocenters contained in the SCEDC catalogue (without declustering) for each month from 1982 to 2020.

Values for Temporal Variables				
Variable	Minimum	Maximum	Average	Standard Deviation
$b_{\mathbf{ML}}$	0.49	2.40	1.28	0.27
$\sigma_{b_{\mathbf{ML}}}$	0.02	0.42	0.17	0.06
$b_{\mathbf{LS}}$	0.67	2.01	1.11	0.23
$\sigma_{b_{\mathbf{LS}}}$	0.03	0.27	0.09	0.04
D_2	0.03	2.12	0.52	0.40
σ_{D_2}	0.00	0.14	0.04	0.02

Table 2: Values for spatial variables were determined for yearly sets of earthquake hypocenters contained in the SCEDC catalogue (without declustering) for each $0.1°$ latitude by $0.1°$ longitude cell for each year from 1982 to 2020.

Values for Spatial Variables				
Variable	Minimum	Maximum	Average	Standard Deviation
$b_{\mathbf{ML}}$	0.47	4.10	1.27	0.30
$\sigma_{b_{\mathbf{ML}}}$	0.03	0.58	0.14	0.05
$b_{\mathbf{LS}}$	0.60	3.50	1.11	0.24
$\sigma_{b_{\mathbf{LS}}}$	0.01	0.41	0.10	0.04
D_2	0.11	1.84	0.82	0.27
σ_{D_2}	0.00	0.20	0.06	0.03

Figures
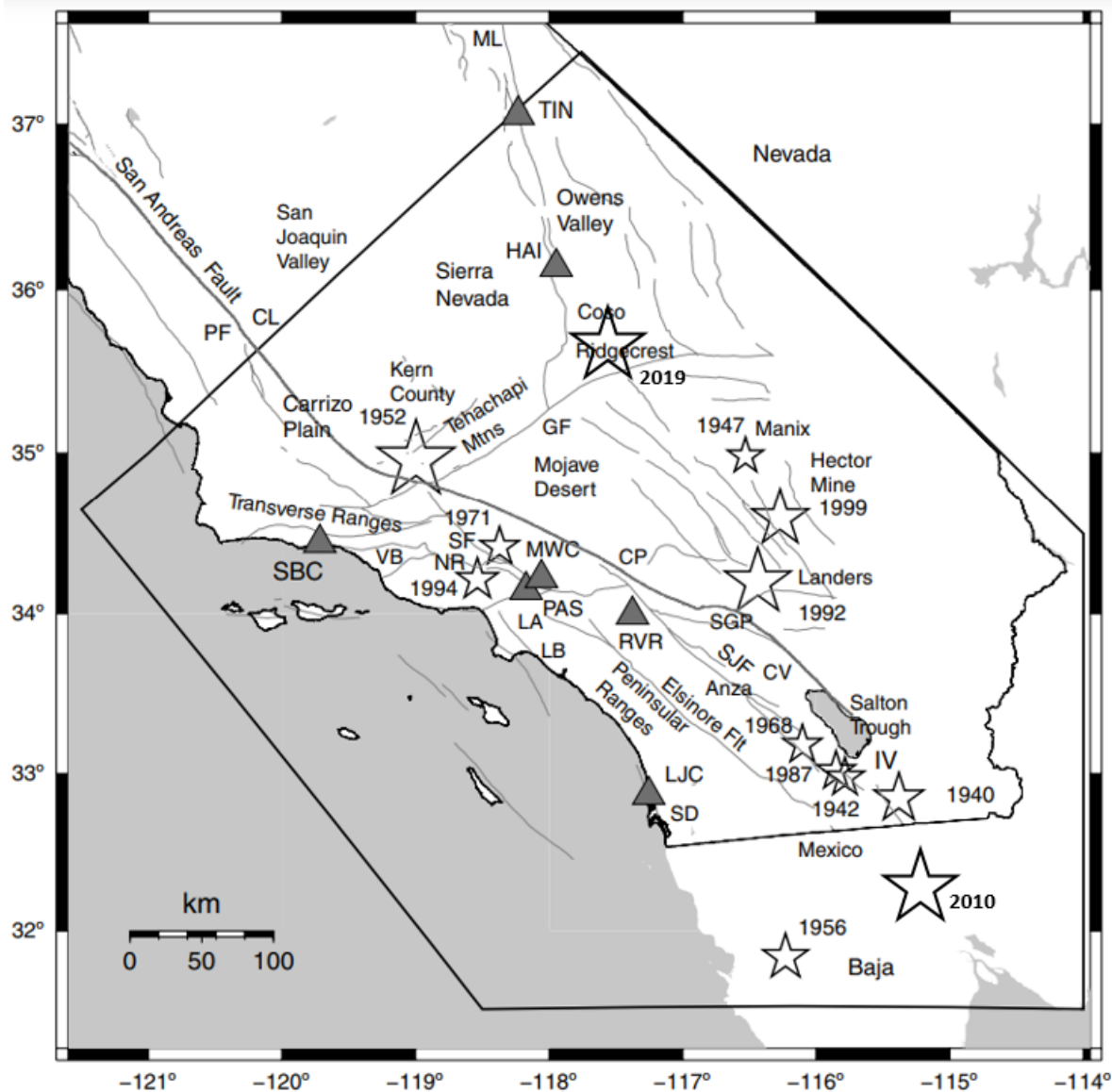
FIGURE 1. For 1932 to 2020, map of the SCSN coverage area (pentagon), the oldest seven stations of the SCSN (triangles), and $M_{\mathbf{w}} \geq 6.5$ earthquakes (stars) (Edited from Hutton et al., 2010).
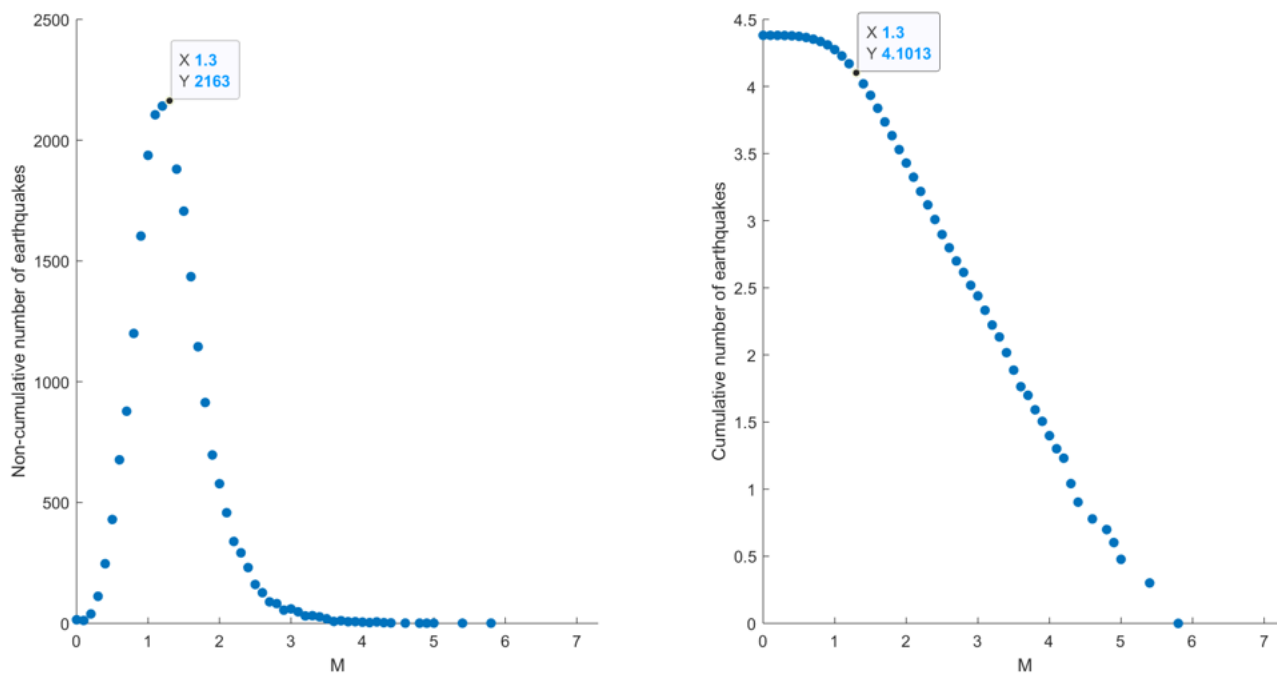
FIGURE 2. Sample estimation of the $M_{\mathbf{c}}$ for the SCEDC catalogue in 1995 using the Maximum Curvature Method. The figure to the left shows the non-cumulative number of earthquakes. The figure to the right shows the base 10 logarithm of the cumulative number of earthquakes. A M value of 1.3 corresponds to the maximum non-cumulative frequency, so the $M_{\mathbf{c}} = 1.3 + 0.2 = 1.5$.
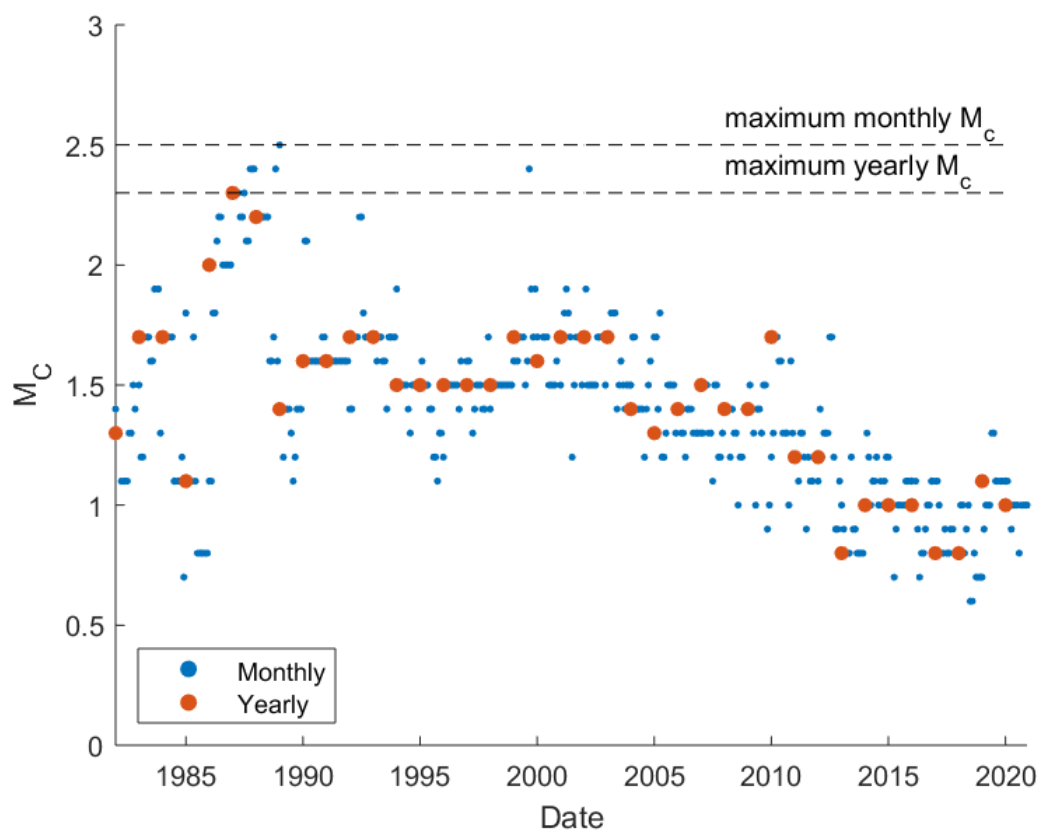
FIGURE 3. Evolution of monthly M_c and yearly M_c values for the SCEDC catalogue.

The Sierpinksi triangle, a fractal with fractal dimension $D = \dfrac{\log 3}{\log 2} \approx 1.59$

$\log_{10} C(s) = 1.52\log_{10} s - 2.90$

$D_2 \approx 1.52$

D_2 approximation
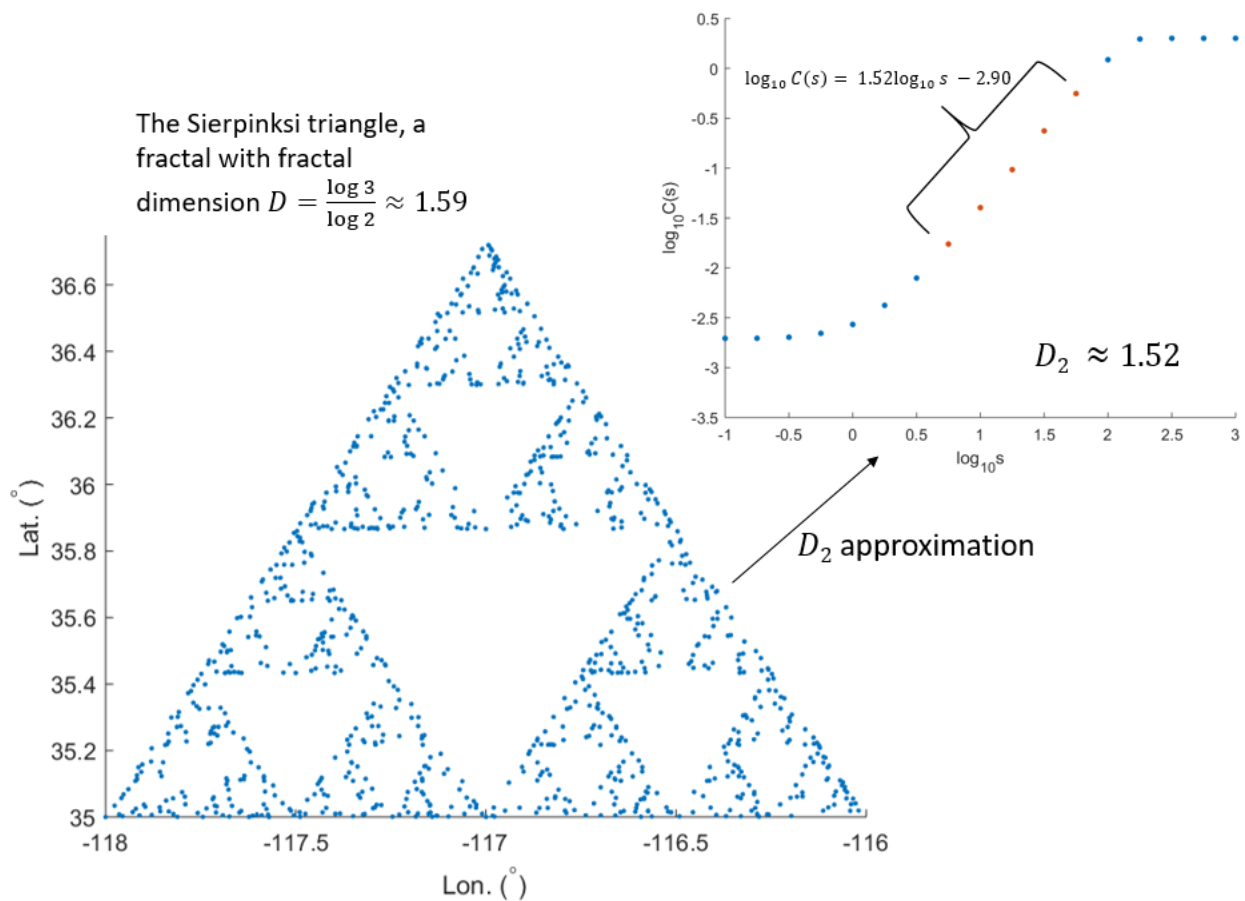
FIGURE 4. A finite sample of the Sierpinski triangle, a fractal in mathematics, and its associated scatter plot of $\log_{10} C(s)$ against $\log_{10} s$. The correlation dimension, D_2, one of many notions of fractal dimension, D, is equal to the slope in which the scatter plot follows a positive, constant slope.
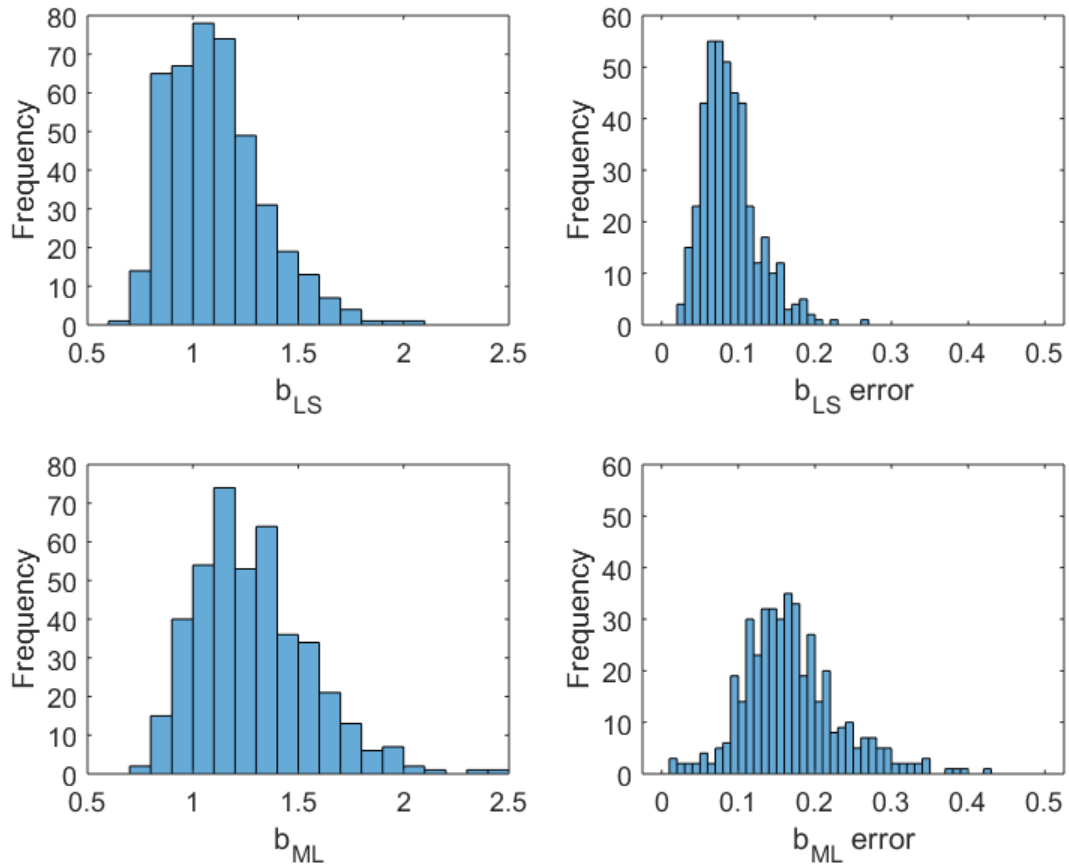
FIGURE 5. Distribution of temporal b_{LS}, b_{ML}, $\sigma_{b_{LS}}$, and $\sigma_{b_{ML}}$ values. These values were determined for sets of earthquake hypocenters contained in the SCEDC catalogue (without declustering) for each month from 1982 to 2020. Temporal $\sigma_{b_{LS}}$ values tended to be lower than temporal $\sigma_{b_{ML}}$ values, with most of the temporal $\sigma_{b_{LS}}$ values being lower than 0.1, whereas most of the temporal $\sigma_{b_{ML}}$ values were higher than 0.1.
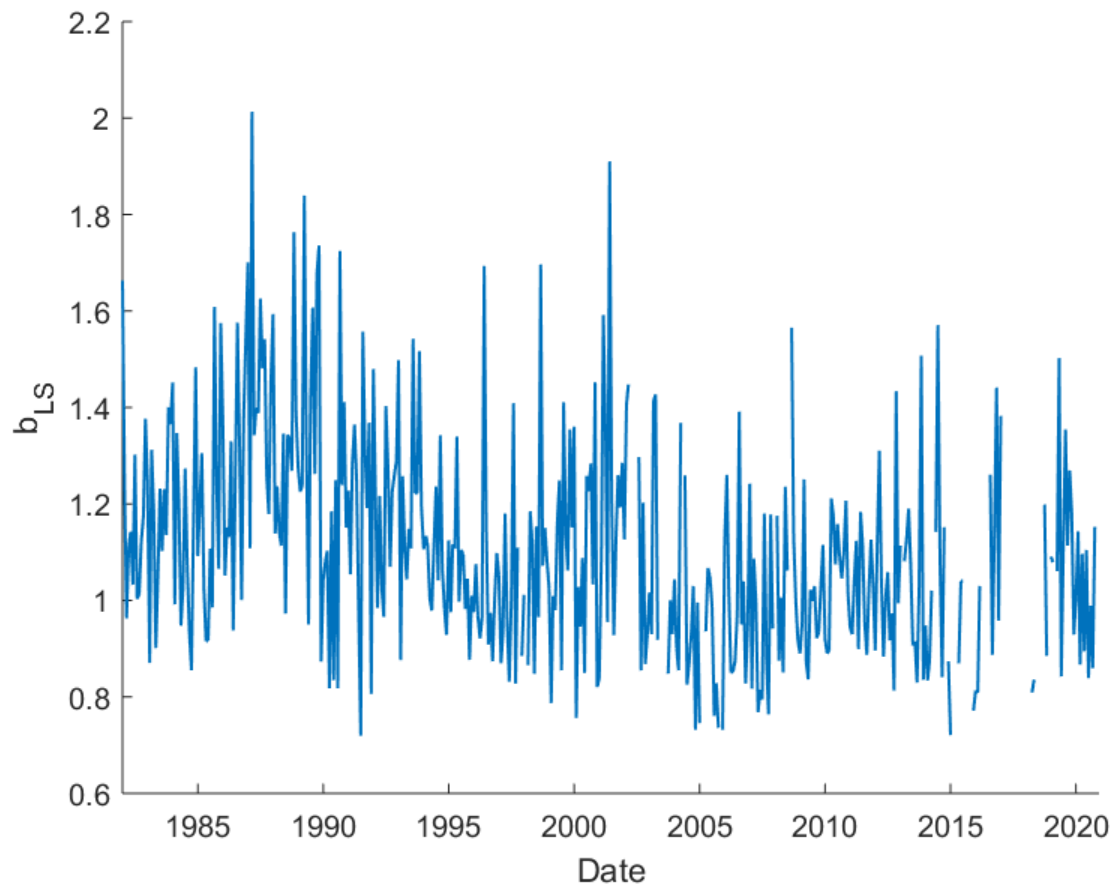
FIGURE 6. Time series of temporal $b_{\mathbf{LS}}$ values. These values were determined for sets of earthquake hypocenters contained in the SCEDC catalogue (without declustering) for each month from 1982 to 2020.
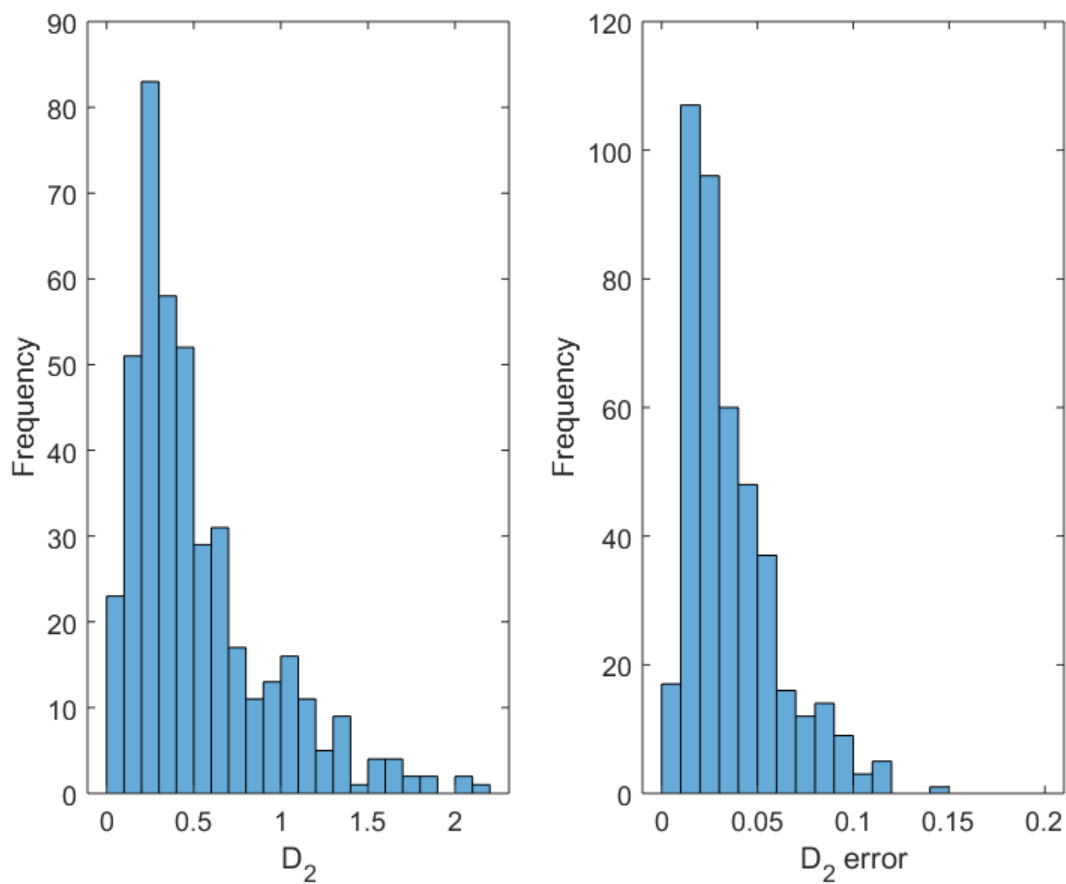
FIGURE 7. Distribution of temporal D_2 and σ_{D_2} values. These values were determined for sets of earthquake hypocenters contained in the SCEDC catalogue (without declustering) for each month from 1982 to 2020. A majority of the temporal σ_{D_2} values were below 0.05.
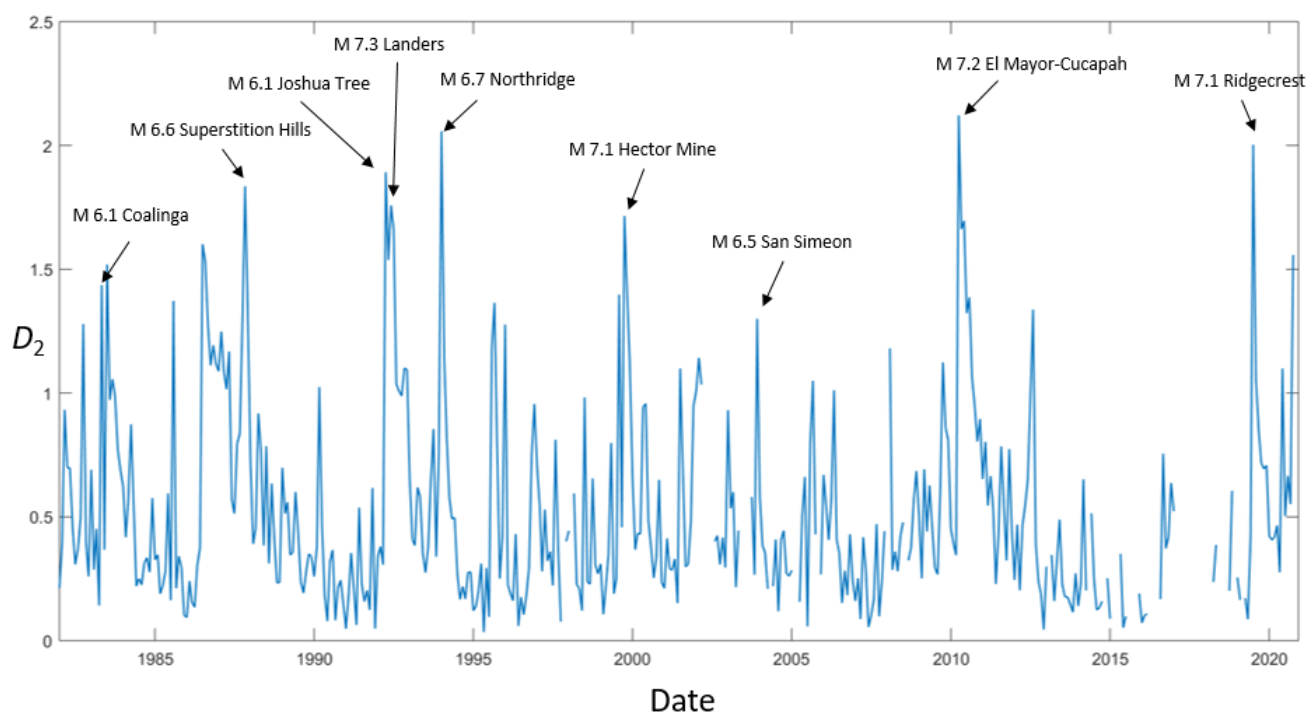
FIGURE 8. Time series of temporal D_2 values. These values were determined for sets of earthquake hypocenters contained in the SCEDC catalogue (without declustering) for each month from 1982 to 2020. D_2 values sharply increased on the months of $M > 6.0$ earthquakes and subsequently decayed.
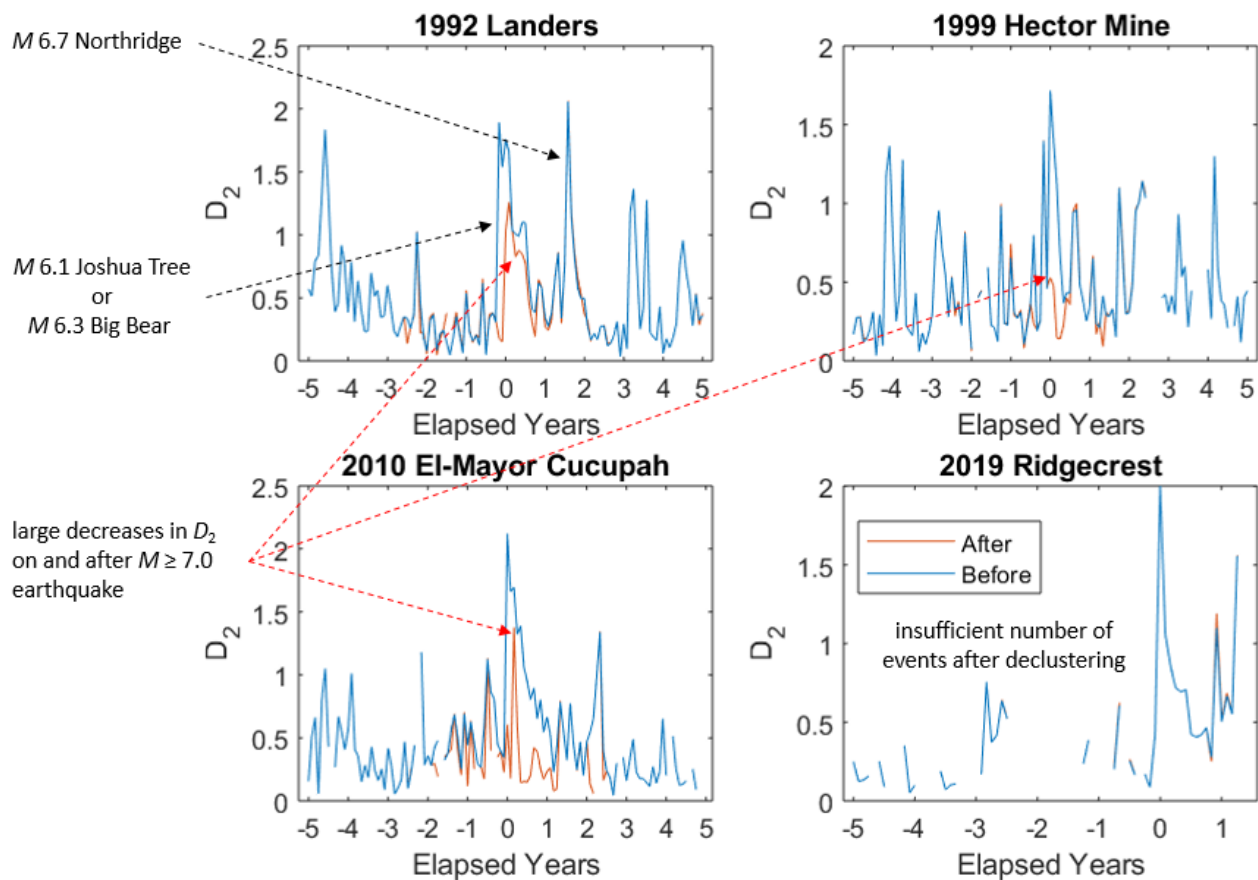
FIGURE 9. Time series of declustered D_2 values for 5-year windows centered about the occurrences of $M > 7.0$ earthquakes. These values were determined for sets of earthquake hypocenters contained in the SCEDC catalogue (with declustering) for each month from 1982 to 2020. After declustering, D_2 values within the temporal window of the aftershock sequences of $M > 7.0$ earthquakes tended to decrease.
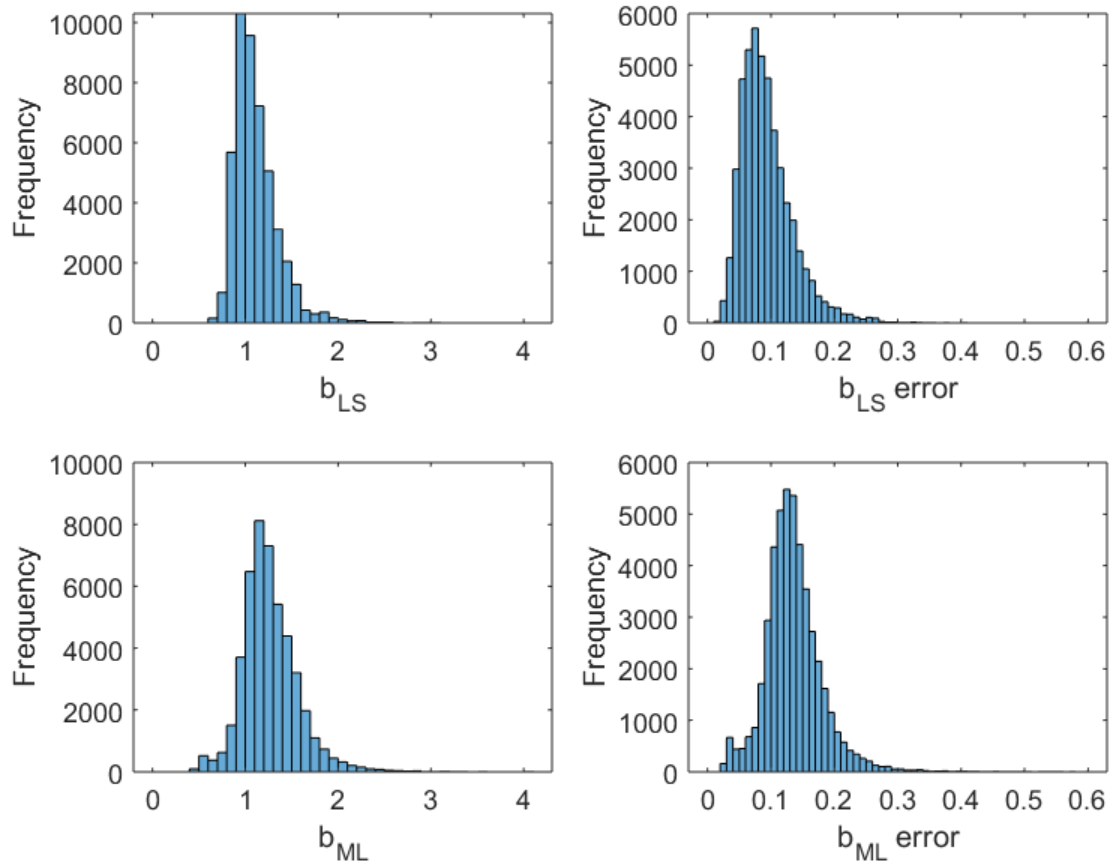
FIGURE 10. Distribution of spatial $b_{\mathbf{LS}}$, $b_{\mathbf{ML}}$, $\sigma_{b_{\mathbf{LS}}}$, and $\sigma_{b_{\mathbf{ML}}}$ values. These values were determined for sets of earthquake hypocenters contained in the SCEDC catalogue (without declustering) for 0.1° latitude by 0.1° longitude cells for each year from 1982 to 2020. Spatial $\sigma_{b_{\mathbf{LS}}}$ values tended to be lower than spatial $\sigma_{b_{\mathbf{ML}}}$ values, with most of the spatial $\sigma_{b_{\mathbf{LS}}}$ values being lower than 0.1, whereas most of the spatial $\sigma_{b_{\mathbf{ML}}}$ values being higher than 0.1.
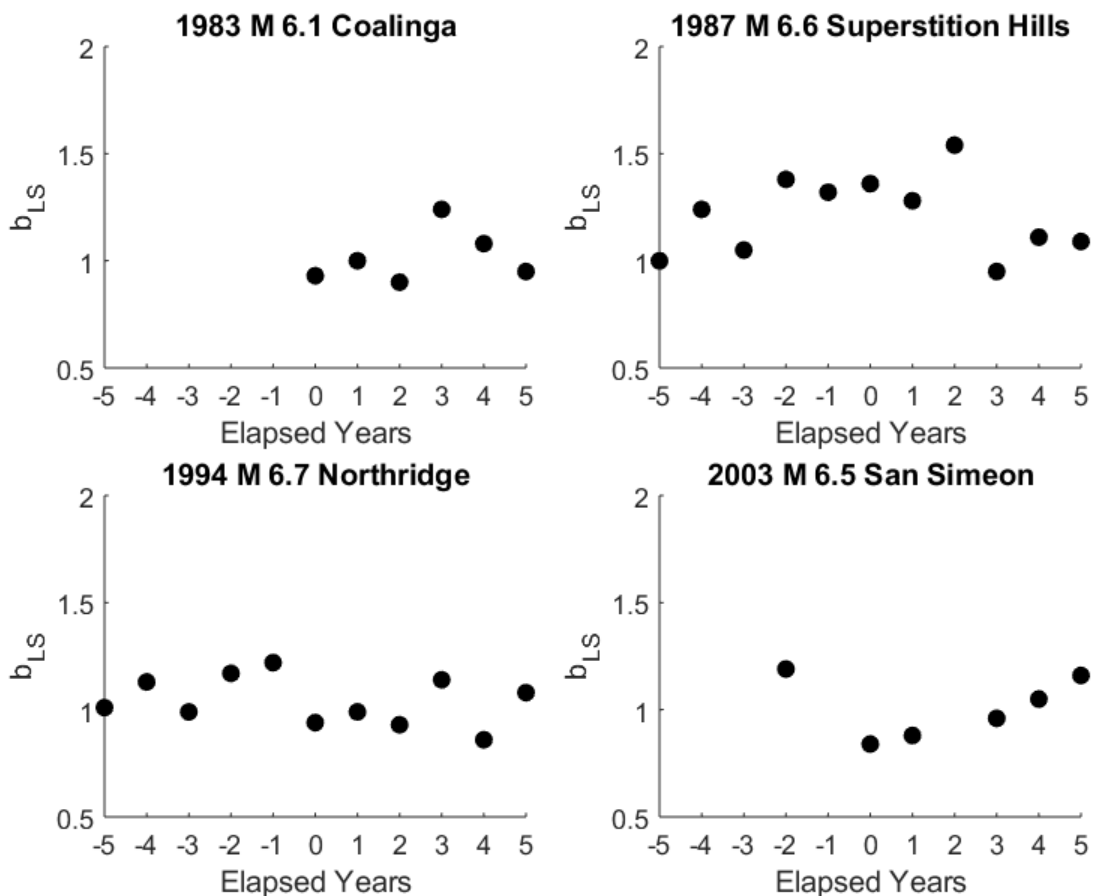
FIGURE 11. Each plot depicts the temporal evolution of mean spatial b_{LS} values in a 77 km radius about the corresponding $M > 6.0$ earthquake. These values were determined for sets of earthquake hypocenters contained in the SCEDC catalogue (without declustering) for $0.1°$ latitude by $0.1°$ longitude cells for each year from 1982 to 2020. Missing values represent years in which all $0.1°$ latitude by $0.1°$ longitude cells within the foreshock-aftershock zone of the epicenter of the corresponding earthquake failed to meet the requirements for determining b_{LS} values. The $b_{\mathbf{LS}}$ values decreased on the years of the $M > 6.0$ earthquakes and increased for at least one year afterwards.

FIGURE 12. Each plot depicts the temporal evolution of mean spatial b_{LS} values in a 77 km radius about the corresponding $M > 7.0$ earthquake. These values were determined for sets of earthquake hypocenters contained in the SCEDC catalogue (without declustering) for $0.1°$ latitude by $0.1°$ longitude cells for each year from 1982 to 2020. Missing values represent years in which all $0.1°$ latitude by $0.1°$ longitude cells within the foreshock-aftershock zone of the epicenter of the corresponding earthquake failed to meet the requirements for determining b_{LS} values. The b_{LS} values decreased on the years of the $M > 7.0$ earthquakes and increased for at least one year afterwards.

FIGURE 13. Distribution of spatial D_2 and σ_{D_2} values. These values were determined for sets of earthquake hypocenters contained in the SCEDC catalogue (without declustering) for 0.1° latitude by 0.1° longitude cells for each year from 1982 to 2020. A majority of the spatial σ_{D_2} values were below 0.05.
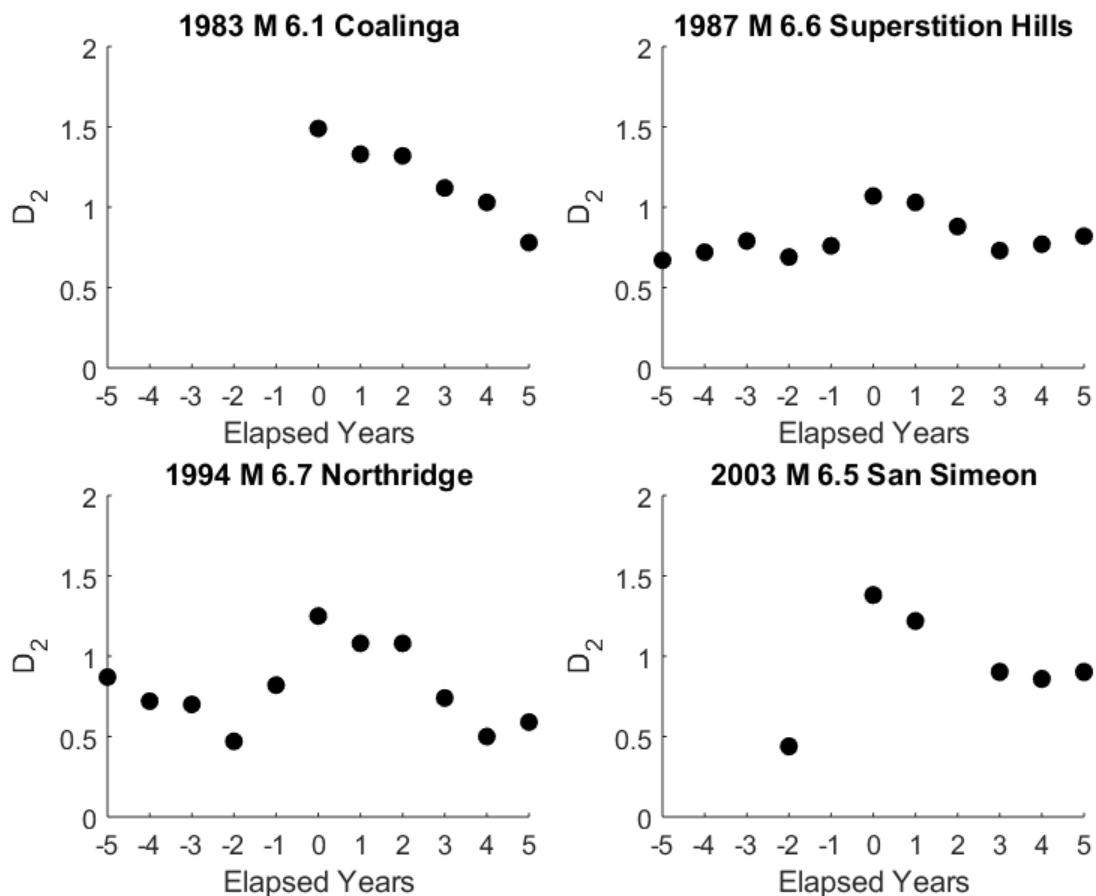
FIGURE 14. Each plot depicts the temporal evolution of mean spatial D_2 values in a 77 km radius about the corresponding $M > 6.0$ earthquake. These values were determined for sets of earthquake hypocenters contained in the SCEDC catalogue (without declustering) for 0.1° latitude by 0.1° longitude cells for each year from 1982 to 2020. Missing values represent years in which all 0.1° latitude by 0.1° longitude cells within the foreshock-aftershock zone of the epicenter of the corresponding earthquake failed to meet the requirements for determining D_2 values. The D_2 values increased on the years of the $M > 6.0$ earthquakes and decreased for at least one year afterwards.

FIGURE 15. Each plot depicts the temporal evolution of mean spatial D_2 values in a 77 km radius about the corresponding $M > 7.0$ earthquake. These values were determined for sets of earthquake hypocenters contained in the SCEDC catalogue (without declustering) for 0.1° latitude by 0.1° longitude cells for each year from 1982 to 2020. Missing values represent years in which all 0.1° latitude by 0.1° longitude cells within the foreshock-aftershock zone of the epicenter of the corresponding earthquake failed to meet the requirements for determining D_2 values. The D_2 values increased on the years of the $M > 7.0$ earthquakes and decreased for at least one year afterwards.

FIGURE 16. Variation in distribution of $\log_{10} C(s)$ against $\log_{10} s$ for spatial D_2 calculations for 2019. Of interest to note is that there are various ranges of length scales in which the set of earthquake hypocenters obey fractal scaling along with the presence of the double S-shaped curve, suggesting either multifractality or a break in fractal scaling.
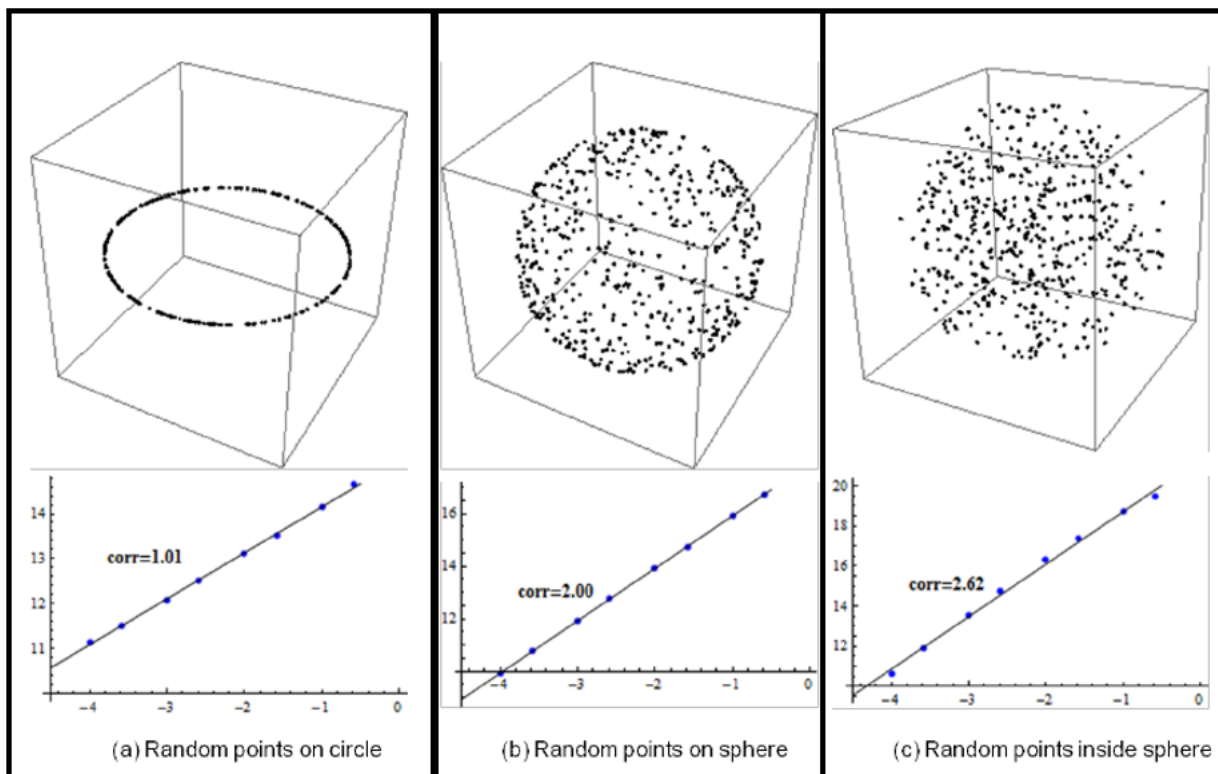
FIGURE 17. Random, finite samplings of a circle, sphere, and ball, along with their corresponding D_2 values (From Wang and Shan, 2009).
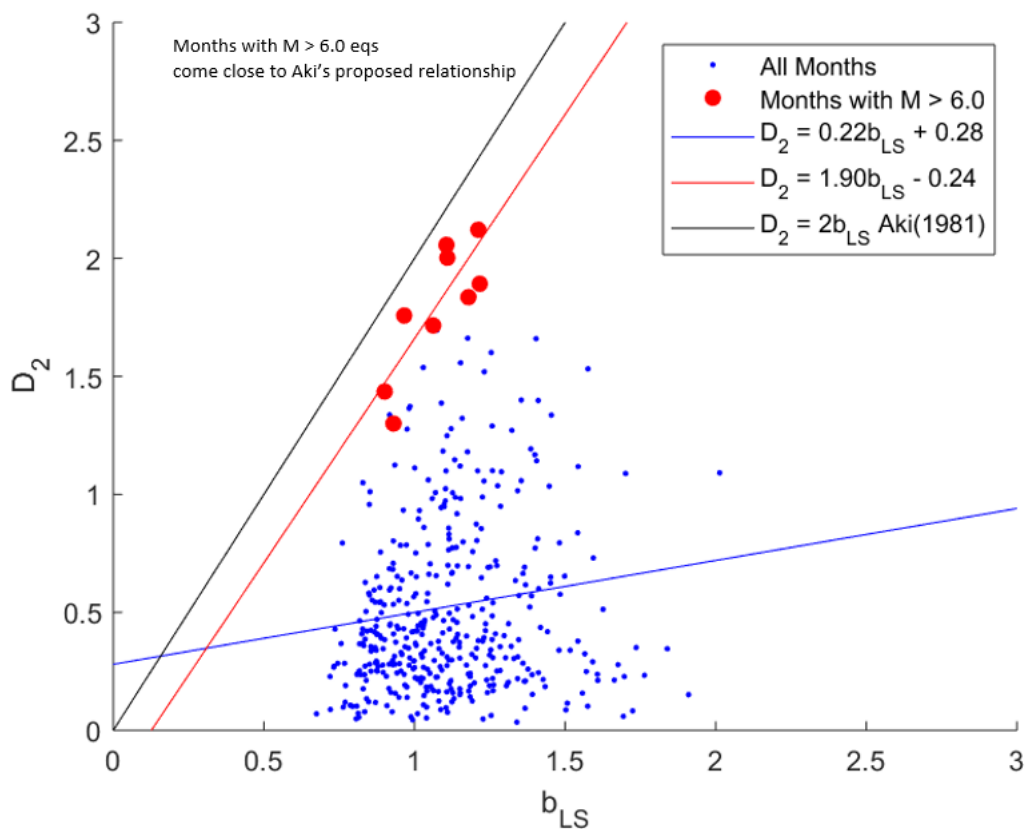
FIGURE 18. Scatter plot of temporal D_2 against temporal $b_{\mathbf{LS}}$. These values were determined for sets of earthquake hypocenters contained in the SCEDC catalogue (without declustering) for each month from 1982 to 2020. Two different populations are shown: one corresponds to all months from 1982 to 2020, whereas the other corresponds to only months in which $M > 6.0$ earthquakes occurred. Color coded lines represent the linear regressions for each population.
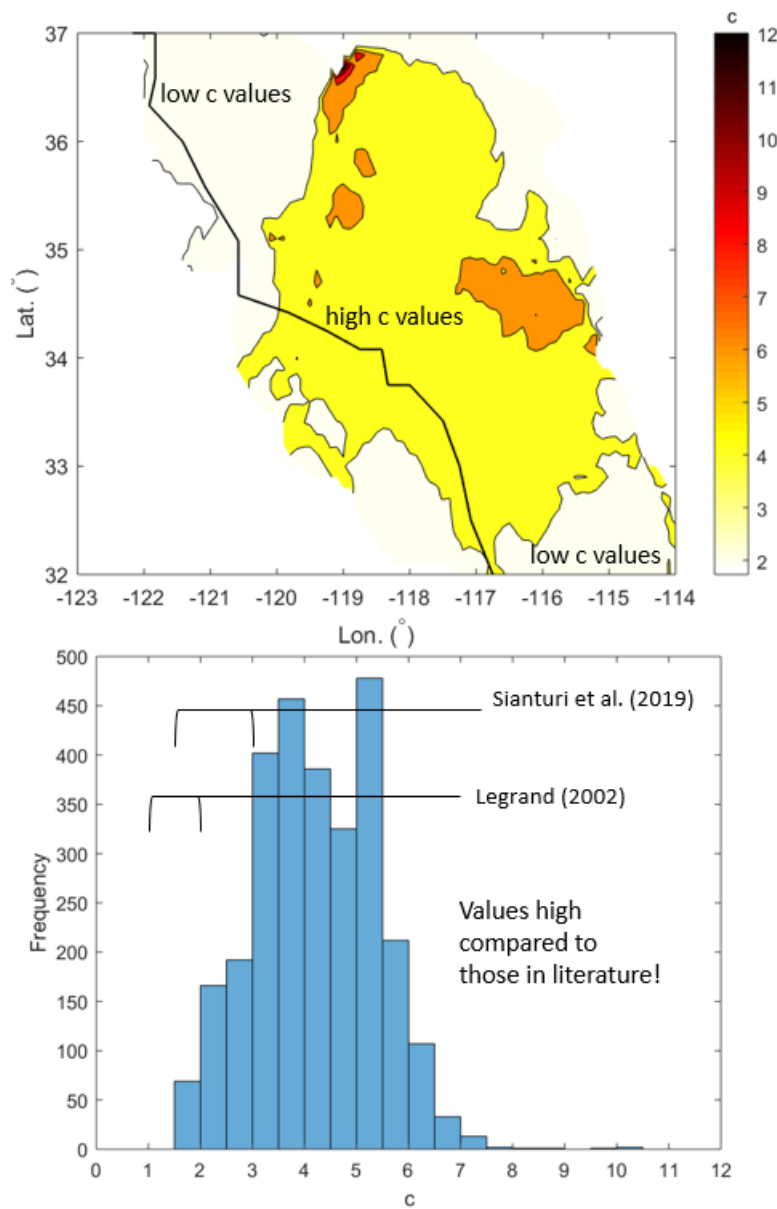
FIGURE 19. Spatial distribution map of spatial c values (top) and associated histogram of spatial c values (bottom). These values were determined for sets of earthquake hypocenters contained in the SCEDC catalogue (without declustering) for 0.1° latitude by 0.1° longitude cells for each year from 1982 to 2020.
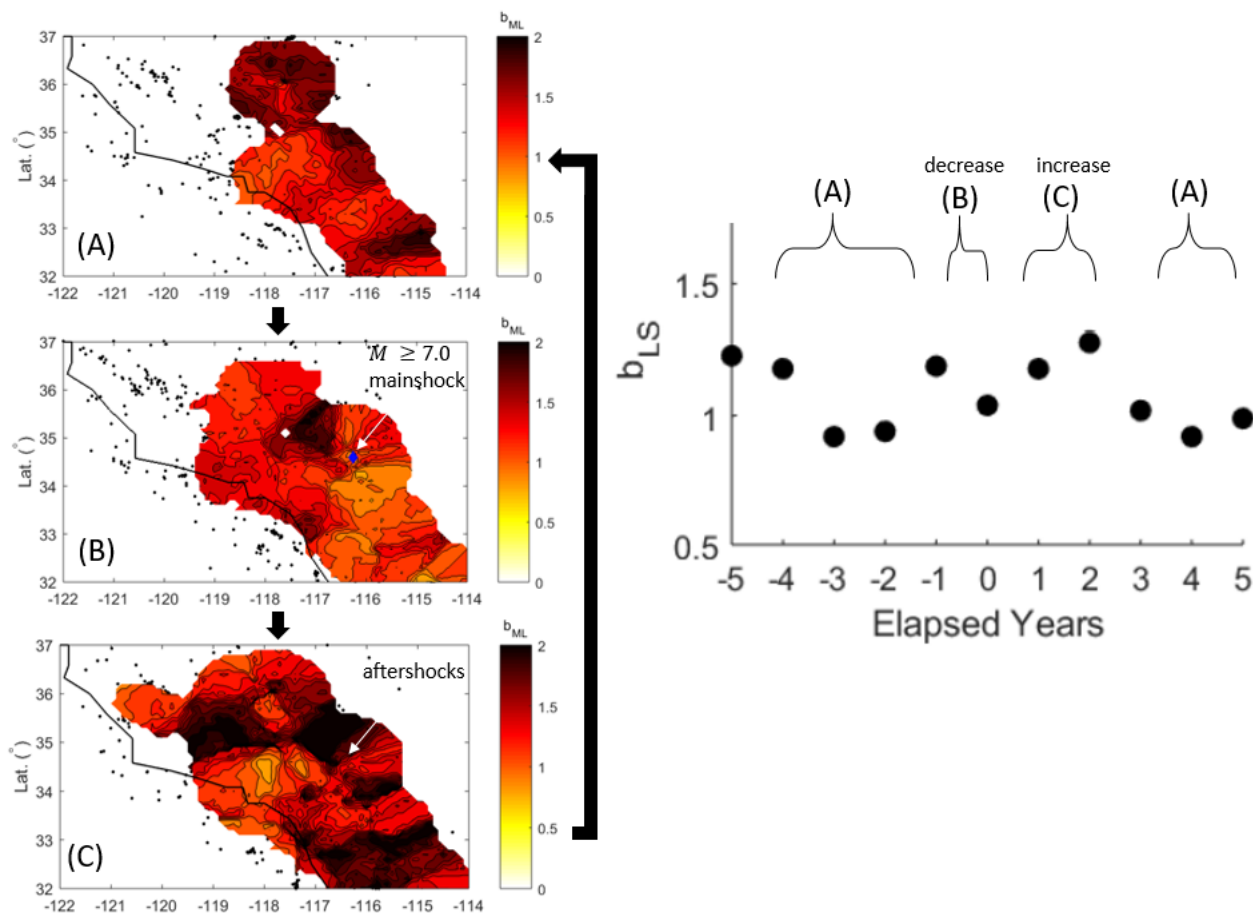
FIGURE 20. Schematic of evolution of spatial b_{LS} values with respect to proximity and timing of a large earthquake, example for the 1999 M 7.1 Hector Mine earthquake. These values were determined for sets of earthquake hypocenters contained in the SCEDC catalogue (without declustering) for 0.1° latitude by 0.1° longitude cells for each year from 1982 to 2020. (A) represents the period prior to a large earthquake, in which b_{LS} values follow no particular pattern. (B) represents the decrease in b_{LS} values from the year prior and the year of the large earthquake near the earthquake's epicenter. (C) represents the increase in b_{LS} values after the large earthquake near the earthquake's epicenter. Finally, the cycle returns to (A) once the b_{LS} values stop increasing.
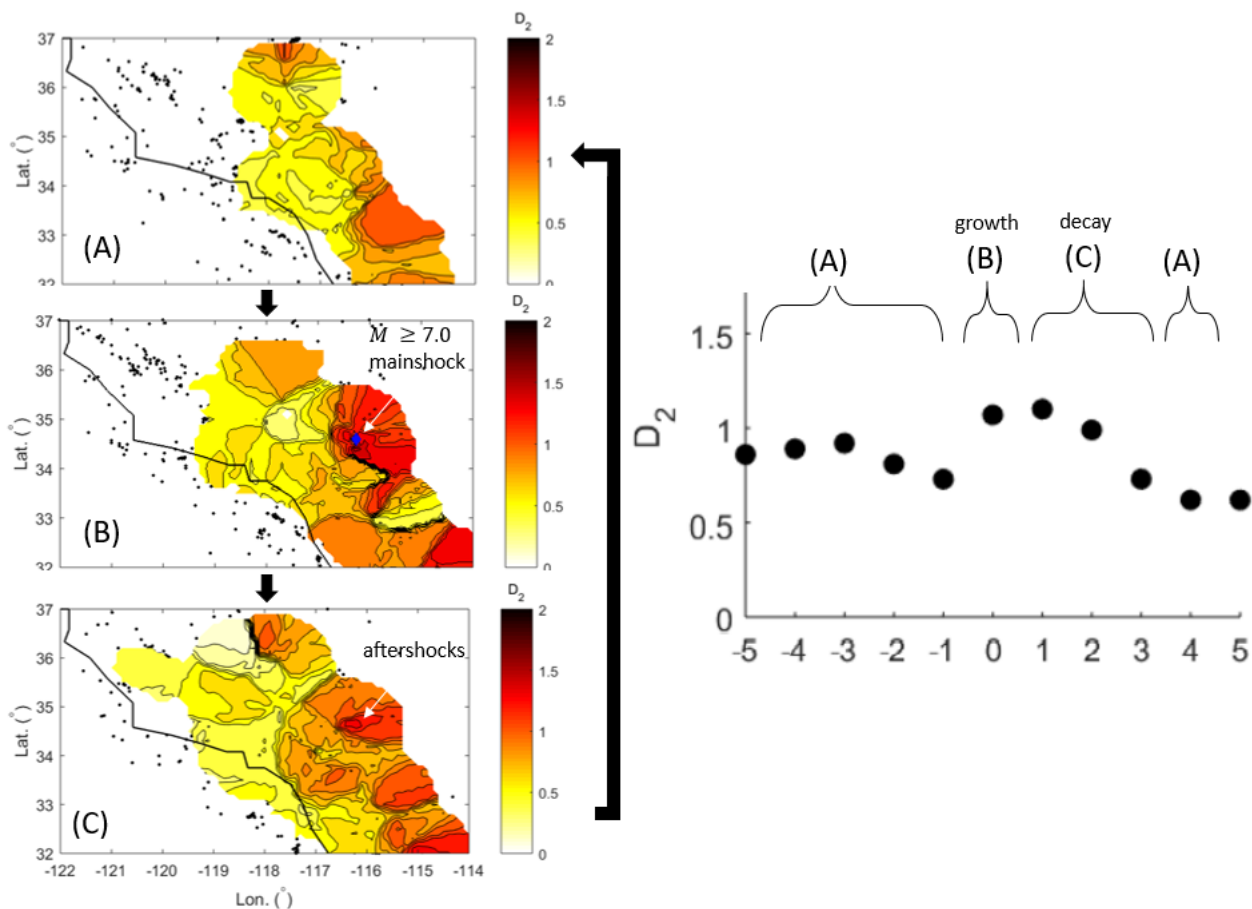
FIGURE 21. Schematic of evolution of spatial D_2 values with respect to proximity and timing of a large earthquake, example for the 1999 M 7.1 Hector Mine earthquake. These values were determined for sets of earthquake hypocenters contained in the SCEDC catalogue (without declustering) for 0.1° latitude by 0.1° longitude cells for each year from 1982 to 2020. A) represents the period prior to a large earthquake, in which D_2 values follow no particular pattern. (B) represents the increase in D_2 values from the year prior and the year of the large earthquake near the earthquake's epicenter. (C) represents the decrease in D_2 values after the large earthquake near the earthquake's epicenter. Finally, the cycle returns to (A) once the D_2 values stop decreasing.

References

[1] Amorèse, D.; Grasso, J.-R.; Rydelek, P.A. 2010. On varying *b*-values with depth: results from computer-intensive tests for Southern California. *Geophysical Journal International*. **180** (1): 347-360.

[2] Aki, K. 1965. Maximum Likelihood Estimate of b in the Formula log N = a - bM and its Confidence Limits. *Bulletin of the Earthquake Research Institute*. **43**: 237-239.

[3] Aki, K. 1966. Estimation of earthquake moment, released energy, and stress-strain drop from the G wave spectrum. *Bulletin of the Earthquake Research Institute*. **44**: 73-88.

[4] Aki, K. 1981. A Probabilistic Synthesis of Precursory Phenomena. *Earthquake Prediction: An International Review*. **4**: 566-574.

[5] Aviles, C.A.; Scholz, C.H.; Boatwright, J. 1987. Fractal Analysis Applied to Characteristic Segments of the San Andreas Fault. *Journal of Geophysical Research*. **92** (B1): 331-344.

[6] Bender, B. 1983. Maximum likelihood estimation of *b* values for magnitude grouped data. *Bulletin of the Seismological Society of America*. **73** (3): 831-851.

[7] Bonnet, E.; Bour, O.; Odling, N.E.; Davy, P.; Main, I.; Cowie, P.; Berkowitz, B. 2001. Scaling of fracture systems in geological media. *Reviews of Geophysics*. **39** (3): 347-383.

[8] Chen, C.-C.; Wang, W.-C.; Chang, Y.-F.; Wu, Y.-M.; Lee, Y.-H. 2006. A correlation between the *b*-value and the fractal dimension from the aftershock sequence of the 1999 Chi-Chi, Taiwan, earthquake. *Geophysical Journal International*. **167**. 1215-1219.

[9] Cicerone, R.D.; Ebel, J.E.; Britton, J. 2009. A systematic compilation of earthquake precursors. *Tectonophysics*. **476**: 371-396.

[10] de Arcangelis, L.; Godano, C.; Grasso, J.R.; Lippiello, E. 2016. Statistical physics approach to earthquake occurrence and forecasting. *Physics Reports*. **628**: 1-91.

[11] Dimitriu, P.P.; Scordilis, E.M.; Karacostas, V.G. 2000. Multifractal Analysis of the Arnea, Greece Seismicity with Potential Implications for Earthquake Prediction. *Natural Hazards*. **21**: 277-295.

[12] Enescu, B.; Ito, K. 2011. Values of b and p: Their variations and relation to physical processes for earthquakes in Japan and Romania. *Romanian Journal of Physics*. **56** (3): 590-608.

[13] Falconer, K. 2014. Fractal Geometry: Mathematical Foundations and Applications.

[14] Featherstone, W.E. 1994. An explanation of the Geocentric Datum of Australia and its effects upon future mapping. *Cartography*. **23** (2): 1-12.

[15] Feng, X.-T.; Seto, M. 1999. Fractal structure of the time distribution of microfracturing in rocks. *Geophysical Journal International.* **136** (1): 275-285.

[16] Fereidoni, A.; Atkinson, G.M. 2014. Aftershock Statistics for Earthquakes in the St. Lawrence Valley. *Seismological Research Letters.* **85** (5): 1125-1136.

[17] Freed, A.M.; Ali, S.T.; Burgmänn, R. 2007. Evolution of stress in Southern California for the past 200 years from coseismic, postseismic and interseismic stress changes. *Geophysical Journal International.* **169** (3): 1164-1179.

[18] Gardner, J.K.; Knopoff, L. 1974. Is the sequence of earthquakes in southern California, with aftershocks removed, Poissonian? *Bulletin of the Seismological Society of America.* **64** (5): 1363-1367.

[19] Gerdan, G.P.; Deakin, R. 1999. Transforming Cartesian coordinates X, Y, Z to Geographical coordinates, ϕ, λ, h. *Australian Surveyor.* **44** (1): 55-63.

[20] Gerstenberger, M.; Wiemer, S.; Giardini, D. 2001. A systematic test of the hypothesis that the b value varies with depth in California. *Geophysical Research Letters.* **28** (1): 57-60.

[21] Godano, C.; Caruso, V. 1995. Multifractal analysis of earthquake catalogues. *Geophysical Journal International.* **121** (2): 385-392.

[22] Grassberger, P. 1983. Generalized dimensions of strange attractors. *Physics Letters A.* **97** (6): 227-230.

[23] Grassberger, P.; Procaccia, I. 1983. Measuring the strangeness of strange attractors. *Physica D: Nonlinear Phenomena.* **9** (1-2): 189-208.

[24] Gulia, L.; Rinaldi, A.P.; Tormann, T.; Vannucci, G.; Enescu, B.; Wiemer, S. 2018. The Effect of a Mainshock on the Size Distribution of the Aftershocks. *Geophysical Research Letters.* **45** (24): 13277-13287.

[25] Gutenberg, B.; Richter, C.F. 1944. Frequency of earthquakes in California. *Bulletin of the Seismological Society of America.* **34** (4): 185-188.

[26] Guttorp, P. 1987. On least-squares estimation of b values. *Bulletin of the Seismological Society of America.* **77** (6): 2115-2124.

[27] Han, Q.; Carpinteri, A.; Lacidogna, G.; Xu, J. 2015. Fractal analysis and yule statistics for seismic prediction based on 2009 L'Aquila earthquake in Italy. *Arabian Journal of Geosciences.* **8**: 2457 - 2465.

[28] Hauksson, E.; Stock, J.; Hutton, K.; Yang, W.; Vidal-Villegas, J.A.; Kanamori, H. 2010. The 2010 M_w 7.2 El Mayor-Cucapah Earthquake Sequence, Baja California, Mexico and Southernmost California, USA: Active Seismotectonics along the Mexican Pacific Margin. *Pure and Applied Geophysics.* **168**: 1255-1277.

[29] Hirata, T.; Satoh, T.; Ito, K. 1987. Fractal structure of spatial distribution of microfracturing in rock. *Geophysical Journal International.* **90** (2): 369-374.

[30] Hirata, T. 1989. A correlation between the b value and the fractal dimension of earthquakes. *Journal of Geophysical Research: Solid Earth.* **94** (B6): 7507-7514.

[31] Hutton, K; Woessner, J.; Hauksson, E. 2010. Earthquake Monitoring in Southern California for Seventy-Seven Years (19322008). *Bulletin of the Seismological Society of America.* **100** (2): 423-446.

[32] Irwin, W.P. 1990. Geology and plate-tectonic development. *The San Andreas Fault System, California: U.S. Geological Survey Professional Paper 1515*: 61 - 80.

[33] Kagan, Y.Y. 2007. Earthquake spatial distribution: the correlation dimension. *Geophysical Journal International.* **168** (3): 1175-1194.

[34] Kanamori, H.; Anderson, D.L. 1975. Theoretical basis of some empirical relations in seismology. *Bulletin of the Seismological Society of America.* **65** (5): 1073-1095.

[35] Legrand, D. 2002. *Short Notes*: Fractal Dimensions of Small, Intermediate, and Large Earthquakes. *Bulletin of the Seismological Society of America.* **92** (8): 3318-3320.

[36] Mandal, P.; Rastogi, B.K. 2005. Self-organized Fractal Seismicity and b Value of Aftershocks of the 2001 Bhuj Earthquake in Kutch (India). *pure and applied geophysics.* **162**: 53-72.

[37] Mandal, P.; Srinagesh, D.; Suresh, G.; Naresh, B.; Naidu, M.; Singh, D.K.; Swathi, K.; Devi, A.; Vittal, S.; Vengala, P.K.; Raghavan, R.V.; Shekar, M.; Saha, S. 2021. Characterization of earthquake hazard at the Palghar and Pulichintala swarm activity regions (India) through three-dimensional modelling of b-value and fractal (correlation) dimensions. *Natural Hazards.* **108**: 1183-1196.

[38] Mondal, S.K.; Roy, P.N.S.; Catherine, J.K.; Pandey, A.K. 2019. Significance of fractal correlation dimension and seismic b-value variation due to 15th July 2009, New Zealand earthquake of Mw 7.8. *Annals of Geophysics.* **62** (5): https://doi.org/10.4401/ag-8020.

[39] Molchan, G.; Kronrod, T. 2009. The fractal description of seismicity. *Geophysical Journal International.* **179** (3): 1787-1799.

[40] Mori, J.; Abercrombie R.E. 1997. Depth dependence of earthquake frequency-magnitude distributions in California: Implications for rupture initiation. *Journal of Geophysical Research.* **102** (B7): 15081-15090.

[41] Nanjo, K.Z.; Hirata, N.; Obara, K.; Kasahar, K. 2012. Decade-scale decrease in b value prior to the M9-class 2011 Tohoku and 2004 Sumatra quakes. *Geophysical Research Letters.* **39** (L20304): https://doi.org/10.1029/2012GL052997.

[42] Nicholson, C.; Seeber, L.; Williams, P.; Sykes, L.R. 1986. Seismicity and Fault Kinematics Through the Eastern Transverse Ranges, California: Block Rotation, Strike-Slip Faulting and Low-Angle Thrusts. *Journal of Geophysical Research: Solid Earth.* **91** (B5): 4891-4908.

[43] Nordström, E.; Dineva, S.; Nordlund, E. 2017. Source parameters of seismic events potentially associated with damage in block 33/34 of the Kiirunavaara mine (Sweden). *Acta Geophysica.* **65**: 1229-1242.

[44] Okubo, P.G.; Aki, K. 1987. Fractal Geometry in the San Andreas Fault System. *Journal of Geophysical Research: Solid Earth.* **92** (B1): 345-355.

[45] Ogata, Y.; Yamashina, K. 1986. Unbiased estimate for b-value of magnitude frequency. *Journal of Physics of the Earth.* **34**: 187-194.

[46] Öncel, A.O.; Main, I.; Alptekin, Ö.; Cowie, P. 1996. Spatial variations of the fractal properties of seismicity in the Anatolian fault zones. *Tectonophysics.* **257** (2-4): 189-202.

[47] Oncel, A.O.; Wilson, T.H. 2002. Space-Time Correlations of Seismotectonic Parameters: Examples from Japan and from Turkey Preceding the İzmit Earthquake. *Bulletin of the Seismological Society of America.* **92** (1): 339-349.

[48] Öncel, A.O.; Wilson, T. 2004. Correlation of seismotectonic variables and GPS strain measurements in western Turkey. *Journal of Geophysical Research: Solid Earth.* **109** (B11): https://doi.org/10.1029/2004JB003101.

[49] Öztürk, S. 2012. Statistical correlation between b-value and fractal dimension regarding Turkish epicentre distribution. *Earch Sciences Research Journal.* **16** (2): 103-108.

[50] Page, R. 1968. Aftershocks and microaftershocks of the great Alaska earthquake of 1964. *Bulletin of the Seismological Society of America.* **58** (3): 1131-1168.

[51] Perrin, C.; Manighetti, I.; Gaudemer, Y. 2016. Off-fault tip splay networks: A genetic and generic property of faults indicative of their long-term propagation. *Comptes Rendus Geoscience.* **348** (1): 52-60.

[52] Radziminovich, N.A.; Miroshnichenko, A.I.; Zuev, F.L. 2019. Magnitude of completeness, b-value, and spatial correlation dimension of earthquakes in the South Baikal Basin, Baikal Rift System. *Tectonophysics*. **759**: 44-57.

[53] Reasenberg, P. 1985. Second-Order Moment of Central California Seismicity, 1969-1982. *Journal of Geophysical Research: Solid Earth*. **90** (B7): 5479-5495.

[54] Roch, J.; Duperray, P.; Schindelé, F. 2016. Very Fast Characterization of Focal Mechanism Parameters Through W-Phase Centroid Inversion in the Context of Tsunami Warning. *pure and applied geophysics*. **173**: 3881-3893.

[55] Roy, P.N.S.; Nath, S.K. 2007. Precursory correlation dimensions for three great earthquakes. *Current Science*. **93** (11): 1522-1529.

[56] Roy, S.; Ghosh, U.; Hazra, S.; Kayal, J.R. 2011. Fractal dimension and *b*-value mapping in the Andaman-Sumatra subduction zone. *Natural Hazards*. **57**: 27-37.

[57] Sandri, L.; Marzocchi, W. 2007. A technical note on the bias in the estimation of the *b*-value and its uncertainty through the Least Squares technique. *Annals of Geophysics*. **50** (3): 329-339.

[58] Scholz, C.H. 2015. On the stress dependence of the earthquake *b* value. *Geophysical Research Letters*. **42** (5): 1399-1402.

[59] Shi, Y.; Bolt, B.A. 1982. The standard error of the magnitude-frequency *b* value. *Bulletin of the Seismological Society of America*. **72** (5): 1677-1687.

[60] Sianturi, H.L.; Susilo, A.; Sunaryo; Maryanto, S. 2019. Correlation Analysis of Spatial Distribution, Temporal Seismotectonics, and Return Period of Earthquake in East Nusa Tenggara, Indonesia. *International Journal of Geophysics*. https://doi.org/10.1155/2019/5485783.

[61] Smith, W.D. 1981. The *b*-value as an earthquake precursor. *Nature*. **289**: 136-139.

[62] Smith, W.D. 1986. Evidence for precursory changes in the frequency-magnitude *b*-value. *Geophysical Journal International*. **86** (3): 815-838.

[63] Telesca, L.; Cuomo, V.; Lapenna, V.; Macchiato, M. 2001. Identifying space-time clustering properties of the 1983-1997 Irpinia-Basilicata (Southern Italy) seismicity. *Tectonophysics*. **330** (1-2): 93-102.

[64] Tiwari, A.; Paul, A.; Singh, R.; Upadhyay, R. 2021. Potential seismogenic asperities in the Garhwal-Kumaun region, NW Himalaya: seismotectonic implications. *Natural Hazards*. **107**: 73-95.

[65] Tosi, P. 1998. Seismogenic structure behavior revealed by spatial clustering of seismicity in the Umbria-Marche Region (Central Italy). *Annals of Geophysics*. **41** (2): 215-224.

[66] Tosi, P.; Rubeis, V.D.; Loreto, V.; Pietronero, L. 2008. Space-time correlation of earthquakes. *Geophysical Journal International.* **173** (3): 932-941.

[67] Turcotte, D.L. 1997. *Fractals and Chaos in Geology and Geophysics.*

[68] Utsu, T. 1961. A Statistical Study on the Occurrence of Aftershocks. *The Geophysical Magazine.* **30**: 521-605.

[69] Utsu, T. 1965. A method for determining the value of b in the formula $\log n = a - bM$ showing the magnitude-frequency relation for earthquakes. *Geophysical Bulletin of Hokkaido University.* **13**: 99-103.

[70] van Stiphout, T.; J. Zhuang; D. Marsan. 2012. Seismicity declustering, Community Online Resource for Statistical Seismicity Analysis. doi:10.5078/corssa52382934. Available at http://www.corssa.org.

[71] Wang, J.; Shan, J. 2009. Segmentation of LiDAR point clouds for building extraction. *The American Society of Photogrammetry and Remote Sensing 2009 Annual Conference.*

[72] Wang, J.P.; Wu, Y.-M.; Huang, D.; Chang, S.-C. 2014. A new procedure to best-fit earthquake magnitude probability distributions: including an example for Taiwan. *Natural Hazards.* **71**. 837-850.

[73] Wiemer, S.; Wyss, M. 1997. Mapping the frequency-magnitude distribution in asperities: An improved technique to calculate recurrence times? *Journal of Geophysical Research: Solid Earth.* **102** (B7): 15115-15128.

[74] Wiemer, S.; Wyss, M. 2000. Minimum Magnitude of Completeness in Earthquake Catalogs: Examples from Alaska, the Western United States, and Japan. *Bulletin of the Seismological Society of America.* **90** (4): 859-869.

[75] Wyss, M.; Sammis, C.G.; Nadeau, R.M.; Wiemer, S. 2004. Fractal Dimension and b-Value on Creeping and Locked Patches of the San Andreas Fault near Parkfield, California. *Bulletin of the Seismological Society of America.* **94** (2): 410-421.

[76] Ye, J.; Liu, M. 2017. How fault evolution changes strain partitioning and fault slip rates in Southern California: Results from geodynamic modeling. *Journal of Geophysical Research: Solid Earth.* **122** (8): 6893-6909.

[77] Zhuang, J.; Ogata, Y.; Vere-Jones, D. 2004. Analyzing earthquake clustering features by using stochastic reconstruction. *Journal of Geophysical Research.* **109** (B5): https://doi.org/10.1029/2003JB002879.

Appendix

Each figure in the appendix contains a set of four spatial distribution maps for each year from 1982 to 2020. For each figure, the map in the top left shows the spatial distribution of $b_{\mathbf{LS}}$ values, the map in the top right shows the spatial distribution of $b_{\mathbf{ML}}$ values, the map in the bottom left shows the spatial distribution of D_2 values, and the map in the bottom right shows the spatial distribution of earthquake epicenters. These values were determined for sets of earthquake hypocenters contained in the SCEDC catalogue (without declustering) for 0.1° latitude by 0.1° longitude cells for each year from 1982 to 2020.
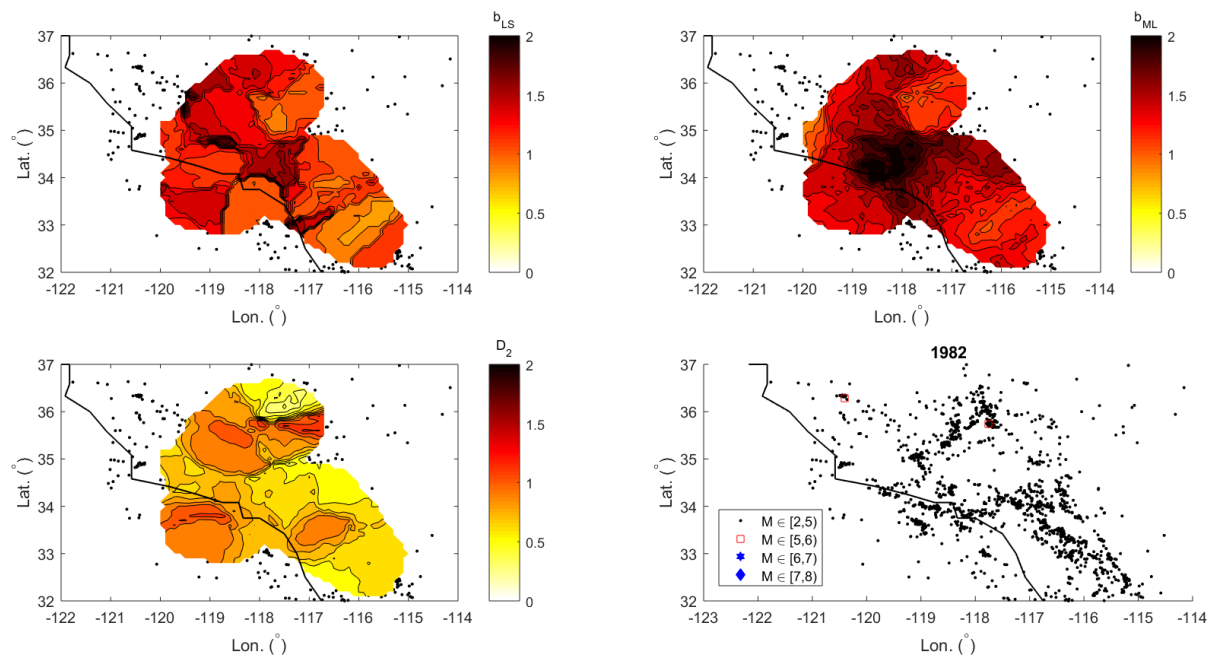
FIGURE A.1. Sets of spatial distribution maps for 1982.
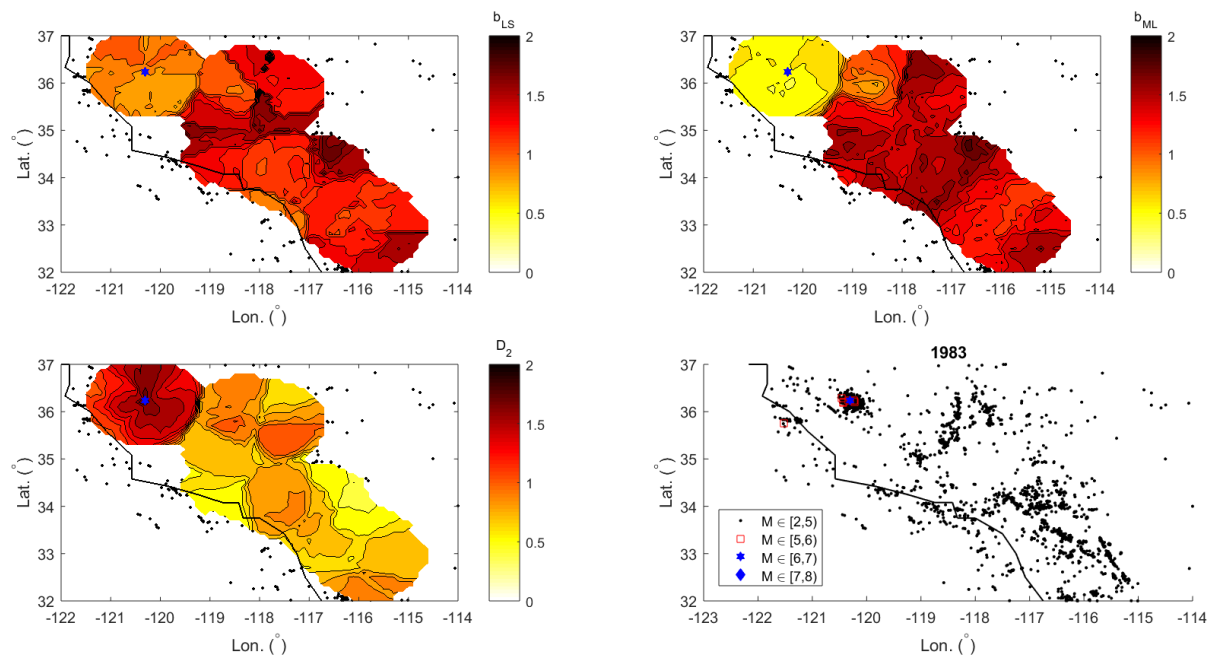
FIGURE A.2. Sets of spatial distribution maps for 1983.
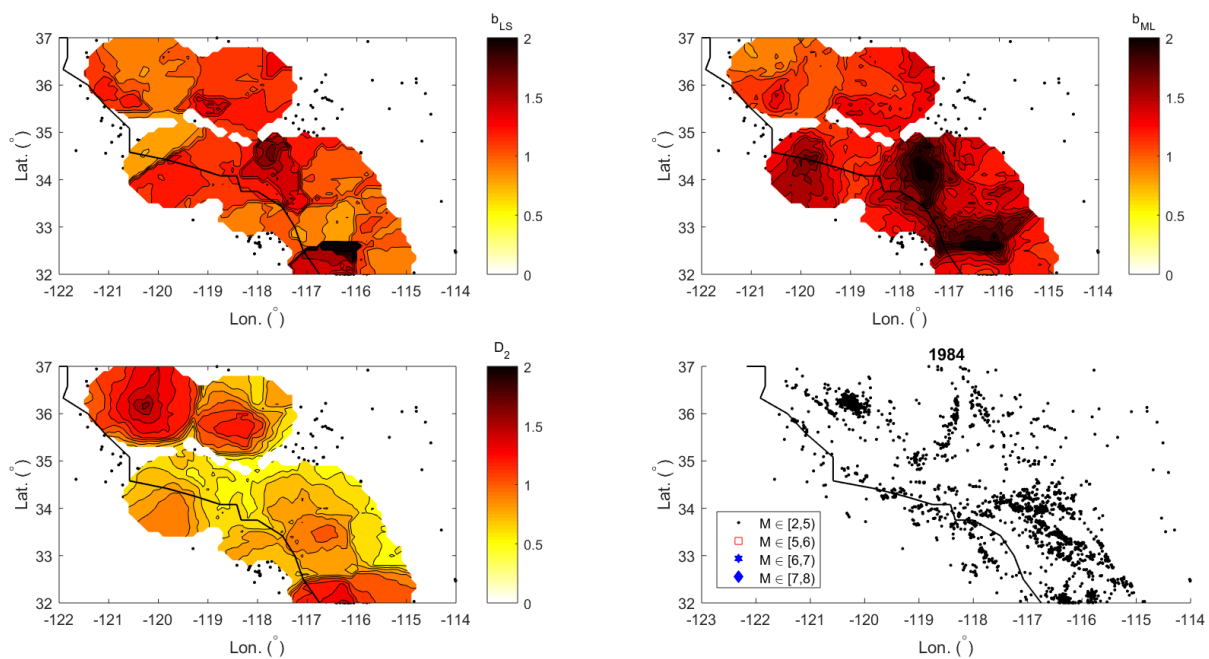
FIGURE A.3. Sets of spatial distribution maps for 1984.
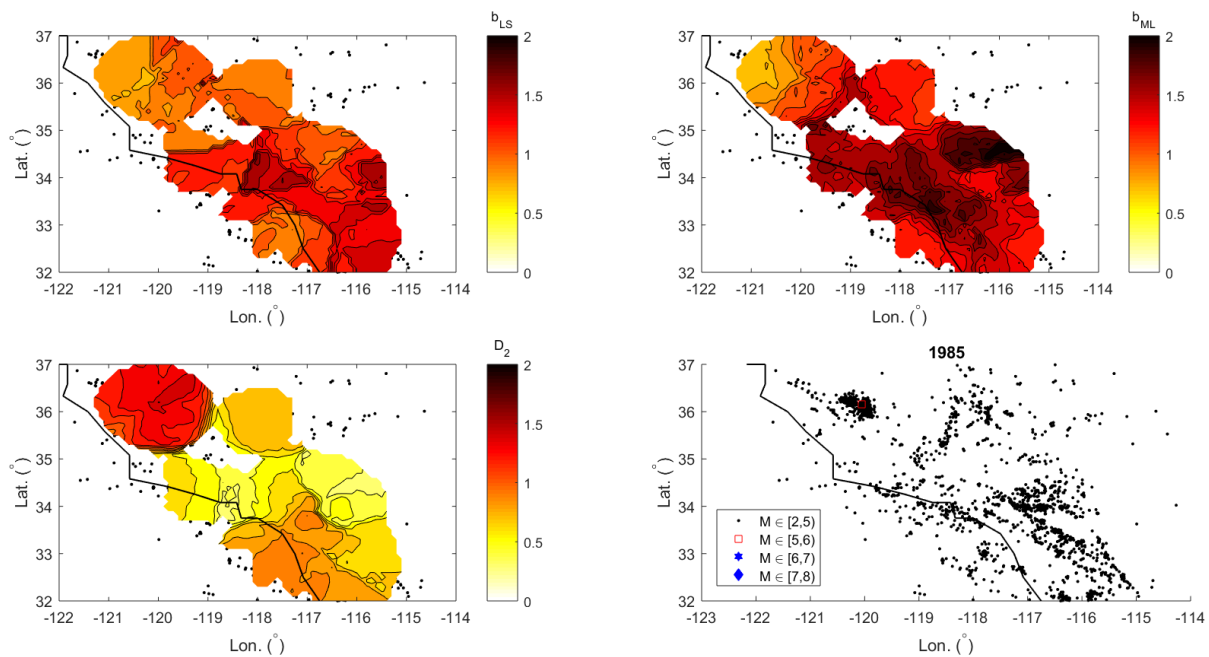
FIGURE A.4. Sets of spatial distribution maps for 1985.
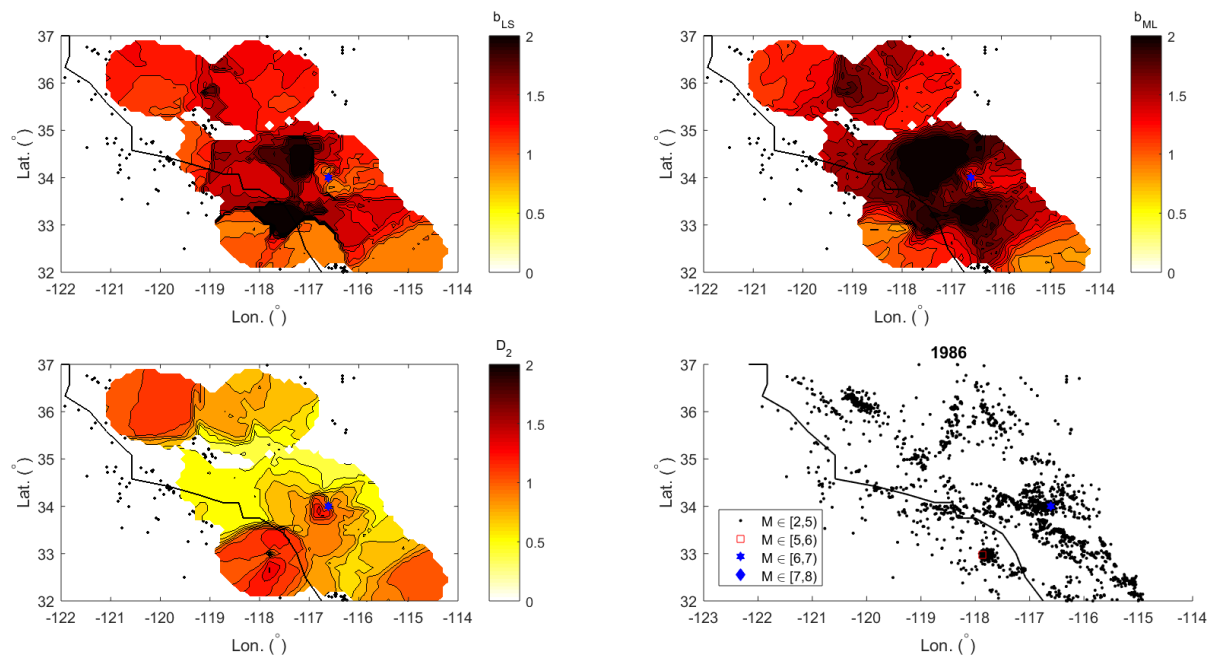
FIGURE A.5. Sets of spatial distribution maps for 1986.
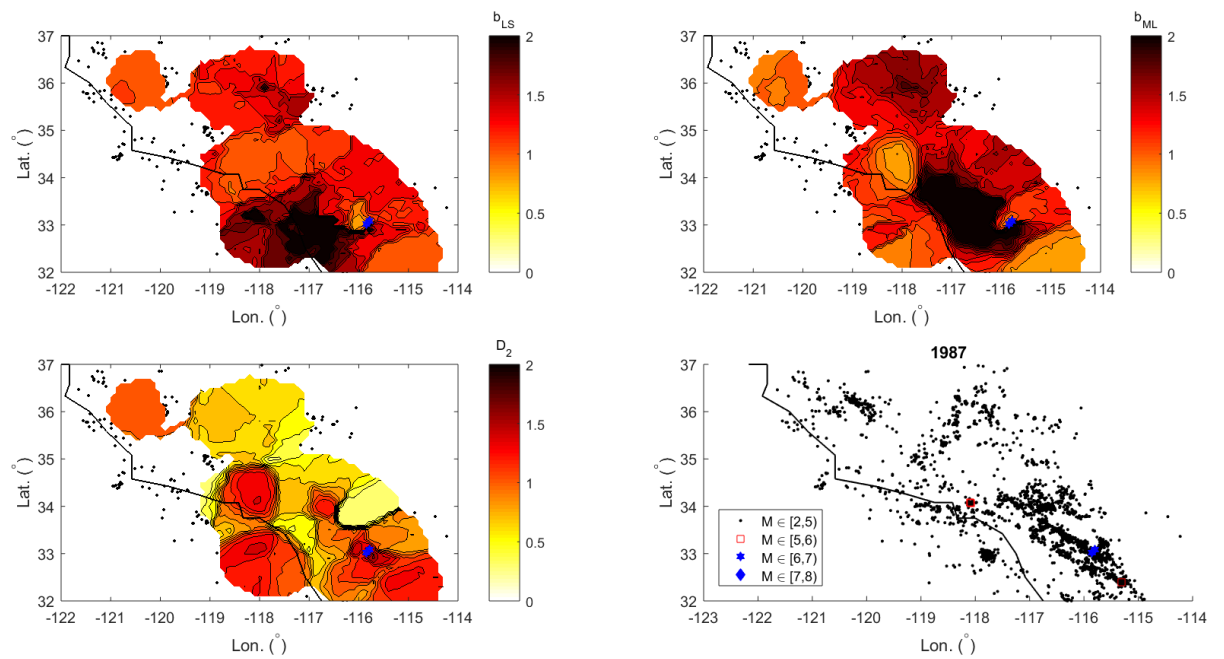
FIGURE A.6. Sets of spatial distribution maps for 1987.
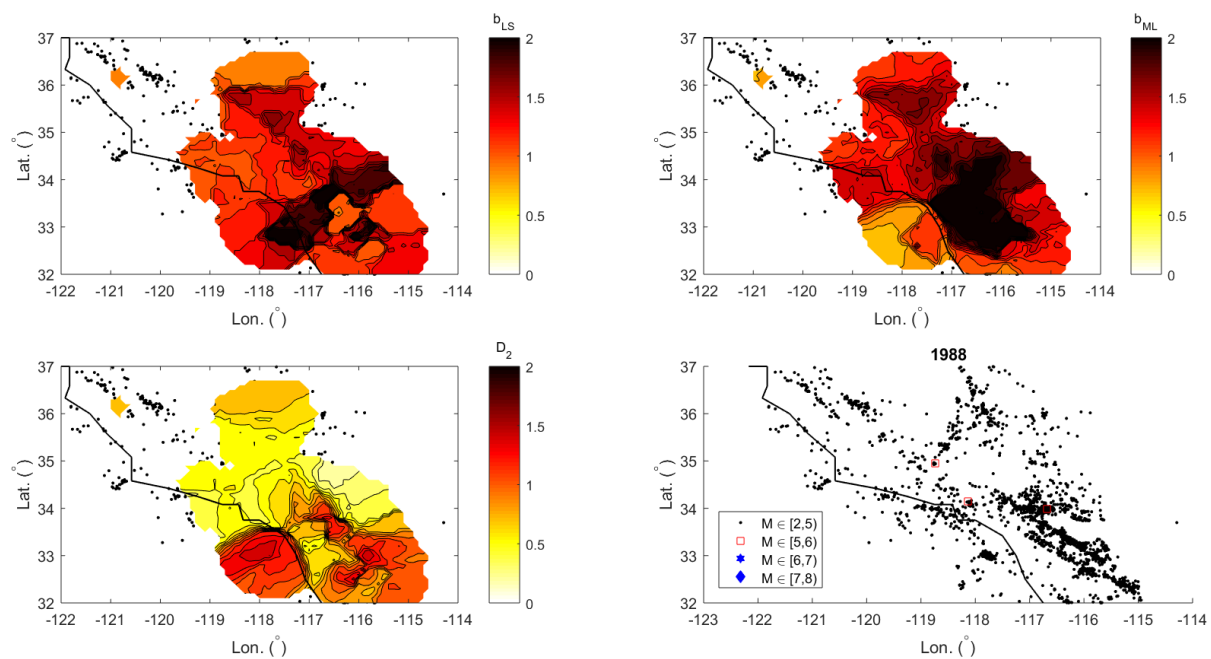
FIGURE A.7. Sets of spatial distribution maps for 1988.
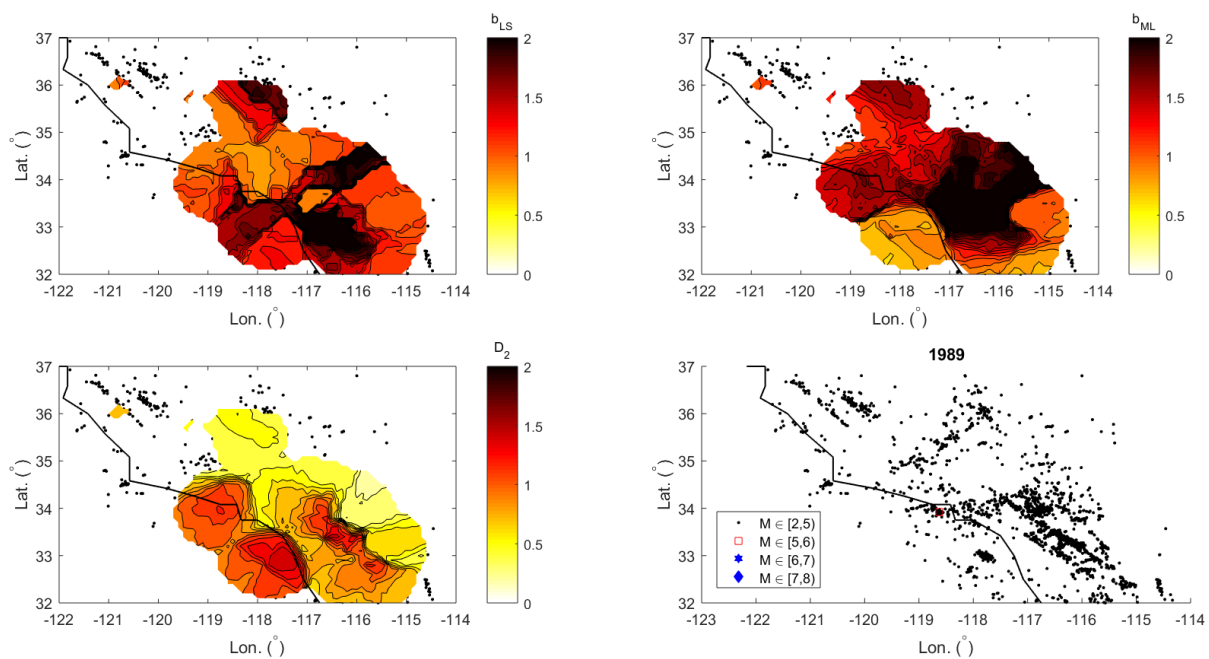
FIGURE A.8. Sets of spatial distribution maps for 1989.
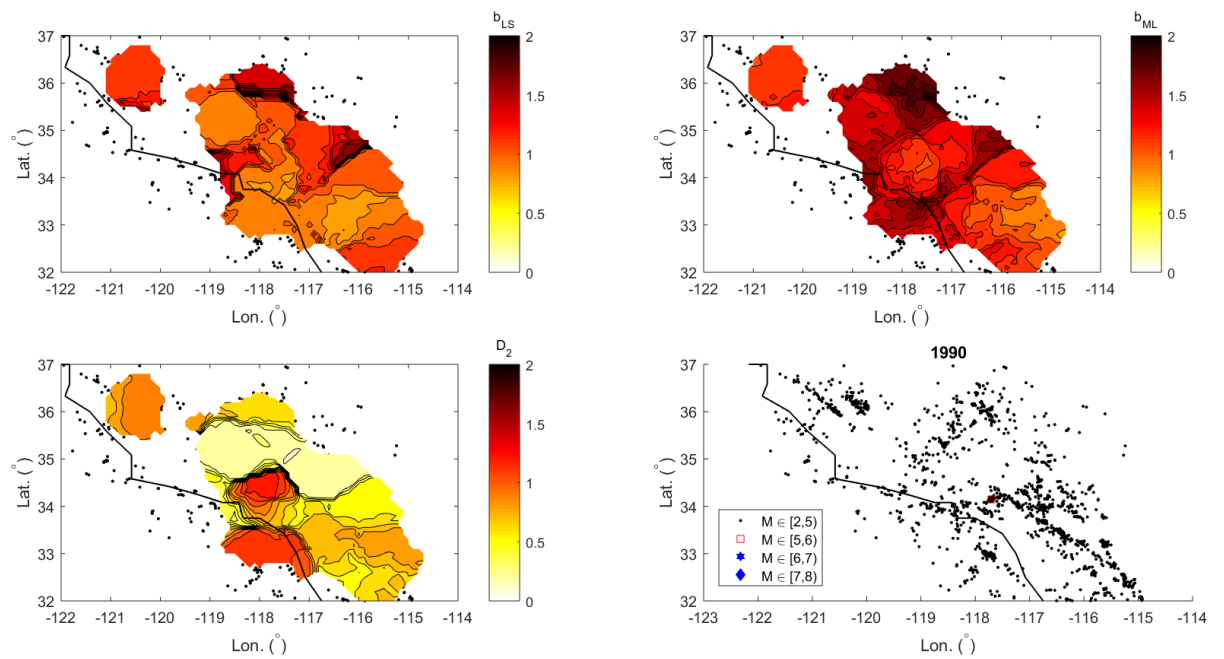
FIGURE A.9. Sets of spatial distribution maps for 1990.
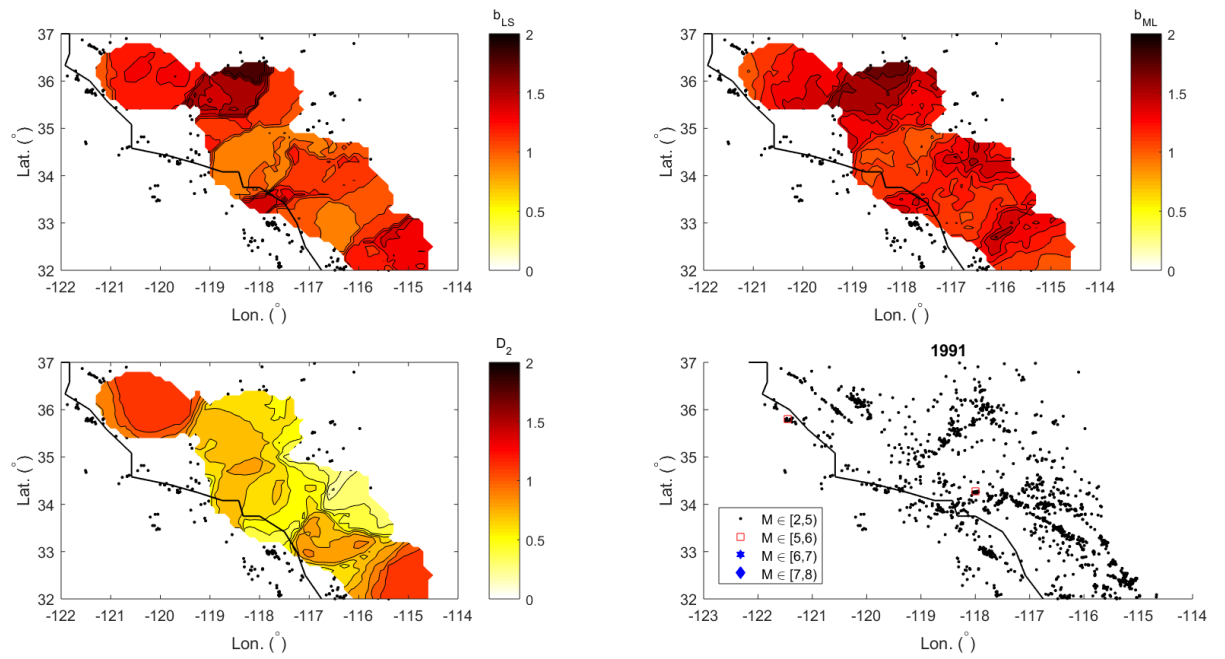
FIGURE A.10. Sets of spatial distribution maps for 1991.
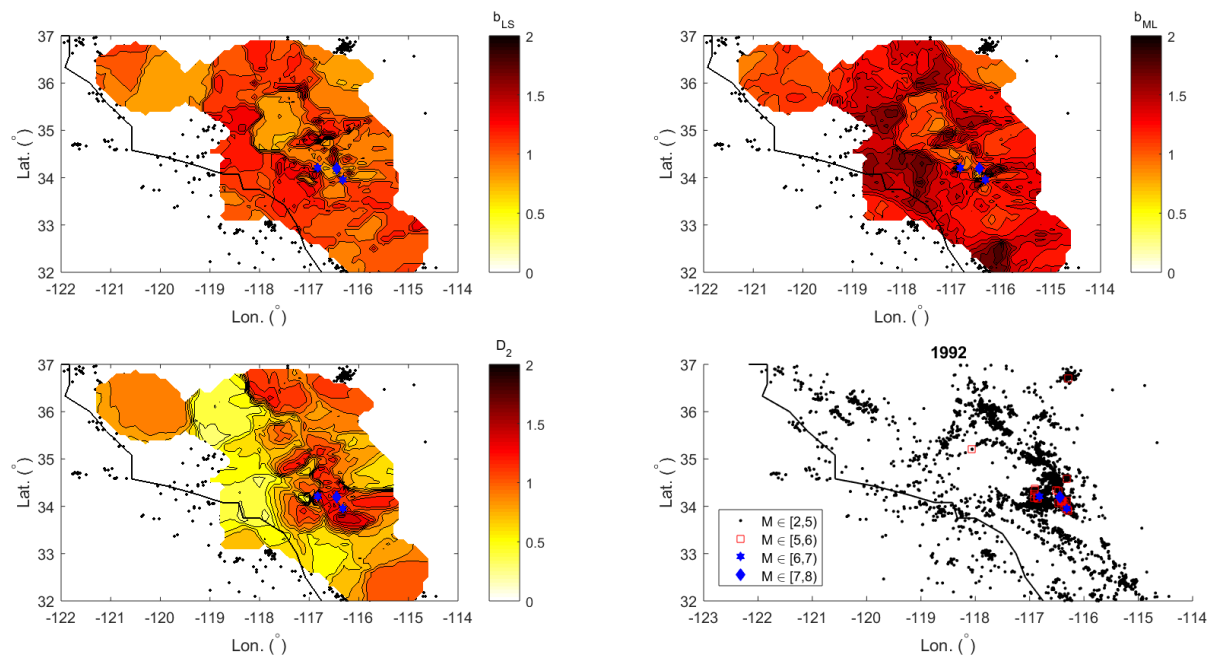
FIGURE A.11. Sets of spatial distribution maps for 1992.
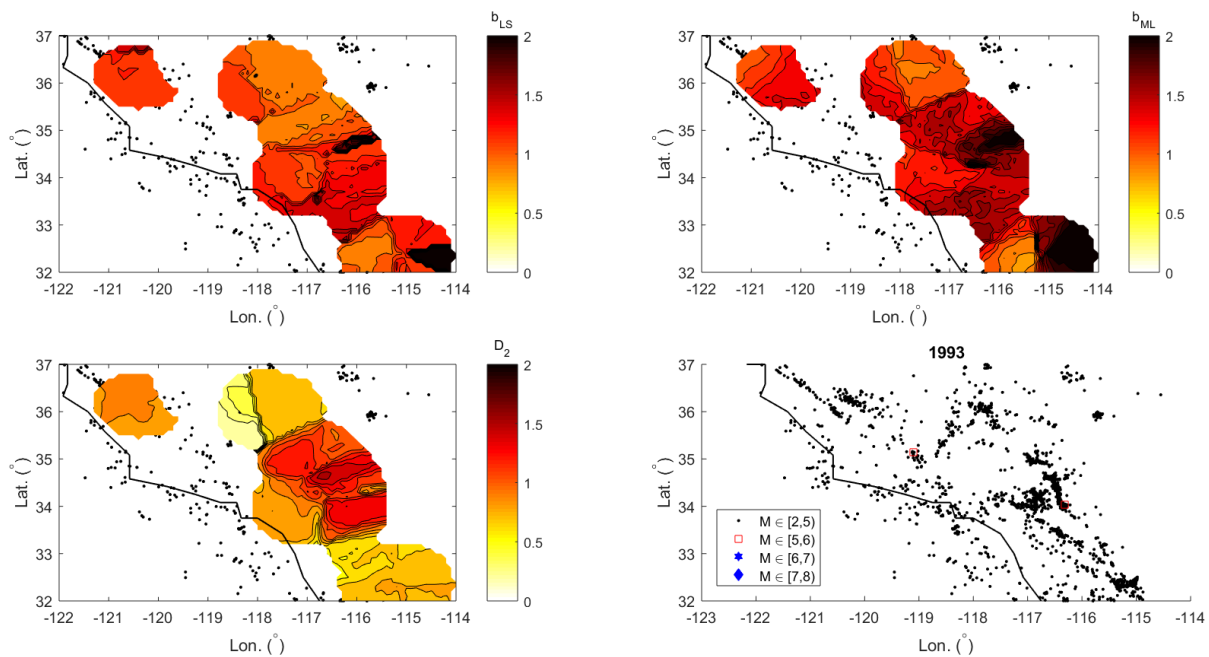
FIGURE A.12. Sets of spatial distribution maps for 1993.
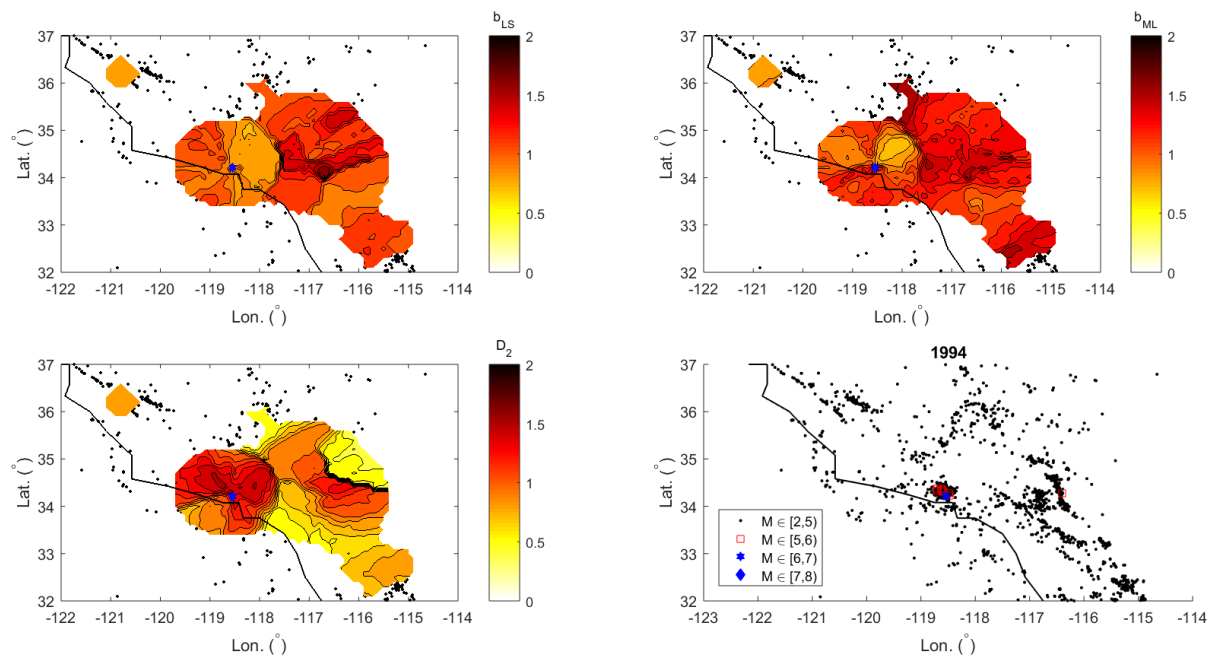
FIGURE A.13. Sets of spatial distribution maps for 1994.
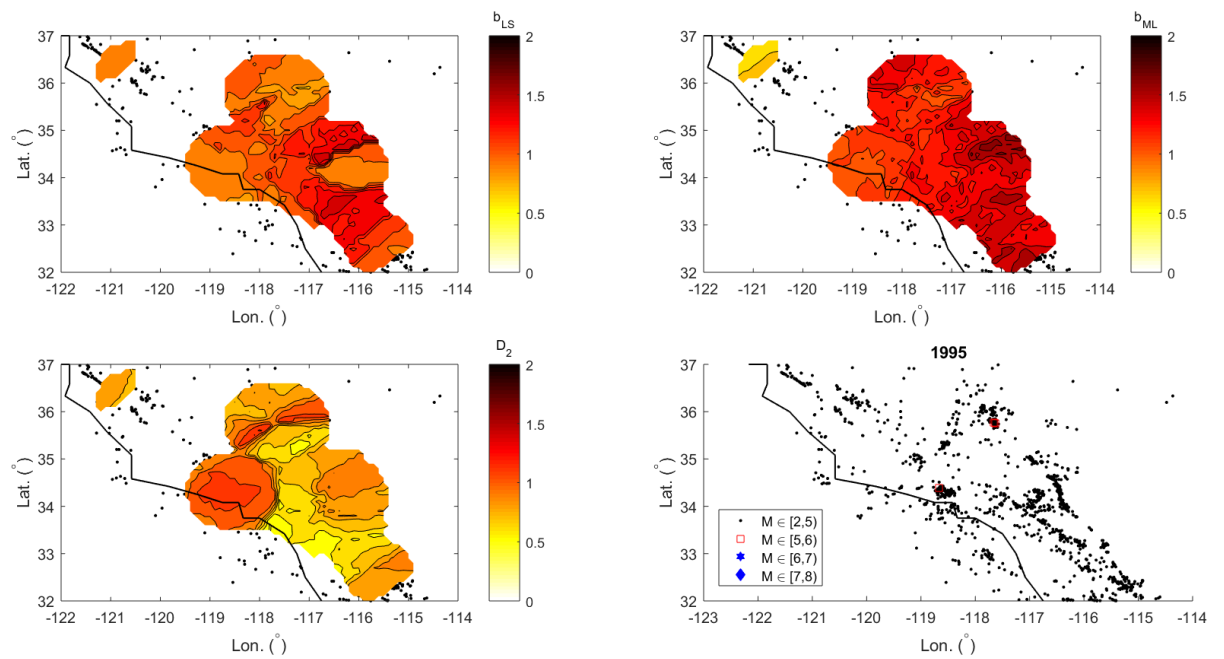
FIGURE A.14. Sets of spatial distribution maps for 1995.
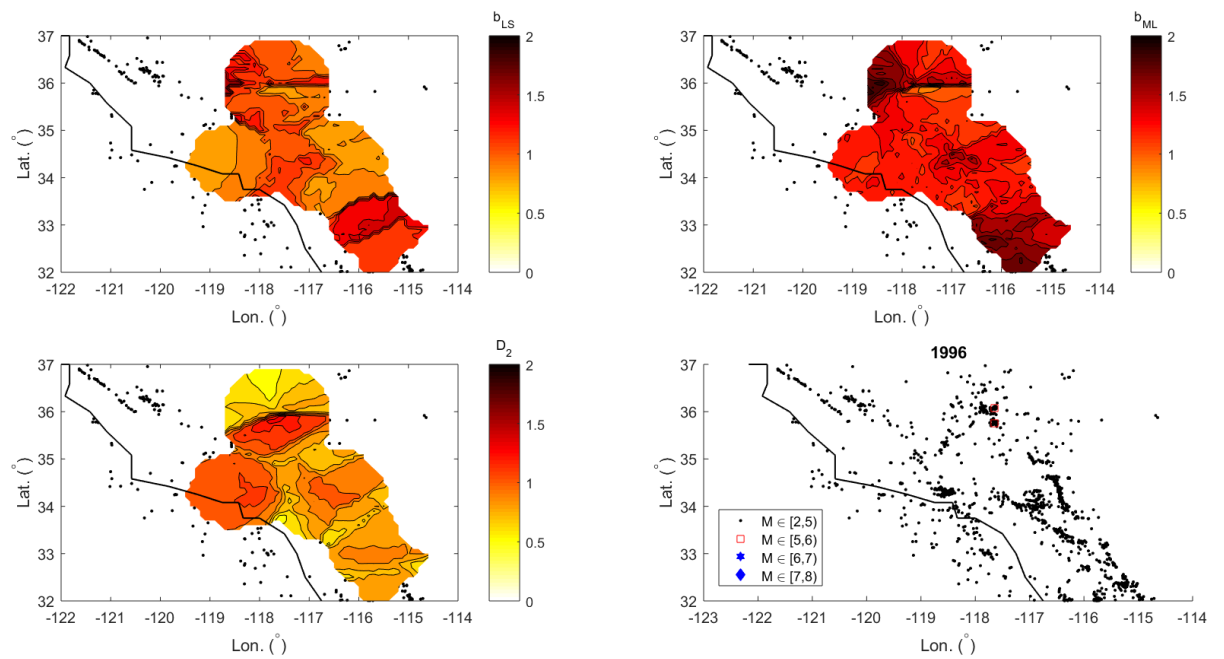
FIGURE A.15. Sets of spatial distribution maps for 1996.
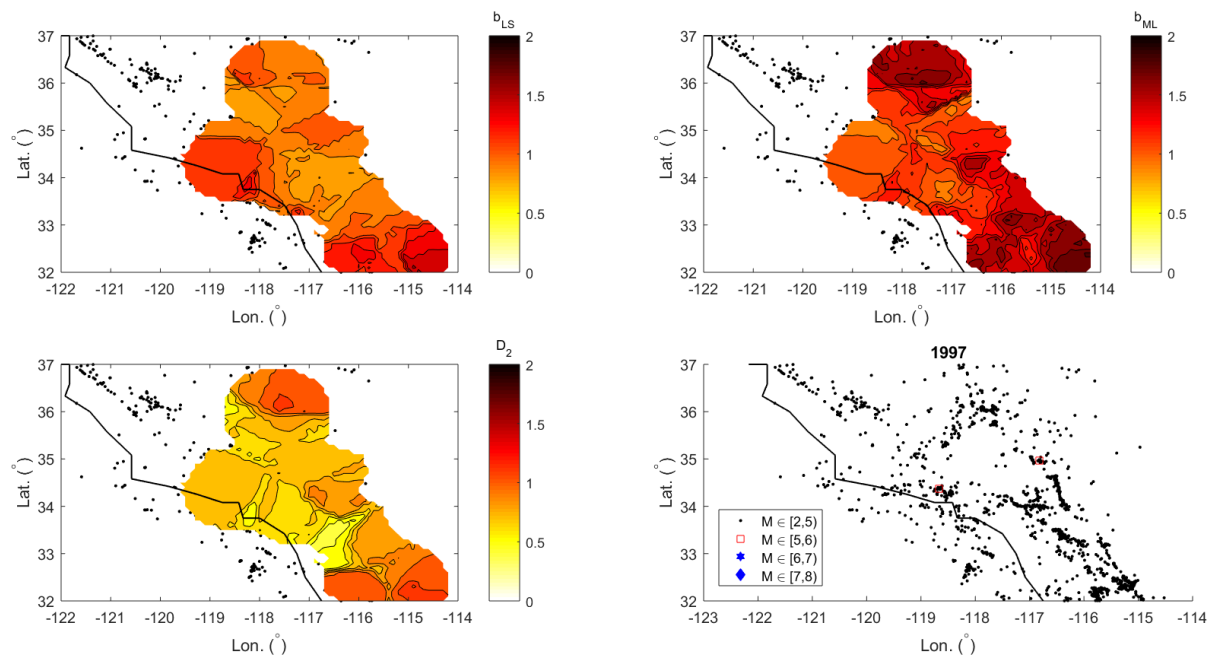
FIGURE A.16. Sets of spatial distribution maps for 1997.
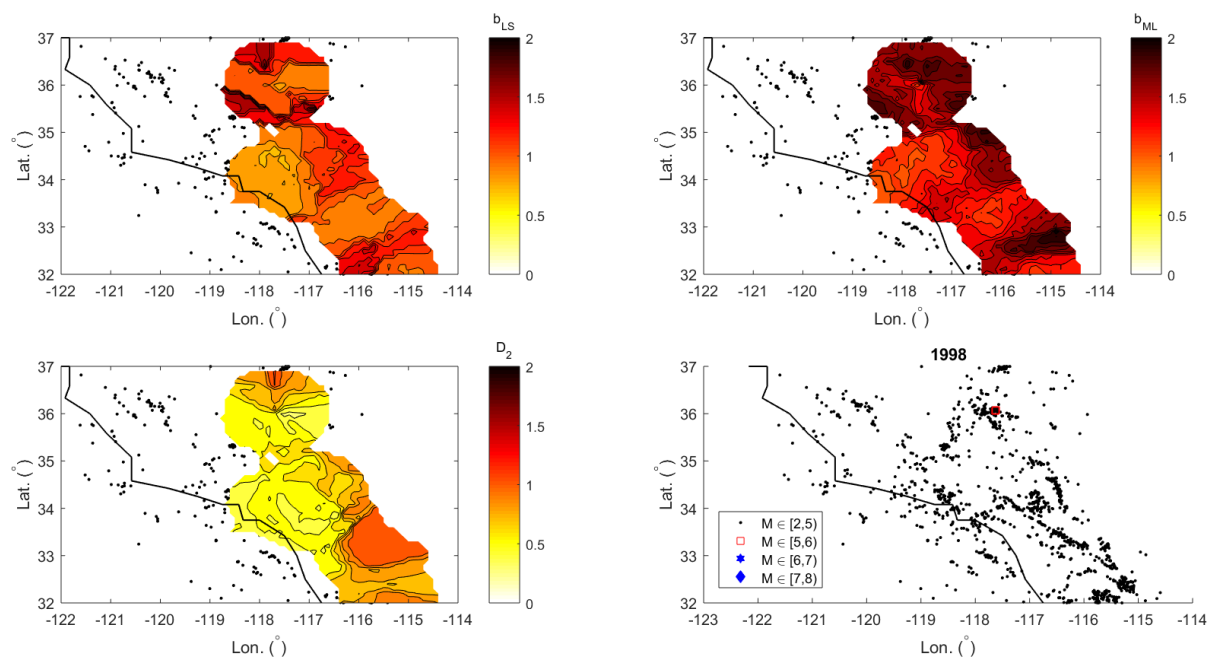
FIGURE A.17. Sets of spatial distribution maps for 1998.
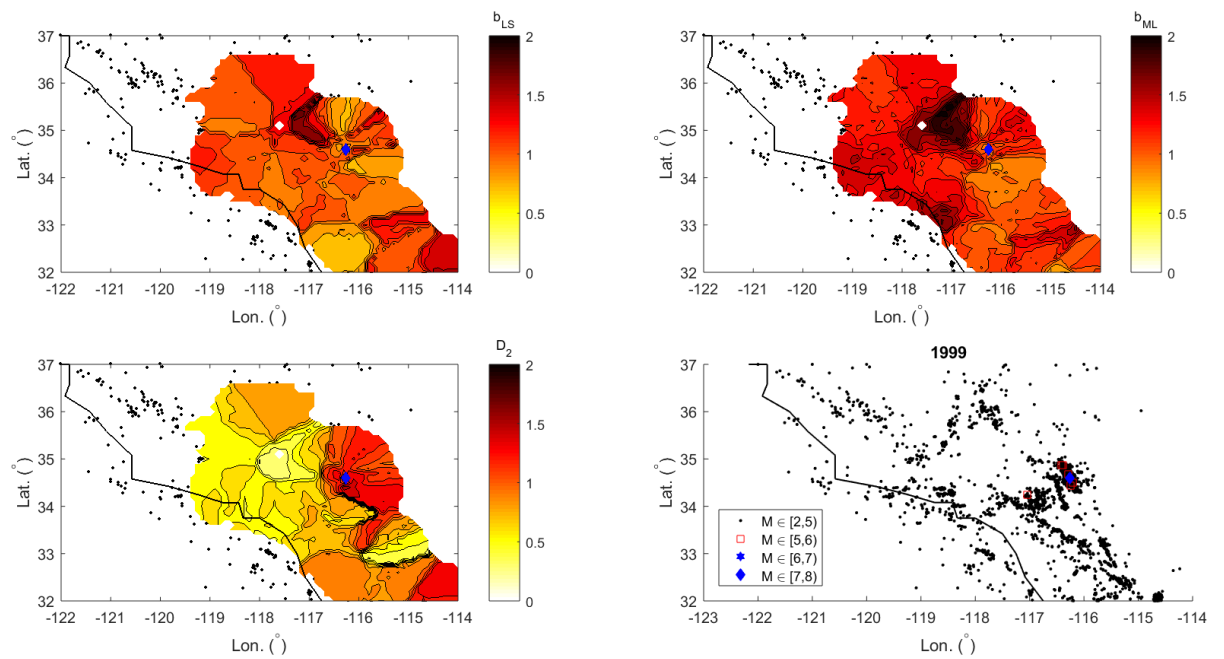
FIGURE A.18. Sets of spatial distribution maps for 1999.
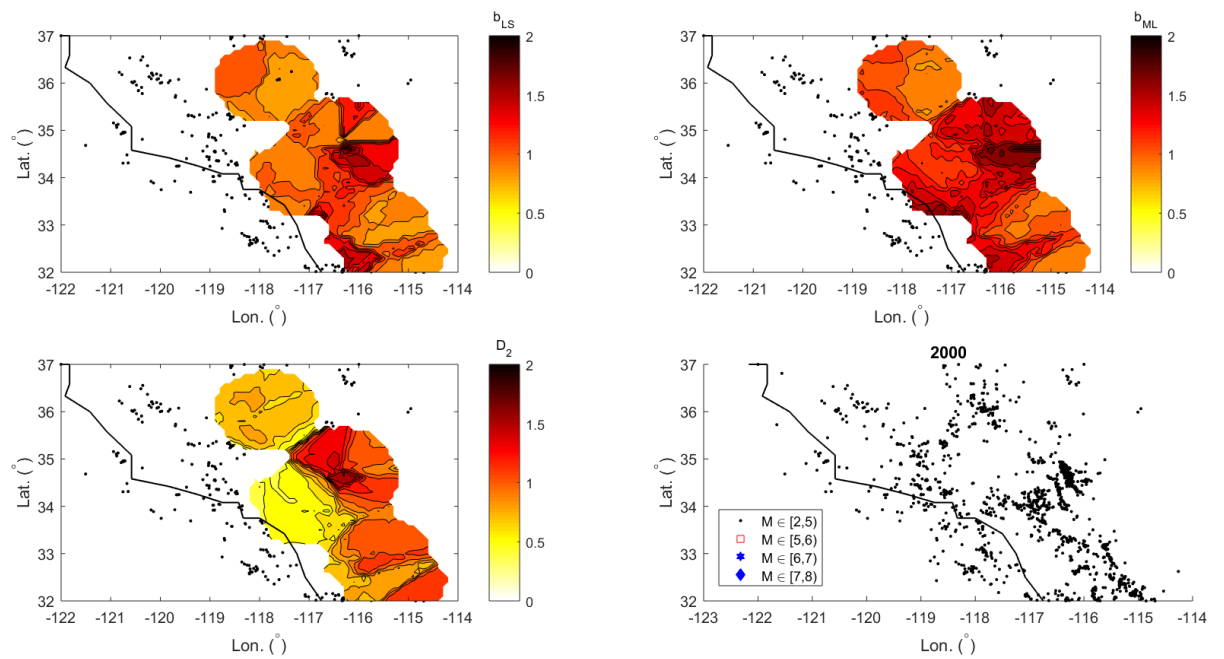
FIGURE A.19. Sets of spatial distribution maps for 2000.
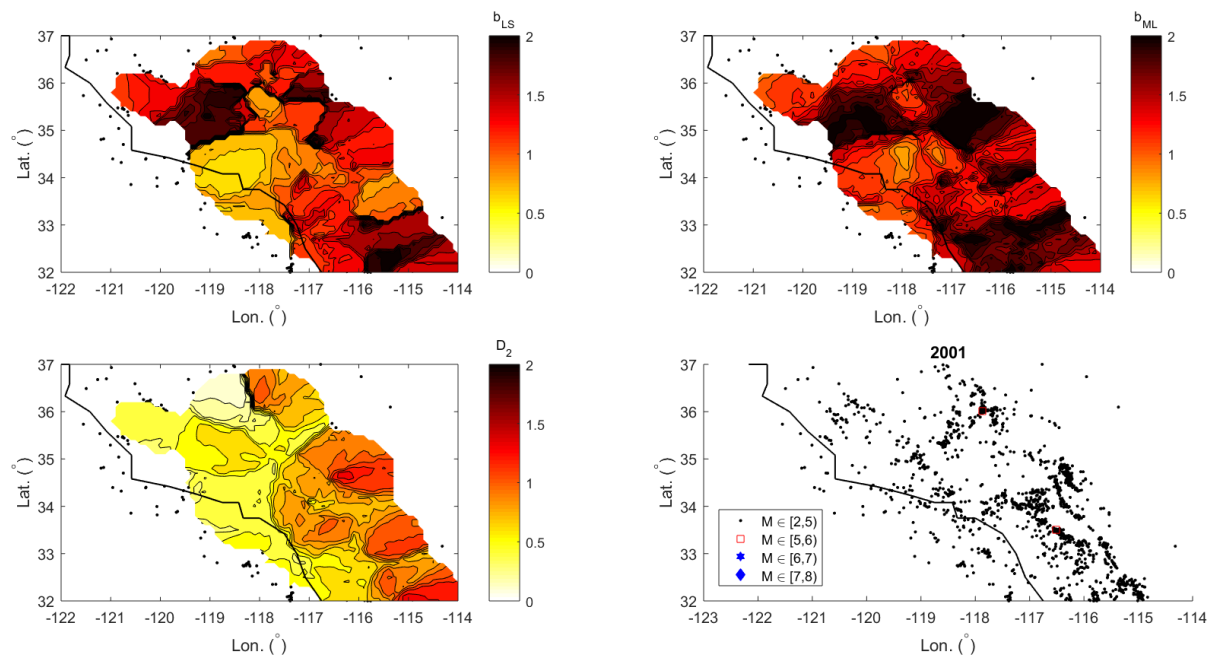
FIGURE A.20. Sets of spatial distribution maps for 2001.
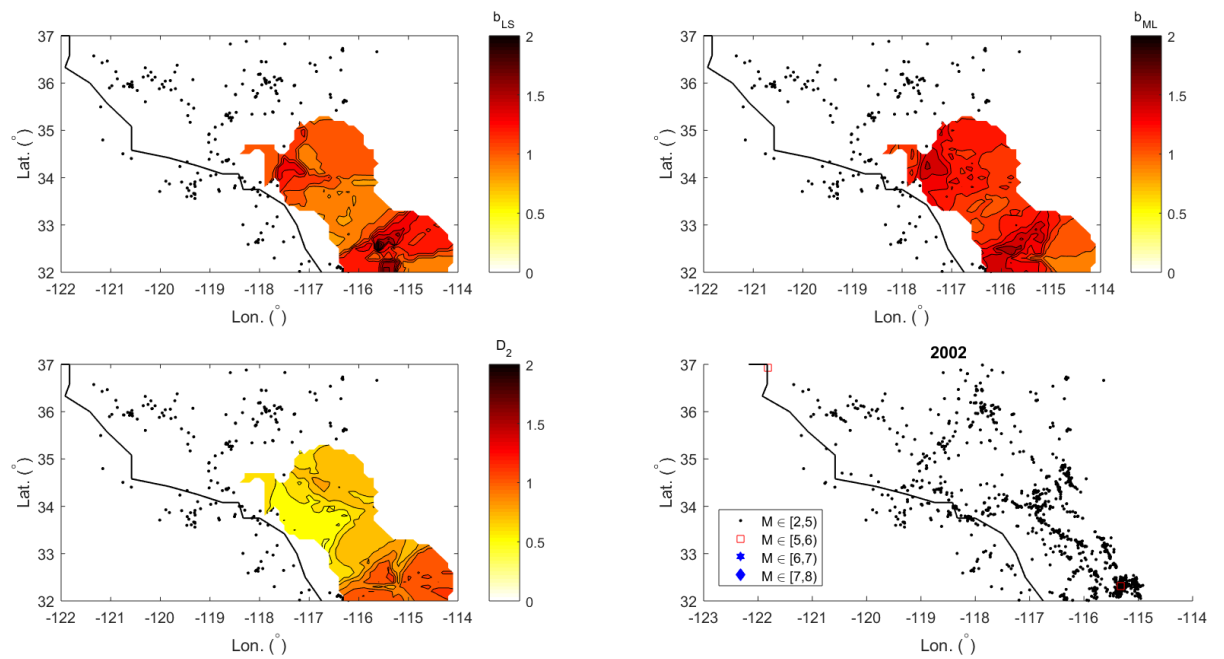
FIGURE A.21. Sets of spatial distribution maps for 2002.
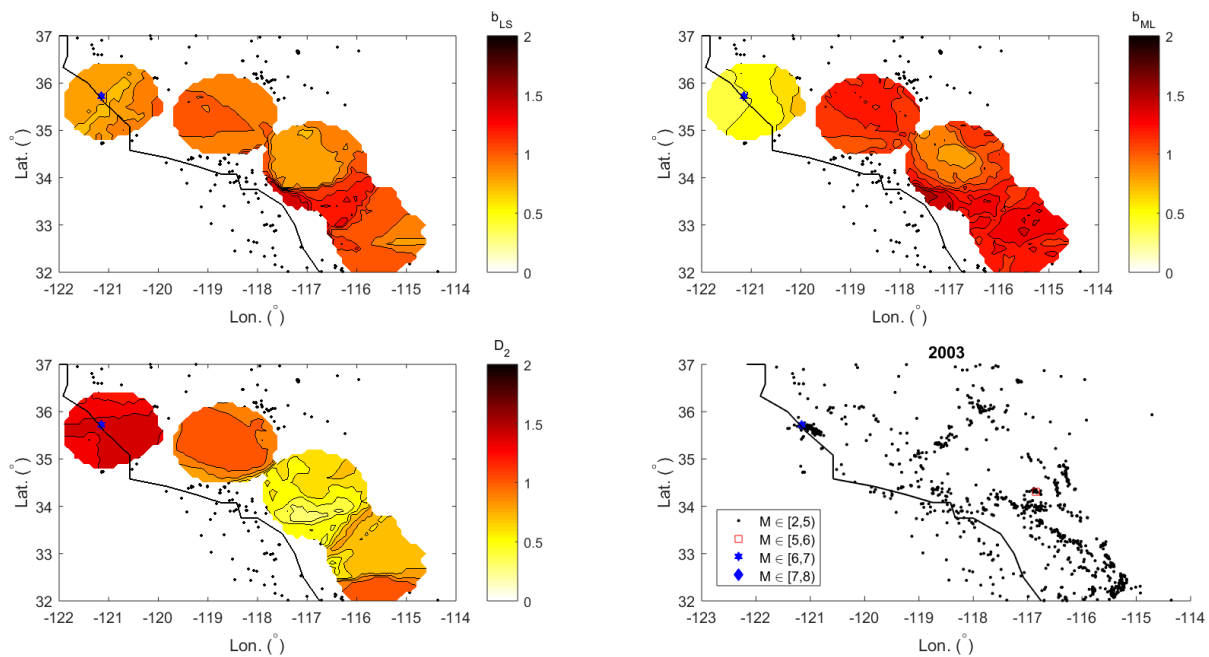
FIGURE A.22. Sets of spatial distribution maps for 2003.
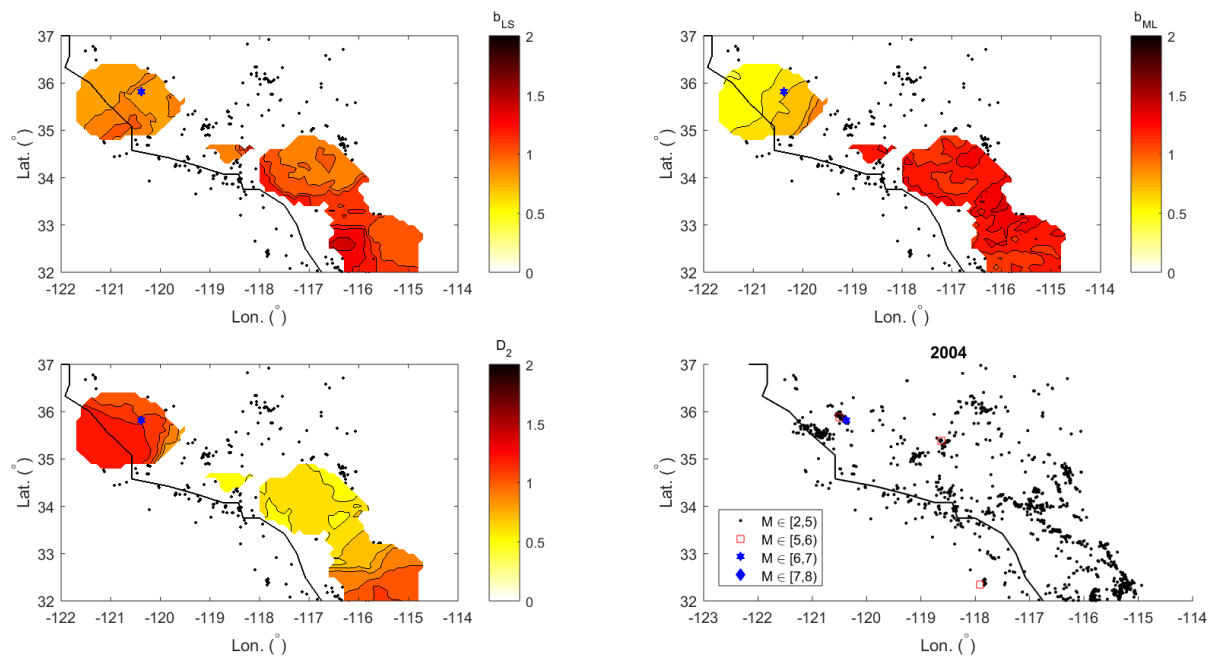
FIGURE A.23. Sets of spatial distribution maps for 2004.
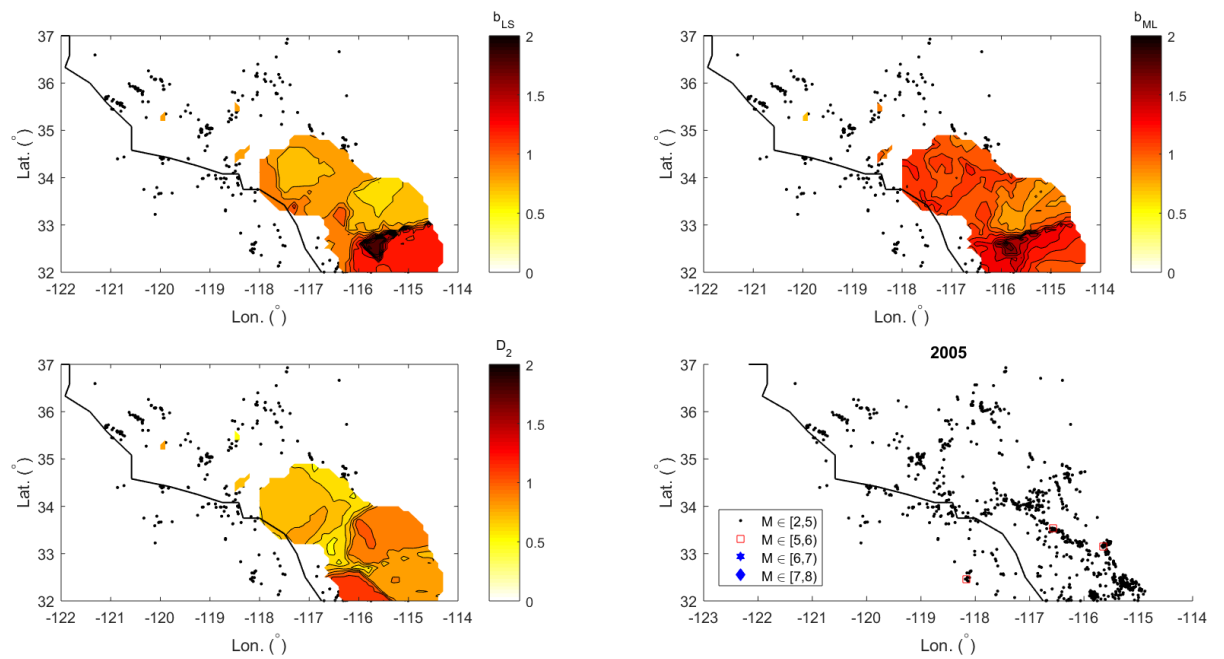
FIGURE A.24. Sets of spatial distribution maps for 2005.
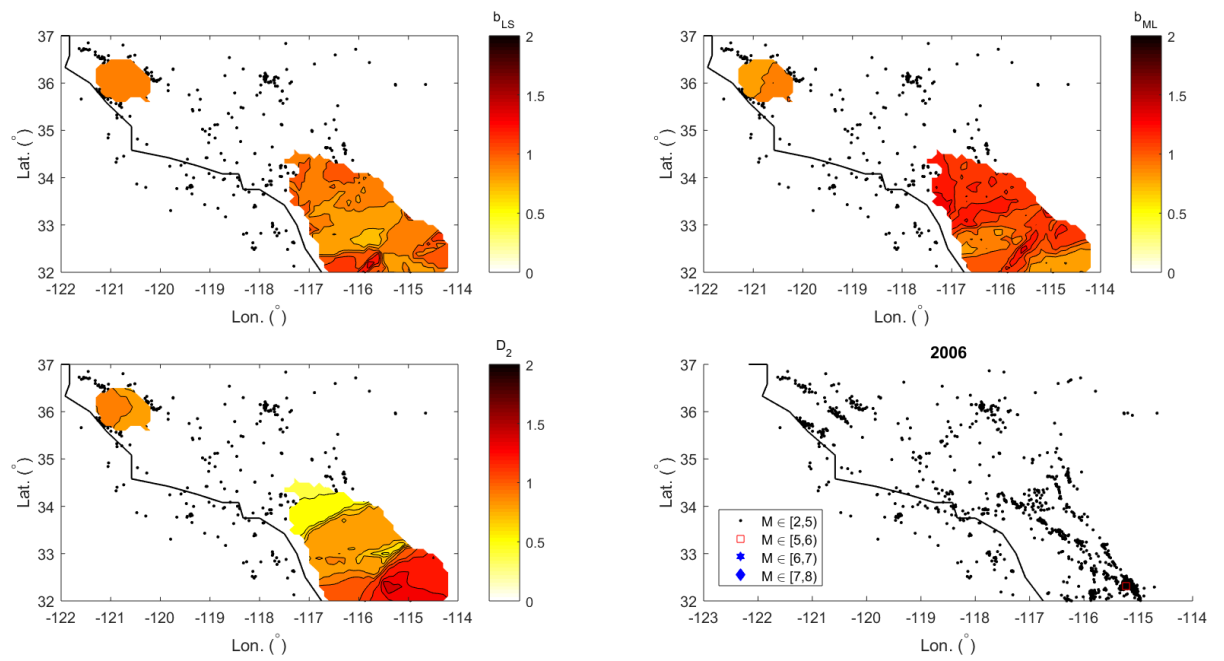
FIGURE A.25. Sets of spatial distribution maps for 2006.
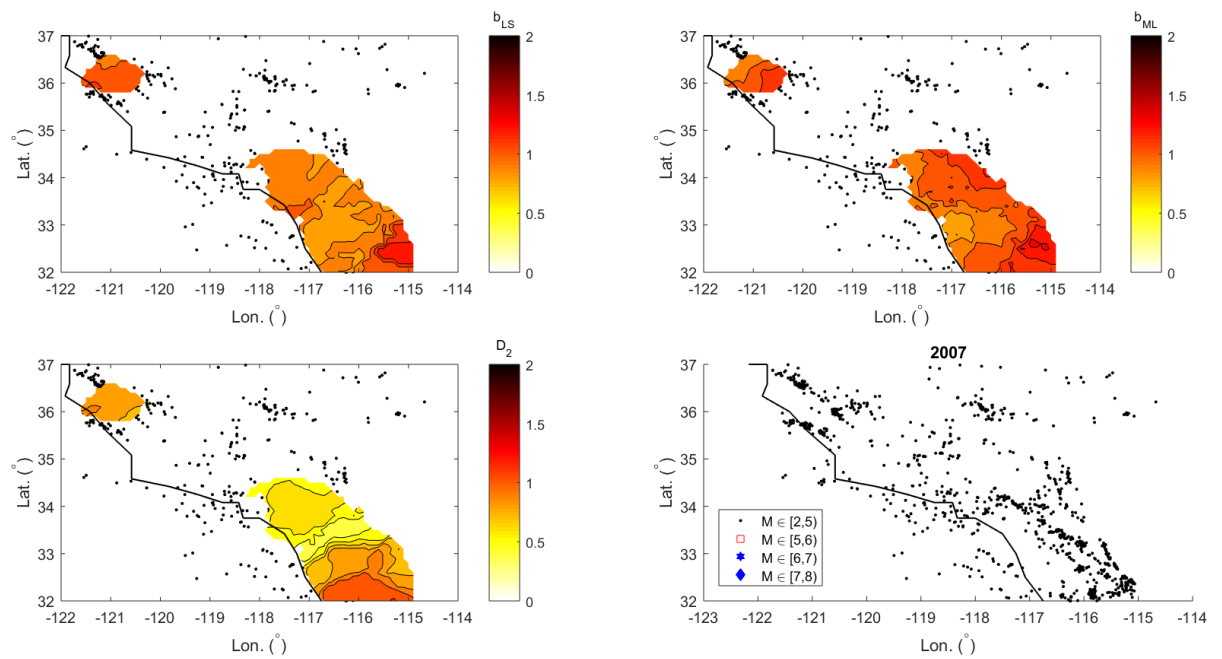
FIGURE A.26. Sets of spatial distribution maps for 2007.
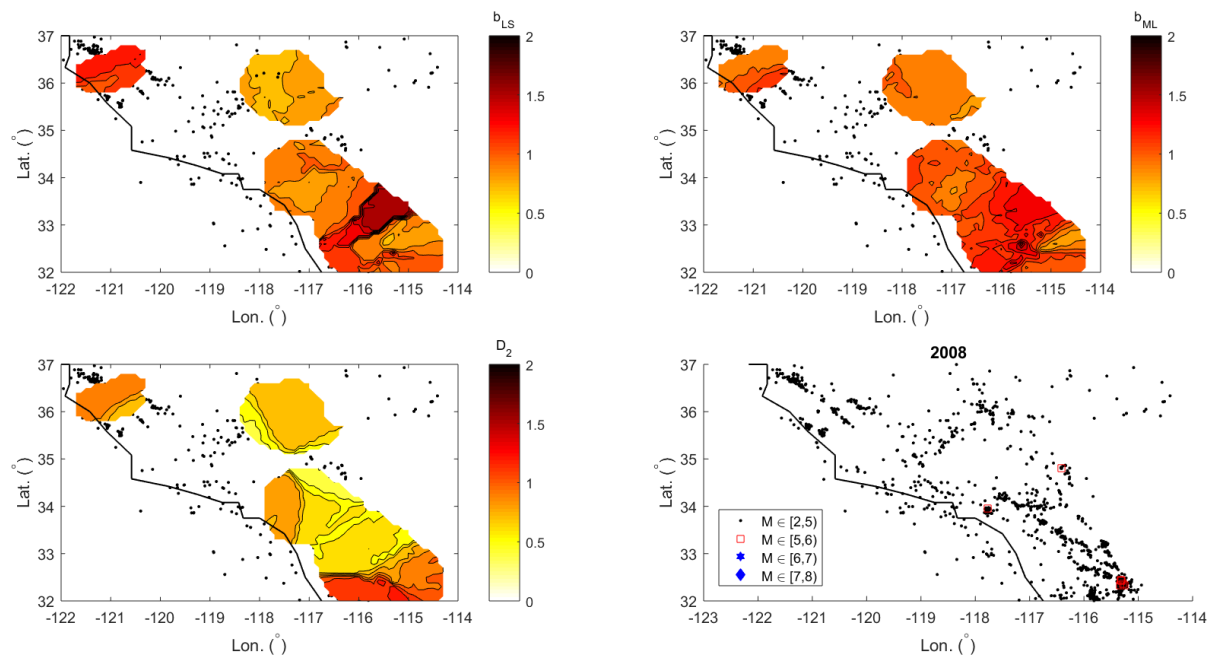
FIGURE A.27. Sets of spatial distribution maps for 2008.
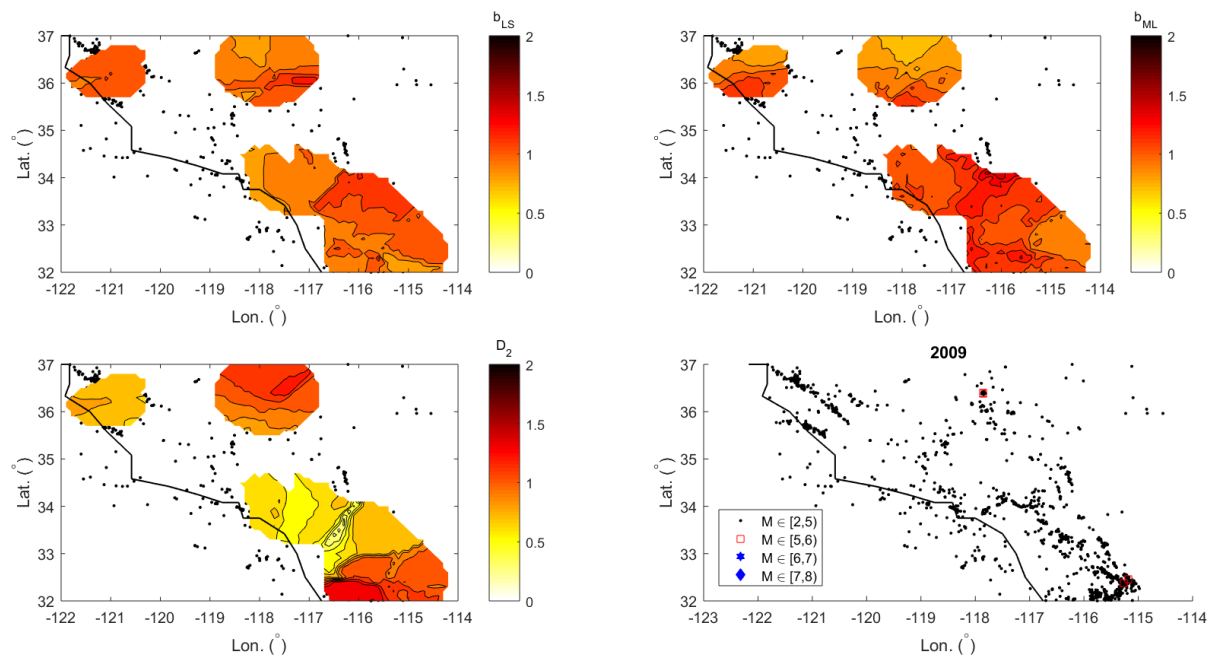
FIGURE A.28. Sets of spatial distribution maps for 2009.
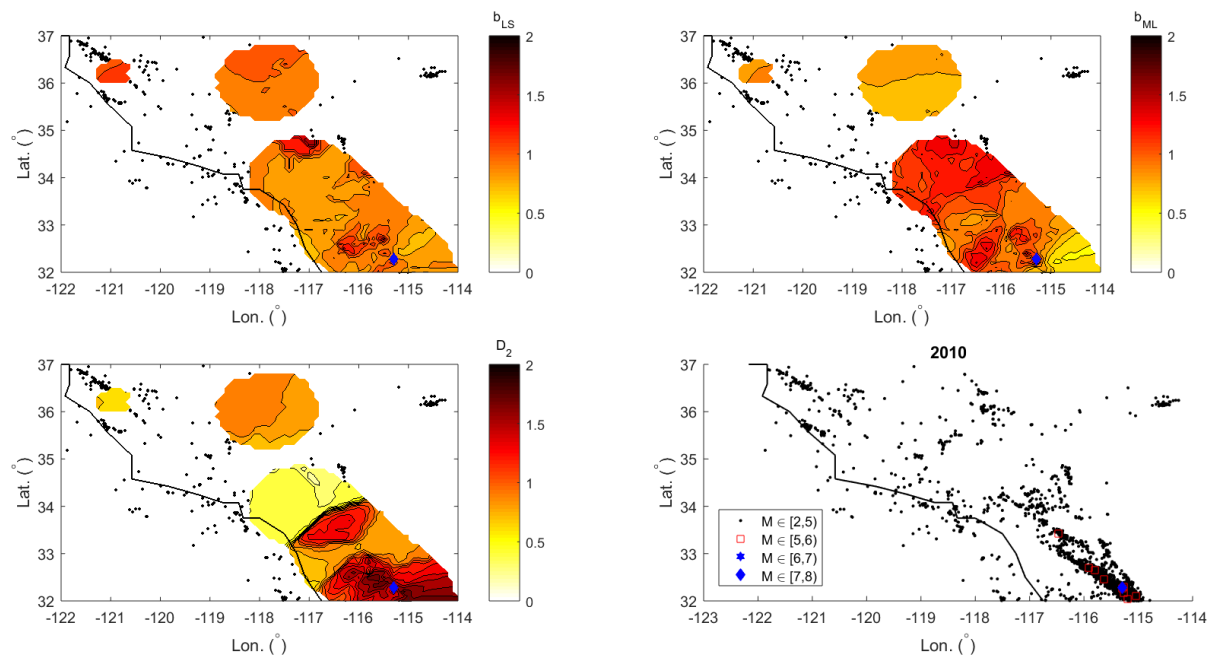
FIGURE A.29. Sets of spatial distribution maps for 2010.
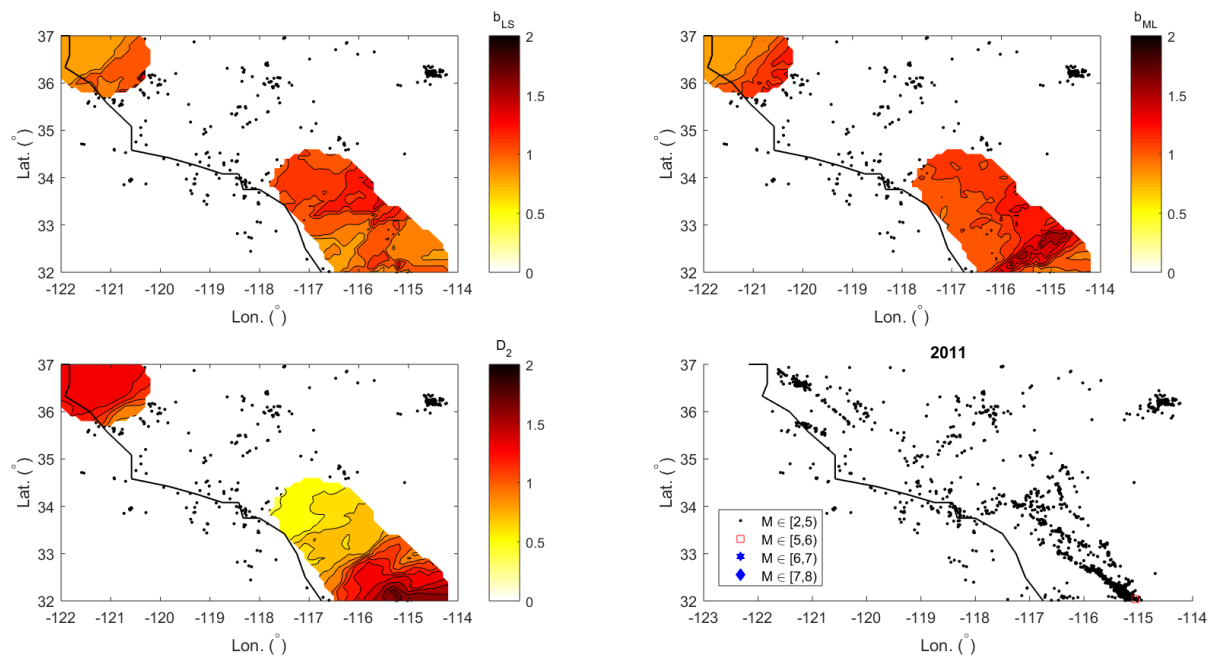
FIGURE A.30. Sets of spatial distribution maps for 2011.
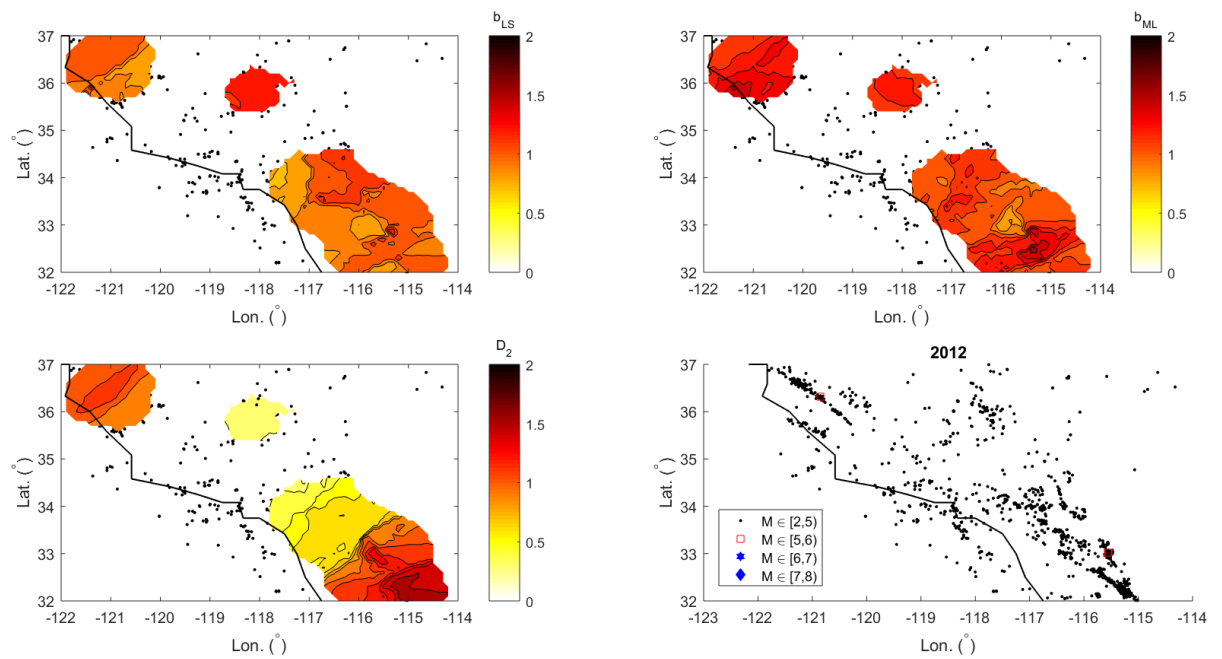
FIGURE A.31. Sets of spatial distribution maps for 2012.
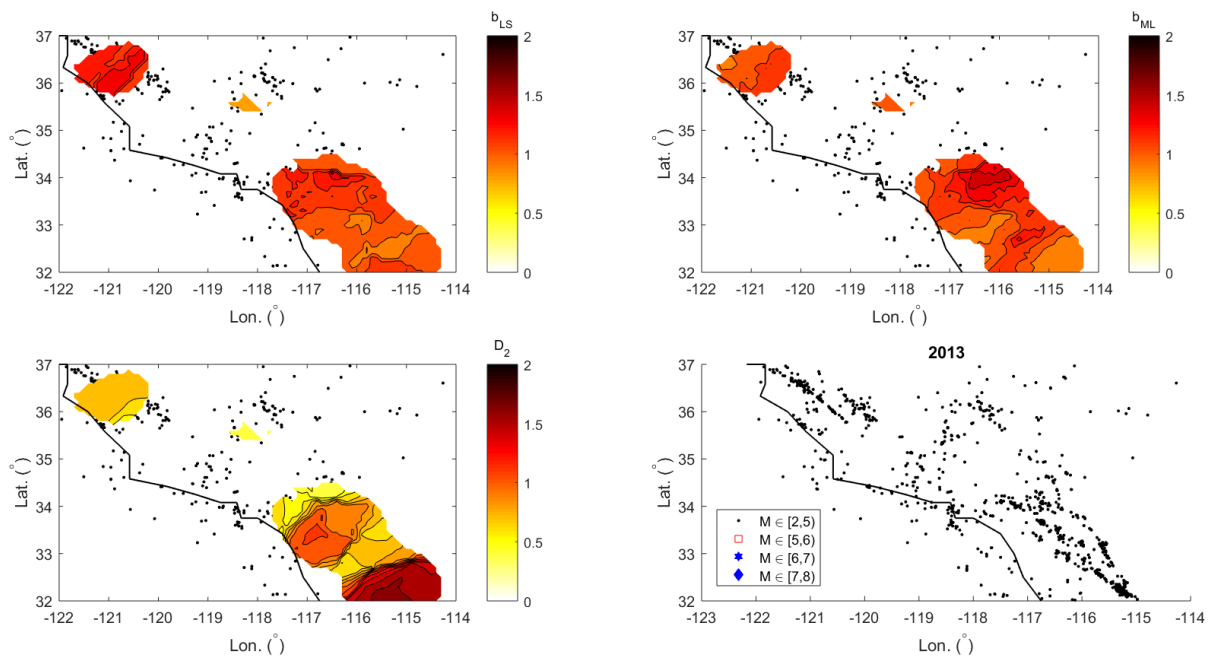
FIGURE A.32. Sets of spatial distribution maps for 2013.
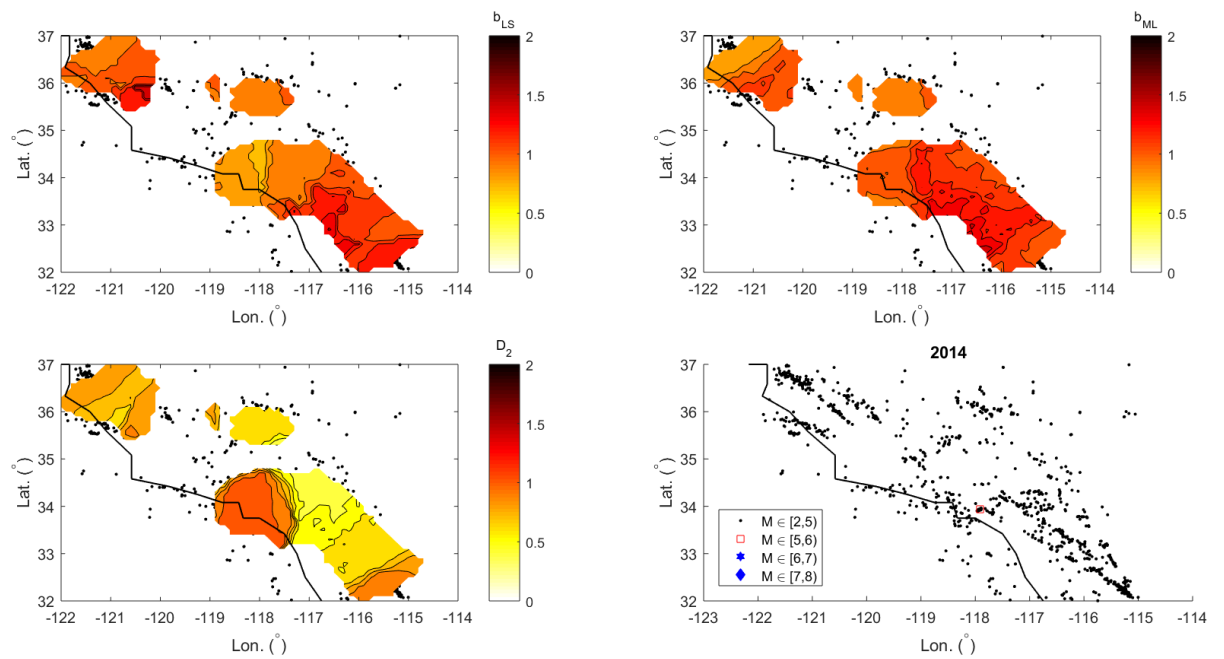
FIGURE A.33. Sets of spatial distribution maps for 2014.
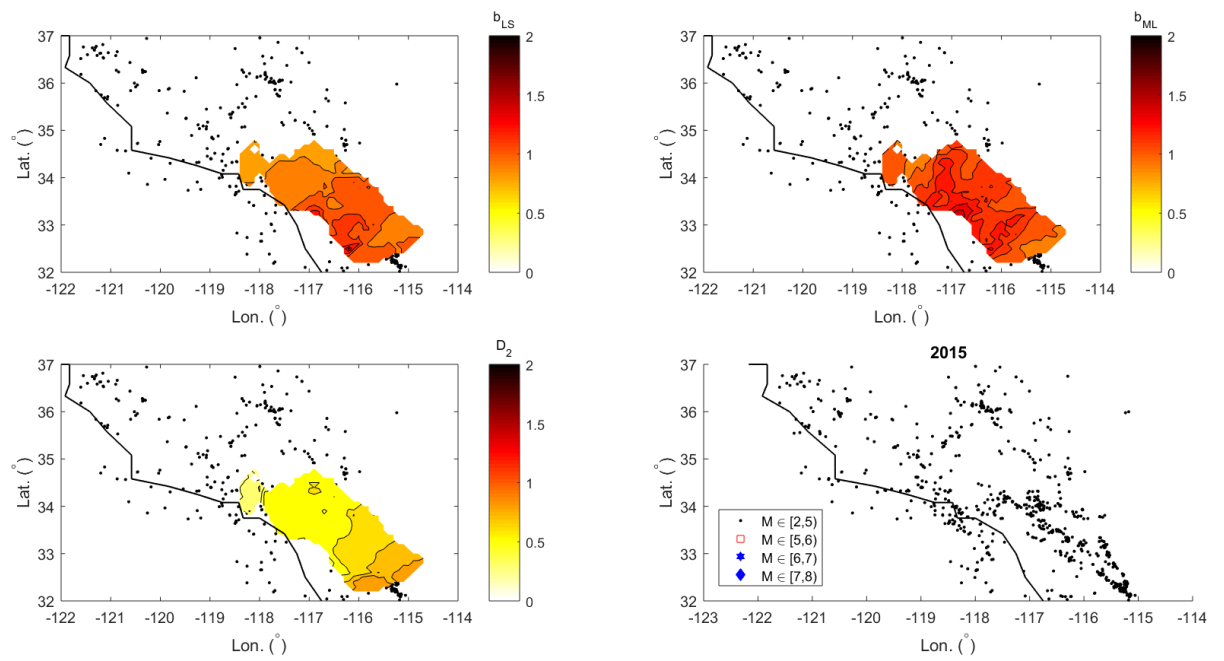
FIGURE A.34. Sets of spatial distribution maps for 2015.
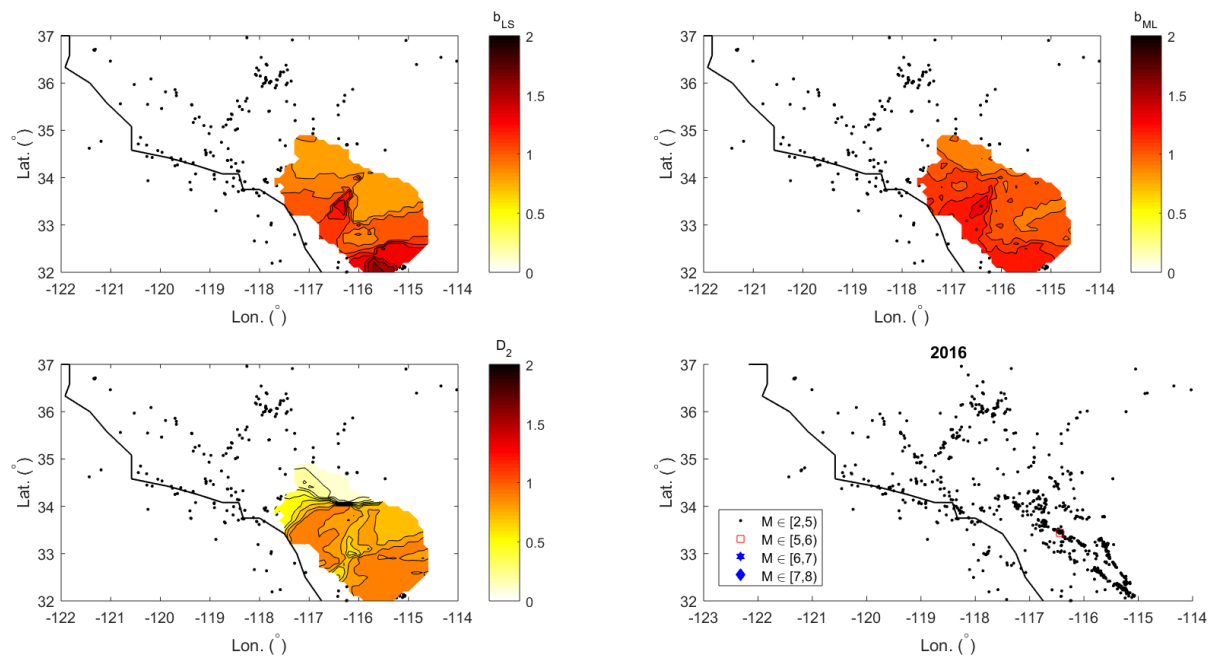
FIGURE A.35. Sets of spatial distribution maps for 2016.
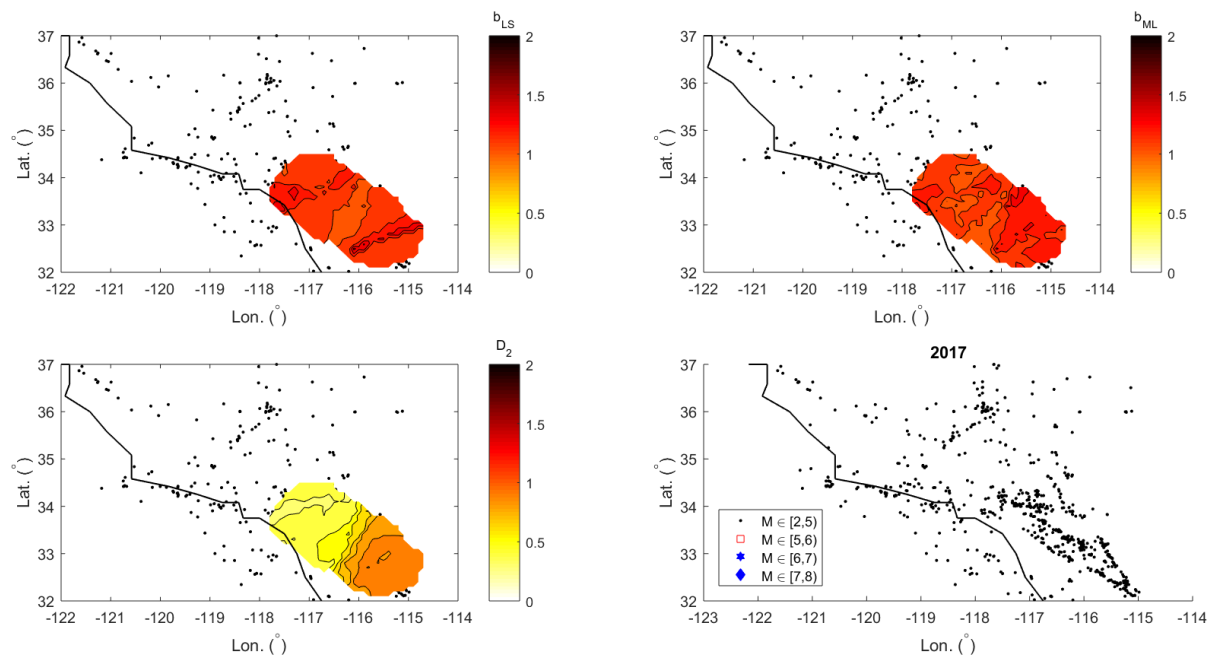
Figure A.36. Sets of spatial distribution maps for 2017.
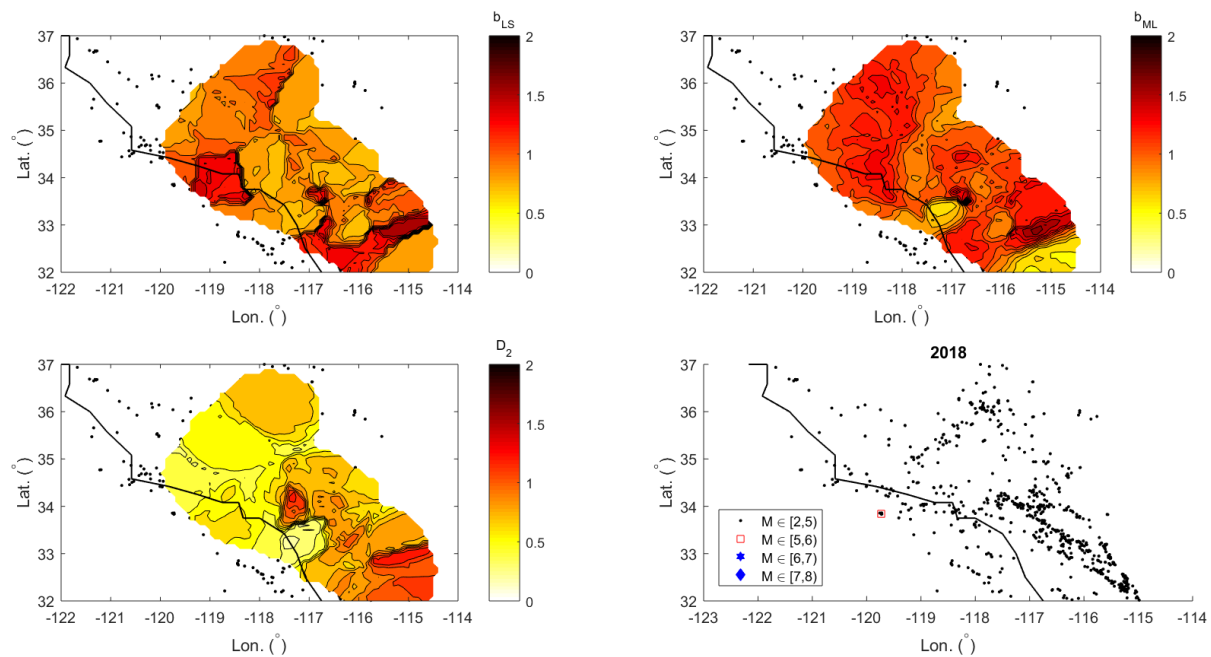
FIGURE A.37. Sets of spatial distribution maps for 2018.
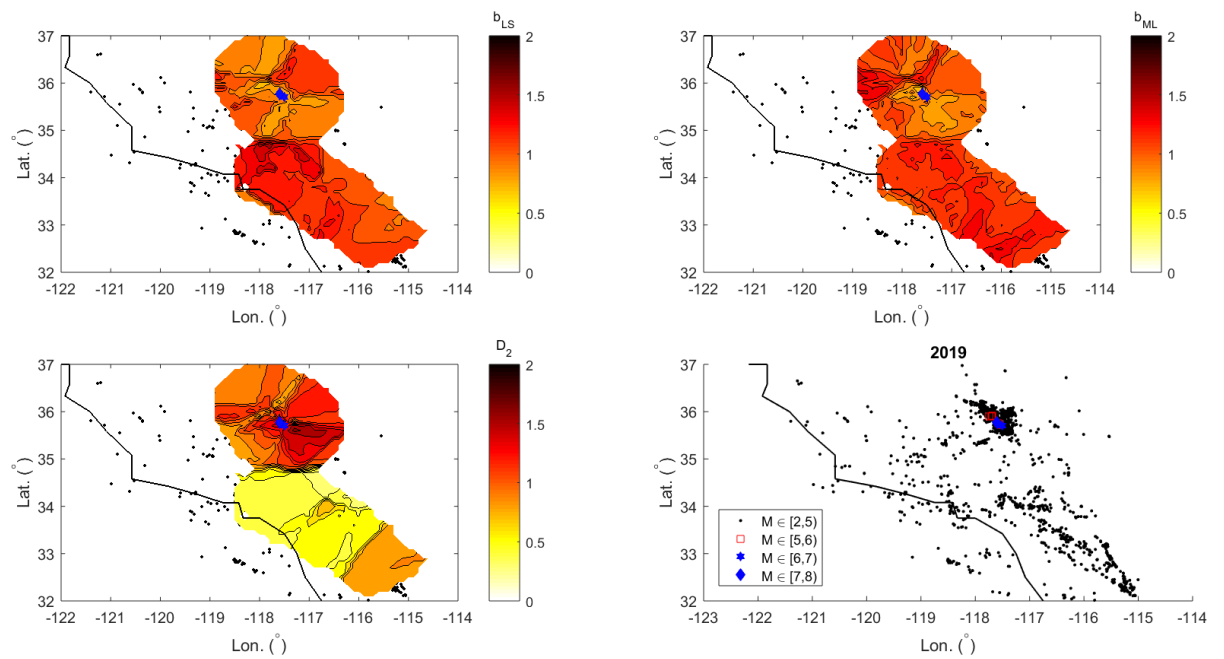
Figure A.38. Sets of spatial distribution maps for 2019.
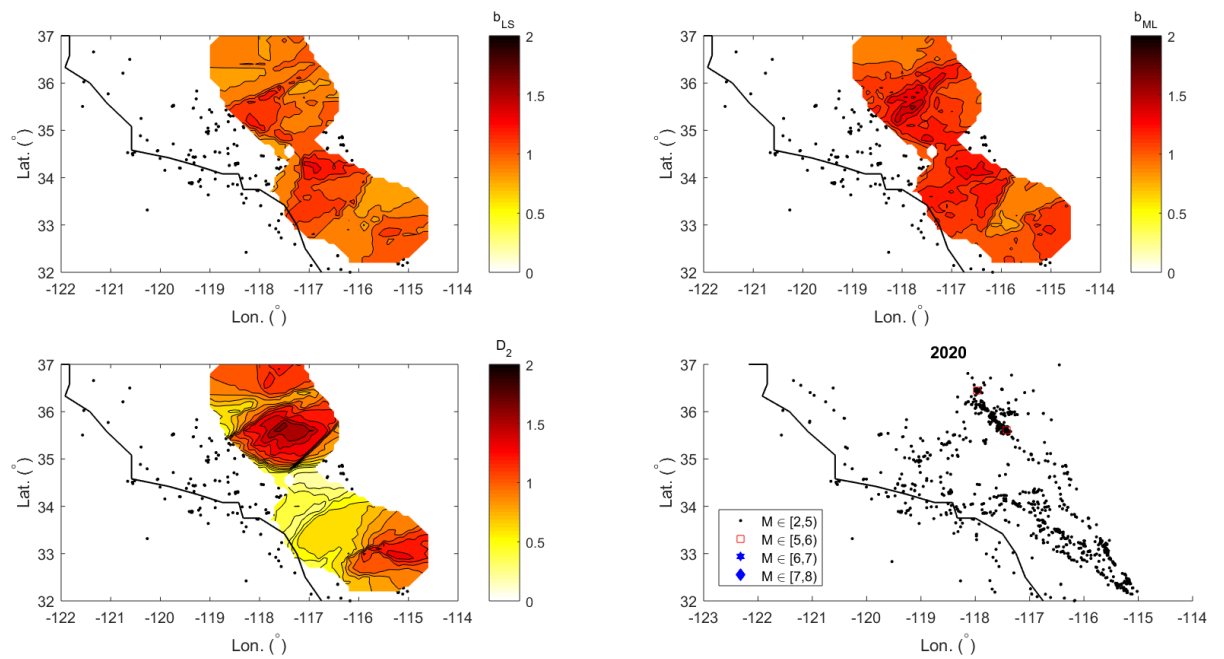
FIGURE A.39. Sets of spatial distribution maps for 2020.